首都大学東京　博士 (理学) 学位論文 (課程博士)

論文名

東京における夜間都市境界層の特徴と
その地上気温分布および風系との関係
(英文)

著者

中島 虹

審査担当者

主査

委員

委員

上記の論文を合格と判定する

平成　　年　　月　　日

首都大学東京大学院都市環境科学研究科教授会

研究科長

DISSERTATION FOR A DEGREE OF

DOCTOR OF SCIENCE
TOKYO METROPOLITAN UNIVERSITY

TITLE:

Characteristics of nocturnal urban boundary layer and its relation to distribution of surface air temperature and wind system in Tokyo metropolitan area

AUTHOR:

Ko NAKAJIMA

EXAMINED BY

Examiner in chief

Examiner

Examiner

QUALIFIED BY THE GRADUATE SCHOOL OF URBAN ENVIRONMENTAL SCIENCES TOKYO METROPOLITAN UNIVERSITY

Dean

Date

Characteristics of nocturnal urban boundary layer and its relation to distribution of surface air temperature and wind system in Tokyo metropolitan area

Ko NAKAJIMA

Department of Geography, Tokyo Metropolitan University

September 2018

Contents

List of Figures

List of Tables

Acknowledgments

I acknowledge Professor Hideo Takahashi of the Department of Geography, Tokyo Metropolitan University with great thanks and appreciation. Without his advice and encouragement, this study would not have been possible. I must also thank Professor Jun Matsumoto and Assistant Professor Hiroshi Takahashi for their insightful comments. I additionally thank Drs. Yoshihito Seto, Masato Nodzu, Fumiaki Fujibe, Jun-ichi Hamada, Tomoshige Inoue and Mr. Olaguera Lyndon Mark, and every member of the Laboratory of Climatology, Tokyo Metropolitan University. I am grateful to former Professor Hiroshi Yoshikado, the University of Saitama, for encouragement and suggestions. I particularly acknowledge the help of Dr. Nobumitsu Tsunematsu, Tokyo Metropolitan Research Institute for Environmental Protection, who provided the data of the Air Pollution Monitoring System in Tokyo used in this study. I further appreciate the members of the Department of Geography at Tokyo Metropolitan University, and my friends Drs. Fumikatsu Nishizawa, Masahiro Tanaka and Takako Utsugawa, for their interesting and unique advice. Finally, I am deeply grateful to my family for their long-term support.

This study used the observational data by the Japan Meteorological Agency, Air Pollution Monitoring System and POTEKA (Meisei Electric Co. Ltd.). Observations at the Sky Tower, West Tokyo, were conducted with the cooperation of Tanashi Tower Co., Ltd.

Abstract

An urban heat island (UHI) is a local-scale atmospheric phenomenon observed when the surface temperature is higher in an urban area than that in the surrounding non-urban areas. The heat island intensity (HII) defines the temperature difference between the urban and rural areas. The HII is maximized in nighttime, when a steep horizontal temperature gradient zone (*heat cliff*) is formed on the rural–urban boundary. On clear nights with weak wind, the surface temperature in rural areas is reduced by radiative cooling, and a ground-based inversion layer is formed. Meanwhile, the atmospheric stability near the surface of urban areas is nearly neutral. The nighttime UHI has been discussed in terms of surface heat emission and vertical mixing. However, although numerous studies have analyzed the horizontal air-temperature distribution in urban areas, the vertical potential temperature profile has been rarely observed. Moreover, in most previous studies of vertical potential temperature profiles over urban areas, the observations were collected several days. As sufficient analysis of long-term observational data is lacking, the diversity of atmospheric stabilities (vertical potential temperature gradients) and the characteristics of their annual and diurnal variations remain unclear. The formation mechanisms of the heat cliffs formed in the western and eastern parts of the Tokyo metropolitan area are also unclarified.

To bridge these gaps, this study investigates the temporal and annual variations of the vertical potential temperature profiles over the Tokyo metropolitan area, based on long-term observational data. It then relates the nocturnal urban boundary layer to the surface air-temperature distribution and the wind system.

This thesis is organized as follows.

Chapter I summarizes the UHI phenomenon and characterizes the nocturnal temperature distribution in the Tokyo metropolitan area.

Chapter II describes the Tokyo metropolitan area, data, and methods in detail. Prior to analysis, the temperature values acquired at the Tokyo Tower (TT) were validated. Although the vertical potential temperature profile in the surface layer should be neutral under strong-wind conditions, the potential temperatures at some specific heights were approximately 0.5℃ higher than those at heights exposed to the top 2% wind speeds. The potential temperature at each height was statistically corrected in this study.

Chapter III characterizes the vertical potential temperature profiles between 2001 and 2010. Using cluster analysis, it determines the vertical distribution of the potential temperature gradient under 250 m at each hour, from 18:00 JST (Japan Standard Time) to 08:00 JST of the succeeding day, under clear conditions with weak winds. The temperature distribution was separated into five categories (clusters A, B, C, D, and E). The atmospheric stability was neutral from the surface to the upper layer in cluster A, stable and neutral above and below 64 m, respectively in cluster B, weakly stable from the surface to the upper layer in cluster C, stable from the surface to the upper layer in cluster D, and strongly and weakly stable above (to the upper layer) and below 205 m, respectively, in cluster E. Clusters D and E were absent from May to August. During the nighttime of the summer season, the minimum depth of the ground-based mixed layer was 250 m, which is consistent with previous numerical simulations conducted in the Tokyo urban area. From November to February, the frequencies of clusters D and E increased before midnight and peaked around sunrise. The strongly stable layer in cluster E is thought to be the stable-layer base over the urban area. The nocturnal mixing-layer height reached $\sim$200 m or higher in winter, and its ratio (relative to the average building height around the TT) was larger than in other cities. The increase in stable-layer base height since the 1960s can be attributed to verticalization in central Tokyo. Enhancement or restraint of vertical mixing and vertical displacement of the stable-layer base are thought to contribute to temporal transitions in the vertical potential temperature profile at night.

Chapter IV analyzes the relationship between the HII and atmospheric stability in the urban and rural areas. The atmospheric stability over the non-urban area (ST) was significantly positively correlated with the HII, as reported in previous studies. The atmospheric stability over the urban area was similarly correlated with the HII. The HII was more strongly correlated with the potential temperature gradient difference between the rural and urban areas than with the potential temperature gradient in the rural area. The amount of excessive nocturnal heat in the Tokyo metropolitan area (TT) relative to the non-urban area (ST) was estimated from the observational data. After analyzing the heat budget of the air column carried from the non-urban to urban areas by the nocturnal land breeze, the heating by the downward sensible heat flux due to vertical mixing was estimated to exceed the upward sensible flux from the urban surface. This result accorded with previous observational studies conducted in small- or mid-scale cities, and may

manifest from mechanical processes. Previous studies have postulated neutral atmospheric stability over urban areas. However, the present study suggests that the stable layer over a non-urban area is preserved, even when it penetrates the Tokyo metropolitan area.

Chapter V characterizes the temperature distributions and wind systems under the clear nocturnal with weak wind nights in which both of the large (small) HII days were analyzed. Small HIIs were associated with dominant northerly winds during the nighttime, whereas large HIIs were associated with hourly wind-direction speed fluctuations in the western part of the Tokyo Wards area. The HII and atmospheric stability were described in terms of the parameters which were derived from the numerical simulations of the heat island circulation (HIC). These parameters admitted a regime in which the HIC develops over the edge of the urban area.

Chapter VI analyzes the relationships between the wind fluctuations and the horizontal temperature distribution were analyzed from 1-min data collected in a three-night case study. The period of the wavelike motion (20–50 mins) was 5–10 times longer than that of the Brunt-Väisälä oscillation (BVO). This ratio agrees with the previous observational results of Yokoyama *et al.* (1981). The wavelike motions were assumed as gravity waves (GWs) generated by the convergence of two wind flows: the northerly wind passing over urbanized areas such as Saitama, and the westerly cold current. The GW moved eastward from Fuchu to the Nerima Ward. The wind and temperature fluctuations were explained by vertical mixing between the upper neutral warmer layer and the surface-stable cooler layer. When the heat cliff was formed, wavelike motions developed in the western part of the Tokyo Wards area, but were absent in the central urban area. This boundary was consistent with the heat cliff. The GW was likely dispersed around the central urban area. The atmospheric stability probably changes between the Suginami and Shibuya Wards. At the TT, the fluctuations of potential temperature above 169 m increased when the westerly wind arrived. These fluctuations suggest a downward sensible heat flux from the elevated inversion layer to the surface layer. The wavelike motion sometimes occurred in the urban area. In these cases, the arriving westerly wind raised the potential temperature gradient, and the heat cliff became unclear. It is suggested that the stable westerly wind penetrated into the urban area.

Finally Chapter VII summarizes our findings and suggests future research topics.

Chapter I Introduction

1 Background of UHI

An urban heat island (UHI) is a local-scale atmospheric phenomenon observed when the surface temperature is higher in an urban area than in the surrounding non-urban areas. UHIs largely impact on human health and plants. For example, plants flower earlier in urban than in rural areas. Cities lower the spatial heating costs but increase the spatial cooling requirements, increasing the heat stress on human residents in summer (Oke *et al.* 2017). Oke (1982) derived the horizontal cross-section of temperature in and around typical near-surface UHIs. A steep horizontal temperature gradient zone, called a *heat cliff*, is formed on the rural–urban boundary (e.g., Oke 1982; Oke 1987; Kuttler *et al.* 2015). Within the urban area, the horizontal temperature gradients are small and are called a *plateau*. The temperature is maximized in the city core. The heat island intensity (HII) is defined as the temperature difference between an urban and a rural area. The HII follows a diurnal cycle (Oke and Maxwell 1975; Oke 1982) with a daytime minimum. As the daily maximum of the cooling rate is larger in a rural area than in an urban area, the HII rapidly increases several hours prior to sunset, reaches its maximum in the nighttime, and decreases after sunrise.

Schematic of the typical layering of the atmosphere over a city at night is shown in Fig. 1. To understand atmospheric stability, some researchers adopt the potential temperature rather than the air temperature (Oke *et al.* 2017). Potential temperature gradients can be neutral ($\Delta\theta/\Delta z=0$), unstable ($\Delta\theta/\Delta z<0$), or stable ($\Delta\theta/\Delta z>0$). In rural areas, radiative cooling reduces the surface temperature on clear nights with weak winds, forming a ground-based inversion layer. Therefore, this layer is stable (called a *nocturnal stable layer* in Fig. 1). On the other hand, ground-based inversion layers are rarely formed over urban areas at night, and the near-surface atmospheric stability, which is affected by heating from the surface and vertical mixing, is nearly neutral. This layer is called a *nocturnal urban boundary layer* (Godowitch *et al.* 1985; Oke 1982; Oke *et al.* 2017).

The near-surface thermal structure of the nighttime UHI has been discussed in terms of the vertical sensible heat flux and the vertical potential temperature profile (see Fig. 2): 1) the upward sensible heat

flux from the urban surface from which the nocturnal potential temperature decreases is suppressed due to the existence of anthropogenic heat, weak radiative cooling (a small sky view factor), and the release of stored heat in surface constructs (Oke 1982), and 2) the occurrence of downward sensible heat flux is caused by vertical mixing of the surface inversion layer due to the large urban roughness (Tamiya and Ohyama 1981). Although both processes should increase the potential temperature in the near-surface layer, the downward sensible heat flux reduces the potential temperature in the upper layer through mechanical mixing, which conserves the heat in the mixed layer. Both processes thus affect the vertical potential temperature profiles. According to observational studies in small- and mid-scale cities, mechanical vertical mixing might contribute more conspicuously to nighttime UHI formation than heating from the urban surface (e.g., Sakakibara 2001).

Previous studies also showed that a layer with a large vertical potential temperature gradient, called an *elevated inversion layer*, is formed above the nocturnal urban boundary layer (Bornstein 1968; Yokoyama *et al.* 1974; Uno *et al.* 1988; Kono *et al.* 2010). The sensible heat is transported downward from this layer to the surface layer (Uno *et al.* 1988), increasing and decreasing the potential temperatures in the lower and upper layers, respectively (Sparks and Toumi 2015). Therefore, an elevated inversion layer is regarded as an important phenomenon in UHIs (Nakagawa 2011; Sakakibara and Nakagawa 2011). Because the $\Delta\theta/\Delta$z is higher over rural areas than that of urban areas, the nighttime potential temperature difference between urban and non-urban areas decreases with height. The nighttime potential temperature difference between urban and non-urban areas decreases with height and vanishes at a height called the *coincident point*. Above the coincident point, the potential temperature is lower in urban areas than in non-urban areas. This phenomenon, known as *crossover* (Bornstein 1968), occurs at around the height of the elevated inversion layer. In general, the mixed layer over an urban area is shallower at night than during the day. During nighttime, the boundary layer is more susceptible to heating from the surface and mechanical mixing than in daytime (Bohnenstengel *et al.* 2011). Therefore, the vertical structure of the potential temperature is important for understanding the near-surface thermal environment.

Nocturnal tower-observation data in Beijing, China, recorded a ground-based inversion layer in the 1980s, which disappeared in the 1990s and 2000s (Yu *et al.* 2013). Yu *et al.* (2013) attributed this

change mainly to urbanization. Numerical simulations indicate that the mixed layer over an urban area at night rises from the ground to hundreds of meters (Saitoh *et al.* 1996; Kusaka and Kimura 2004; Japan Meteorological Agency (JMA) 2013). Using a two-dimensional mesoscale model, Martilli (2002) found that increasing the building height in urban areas raises the base height of the elevated inversion layers.

2 Nocturnal temperature distribution in the Tokyo metropolitan area

The Tokyo metropolitan area is among the most intensively urbanized areas in the world (Figs. 3 and 4). Numerous studies have analyzed the horizontal air-temperature distribution in this area (e.g., Yamashita 1996; Yamazoe and Ichinose 1994; Takahashi *et al.* 2014). For instance, Takahashi *et al.* (2014) derived the nocturnal temperature distribution with several heat cliffs formed in the metropolitan ward area. The heat cliffs appeared several hours before and after sunset, and were gradually enhanced near sunrise. These zones start from the southern part of Saitama Prefecture, they appeared through the border between the Nerima and Itabashi wards, Toshima, Shinjuku, and the area stretching from western Setagaya to the southwest. In European and American cities, heat cliffs are formed on the rural–urban boundaries (Oke 1987). However, the rural–urban boundary in the Tokyo metropolitan area (e.g., the Suginami Ward) is difficult to define. Yamashita (1990) suggested that the expansion of the Tokyo urban area, referred to as urban sprawl, affects the temperature distribution. Heat cliffs were reported at similar locations in the western part of the Tokyo metropolitan ward area in the 1990s and 2000s (Yamashita 1996; Takahashi *et al.* 2014). However, why heat cliffs are formed at the western part of the Tokyo Wards area remains unclear.

The Tokyo Tower (TT) is a communications tower in the Minato Ward district of the central Tokyo urban area. Meteorological data (e.g., temperature, wind speed and wind direction) have been recorded at several heights by the stationed air pollution monitoring systems (APMS) of Tokyo since the 1960s. In a case study in November of 1963, Ohta (1966) revealed an elevated inversion layer at approximately 150 m above ground level (AGL) in the morning. By the way, when vertical temperature profiles are observed from towers and buildings, the measurements are affected by solar shortwave heating and radiative cooling

of the tower-body surface. Especially, the effect of shortwave heating cannot be ignored during daytime hours (Yamazaki *et al.* 1971). In contrast, during nighttime hours, the vertical temperature profiles (relative to the surface air temperature and depth of the ground-based inversion layer) are consistent among tower observations, tethered-balloon measurements (Yamazaki *et al.* 1971) and infrared spectro-radiometer data (Yokoyama 1980). Therefore, from the observational data at TT, we can characterize the nocturnal vertical temperature profile over the urban Tokyo area.

3 Purpose and composition

The above studies have elucidated the UHI phenomenon. However, three problems are listed as follows. Firstly, whereas the horizontal air-temperature distribution in urban areas has been extensively reported (e.g., Oke 1982; Yamashita 1996; Takahashi *et al.* 2014), the vertical potential temperature profile remains undefined. In most of the existing studies on vertical potential temperature profiles over urban areas, the observations were limited to several days. Sufficient analysis of long-term observational data is lacking. Therefore, the diversity of atmospheric stabilities (vertical potential temperature gradients), the vertical potential temperature profiles, and the characteristics of their annual and diurnal variations, remain largely unknown. Next, observational studies in small-cities have reported a positive correlation between the HII and the ground-based vertical potential temperature gradient at rural areas (Sakakibara 2001; Nakagawa 2011). These studies assume neutral atmospheric stability in urban areas. However, the relationships between atmospheric stability in urban areas and HII is still unclear. Finally, heat cliffs are formed in the western and eastern part of the Tokyo metropolitan ward area. However, its mechanism remains unclear.

This study aims to characterize the near-surface vertically structured UHIs in terms of their nocturnal potential temperatures, and their relationships to atmospheric fields within the urban area. The frequencies and variations of these features are revealed in the long-term continuous observational data. The remainder of this study is structured as follows. Chapter II describes the study area, the Tokyo metropolitan area, the data, and the analysis methods. The temperature values at the TT were validated prior to analysis.

Chapter III analyzes the near-surface UHIs by deriving the vertical potential temperature profiles around the TT, and Chapter IV analyzes the relationship between the atmospheric stability and HII. In the latter analysis, the TT data are supplemented by observations at Sky Tower West Tokyo (ST), located in a non-urban area of western Tokyo. Chapter V categorizes and analyzes the temperature and wind fields under the clear nocturnal with weak wind nights. Chapter VI analyzed a case study of two nights with a wavelike structure of wind and one night with no wave behavior. Finally, conclusions are given in Chapter VII.

Chapter II Study area and methods

1 Study area and typical building height around the Tokyo Tower

The Kanto Plain is the largest plain in Japan (Fig. 3). The plain is bounded on the north and west by high mountains and on the south and east by the Pacific Ocean. The south and west of the Tokyo metropolitan area are adjacent to Tokyo Bay and the Kanto mountains, respectively. In nighttime, several local wind systems such as westerly mountain breeze and northerly land breeze develop over the area (Takahashi 1998).

The Tokyo wards (within thick red line in Fig. 4) has a population of approximately 9.3 million in an area of 626.7 km^2 according to the census in 2015. In this area, daytime population density in each ward area is larger than 10,000 km^{-2}, especially the values in the Minato, Chiyoda, and Chuo wards area are larger than 40,000 km^{-2}. These three areas locate around the TT.

Figure 5 shows historical changes in the number of buildings with at least 4 stories and at least 16 stories in the three wards . In 2005, the number of buildings with at least four stories was double that in 1975. Additionally, the number of buildings with at least 16 stories accelerated after 2000. Such increases in building height have probably affected the vertical temperature profile. To our knowledge, few studies have investigated the urbanization effect in this area.

Figure 6 shows the distribution of building heights around the TT, and the locations of the TT and the Tokyo District Meteorological Observatory (Otemachi). The building heights were defined based on the altitude of the Digital Surface Model (DSM, measured in December 2000) by Pasco Co., Ltd. and published by the Geospatial Information Authority of Japan (GSI). The former altitude data includes building heights. The GSI data, with a horizontal interval of 5.0 m, were interpolated to 2.5 m intervals to coincide with the DSM data. Where the altitude difference between DSM and GSI exceeded 4.5 m, the grid region was defined as a building region. The maximum building height in the 50-m^2 area (comprising 20×20 grid squares) was defined as the typical building height in the grid. Where the calculated building height exceeded the building height in 2000 (Osawa 2008), the grid region was removed. Most of the multi-story buildings ($>$ 100 m high) are located in the Shinjuku, Shibuya, and Chiyoda Wards. To obtain

the typical building height in the area, Fig. 7 shows total area covered by the buildings in each height range within 5 km of the TT (circled area in Fig. 6). The results, including the collective area of buildings over 200 m high, are summarized in Fig. 7. Most of the buildings in this area are between 10 and 50 m high, and the average building height is 29.6 m. This height was assumed as the typical building height around the TT in the 2000s.

2 Data

The potential temperature profile and the atmospheric weather conditions in the urban area were derived from the temperature data at selected heights of the TT (4 m, 64 m, 103 m, 169 m, 205 m, 221 m and 250 m AGL), and the wind speeds, WDs, cloud amounts and precipitation data at the Tokyo District Meteorological Observatory from 1991 to 2017. The observation height at 221 m was reduced to 205 m in 1996. Meanwhile, the air-temperature distribution and the wind system were determined from temperature data at 133 APMS stations, the wind speeds and directions at 293 APMS stations, and the temperatures, wind speeds, and directions at 76 stations of the Automated Meteorological Data Acquisition System (AMeDAS) developed by JMA. In this study, the 3-hourly values were used for the cloud analysis, and the hourly values were used for all other analyses. The distributions of the above-mentioned observatories are shown in Fig. 3.

To obtain the vertical temperature profile in the non-urban area, temperature data loggers (T&D Co. Ltd., TR-52) with natural ventilation radiation shields were installed at various altitudes (10 m, 20 m, 40 m, 60 m, 90 m, and 125 m AGL) on the ST (approximately 20 km northwest of the TT). Temperatures were measured at 10-minute intervals from November 17 of 2016 to February 28 of 2017. To smooth the temporal profile, two T&D loggers with a 5-minute time lag were also installed at each height. Every three data points (spaced at 5-minute intervals) were averaged for the analysis. However, after mid-December of 2016, the 5-minute interval data at some heights became unavailable due to a thermometer malfunction. At these times, three data points spaced at 10-minute intervals were averaged for the analysis. The data at 60 m were also missing after this date. Wind speeds at the ST (45 m, 80 m, 115 m, and 151 m AGL) were

measured every 10 minute by Tanashi Tower Co., Ltd. The detail temporal variations of air-temperature and wind were derived from the temperature data at 4 POTEKA stations (Meisei Electric Co. Ltd.), 47 APMS stations in Tokyo and 4 AMeDAS stations, and from the wind speed and direction data at 85 APMS stations and 5 AMeDAS stations. The data analysis employed the APMS and POTEKA values acquired every minute, and the AMeDAS values acquired every 10 minutes. The distributions of the above-mentioned observatories are shown in Fig. 4.

The ST and TT stand 63 m and 21.5 m above sea level, respectively. In this study, the potential temperature at the ST is defined as the temperature of an air parcel brought to the ground surface at the TT via the dry adiabatic lapse rate ($\Gamma d = 0.976$ ℃100 m^{-1}). The vertical potential temperature profiles at the TT and ST supposedly represent the atmospheric conditions at the urban center and in non-urban areas, respectively.

The temperature values at the TT were measured at the western side of the tower (Tokyo Metropolitan Government (TMG), 1966) using a platinum temperature-measuring resistor (TMG, 2008). The wind observation at the Tokyo District Meteorological Observatory was moved from Otemachi to Kitanomaru Park in November of 2007, where the observational height reduced from 75.4 m to 35.1 m. Hereafter, Period-1 defines the period between April 1 of 1991 and October 31 of 2007, and Period-2 proceeds from November 1 of 2007. Throughout the whole analysis period, the location is referred to as Otemachi. When selecting cases by wind speed at Otemachi, the threshold values were defined to ensure a consistent extraction ratio (Period-1, 2).

3 Validation temperature values at Tokyo Tower

In this study, the vertical potential temperature profile up to 250 m at TT was determined from the temperature values at five selected heights. For this purpose, the temperature differences at each height must be accurately observed. The vertical potential temperature profile in the surface layer is expected to be neutral under strong-wind conditions. To validate the temperature values, the vertical potential temperature profile under strong-wind conditions during two periods were checked:April 1991 to March

2015, and April 2016 to March 2017.

We first checked the values between April 1991 and March 2015. During this period, the temperature data at 103 m were excluded because they were missing from 2006 to 2013. The hours from 18:00 JST to the next 08:00 JST (when the ground surface, tower, and ventilation radiation shields were little affected by solar radiation) were classified as strong-wind hours. To prevent raindrop accumulation on the temperature-sensitive part under the strong winds, we selected the non-precipitation hours, during which the accumulated precipitation over the previous three hours was equal to 0.0 mm. Strong-wind hours were decided by setting threshold values of average wind speed over the previous three hours. Considering that the threshold wind speeds must break the surface stable layer and yield statistically significant numbers of strong-wind events, they were set to $7.0\,\mathrm{m}^{-1}$ in Period-1 and $6.5\,\mathrm{m}^{-1}$ in Period-2. The threshold values correspond to the top 2% of non-precipitation hours in each period. As a result, 1459 hours were selected as strong-wind hours during April 1991 and March 2015. Hours other than strong-wind hours were classified as weak wind hours.

To check the uniformity of the vertical potential temperature and the inter-annual change under strong-wind conditions, we calculated the potential temperature difference at 169 m during the strong-wind hours. The average temperature differences and number of strong-wind hours are plotted as time series in Fig. 8. In this figure, fiscal year were defined as the year, for example, 2010 indicates the period from April 1, 2010 to March 31, 2011. From 2001 to 2010, the potential temperature difference remained almost constant, but the slightly varying trends during the 1990–2000 and 2011–2013 periods are thought to be anomalies caused by instrument replacement and errors associated with gradual deterioration. Therefore, the period from 2001 to 2010 was selected as the target period.

Figure 9 is a wind-rose diagram at Otemachi. Plotted are the directions of the strong winds during the 2001–2010 period. Strong winds prevailed in the southwest and north–northwest directions. As the temperature instruments are located on the windward side, they should be little affected by the tower body. During the target period, the potential temperature was approximately 0.5°C higher at 64 m than at the other heights, even under strong-wind conditions. Meanwhile, the potential temperatures at 4 m, 205 m and 250 m were almost constant (0.1°C) throughout the target period (Fig. 8). Therefore, the average

potential temperature ($\overline{\theta}$) at these heights was assumed as the true value; that is, the vertical potential temperature profile was assumed to become uniform during strong-wind hours. Figure 10 presents scatter plots of the $\overline{\theta}$ versus measured potential temperatures at each height under strong (red) and weak (gray) wind conditions. The variances are clearly smaller during strong wind-speed hours than during low wind-speed hours. The regression coefficient is almost one at each height, and the RMSEs are approximately 0.1℃. The difference between the measured and $\overline{\theta}$ (the constant term of the regression formula) is less than 0.1℃ at all heights except 64 m (where the difference increases to ∼0.5 ℃). In addition, as the relationship remains unchanged in different temperature zones (that is, the deviation from the regression line is invariant with respect to temperature level), linearity is presumed to be maintained. Therefore, the potential temperature at each height was statistically corrected based on regression formula. Even when the wind was divided into south (S–SSW–SW) and northward (NW–NNW–N) directions, the corrected values, which varied between −5℃ and 35℃ in high winds of both directions, were consistent within 0.1℃ and were uninfluenced by the WD.

The values between April 2016 and March 2017 were also checked, but the temperature data at 103 m were included in this period. 38 hours were selected as strong-wind hours by the above-mentioned method. The air temperatures at the TT were corrected by the above-described method using the strong-wind hours between April 1 of 2016 and March 31 of 2017, but the way of obtaining $\overline{\theta}$ was altered as follows. Figure 11 shows the difference in potential temperature ($\Delta\theta$) during strong-wind hours from that at 169 m during this period. The average $\Delta\theta$ values at 4 m, 205 m, and 250 m were nearly 0.0 ℃. The potential temperature was 0.2℃ higher at 64 m and 103 m than at 169 m. Therefore, $\overline{\theta}$ during this period was defined as the average of the values at 4 m, 169 m, 205 m, and 250 m. Figure 12 presents scatter plots of $\overline{\theta}$ versus measured potential temperatures at each height during the strong-wind hours. Consequently, the potential temperature at each height was also statistically corrected based on regression formula.

4 Selection of clear nights with weak winds

Clear nights with weak winds over the observation period were selected by consulting the weather conditions at Otemachi based on Takahashi *et al.* (2014). First, a clear night was identified when the accumulated precipitation from 18:00 JST to the next 08:00 JST was equal to 0.0 mm, and the average cloud cover at 18:00 JST, 21:00 JST, the next 03:00 JST, and 06:00 JST was < 2.0. Second, a weak-wind night was identified when the average scalar wind speed from 18:00 JST to 08:00 JST was < 3.0 m s^{-1} during Period-1, or < 2.7 m s^{-1} during Period-2. The threshold wind speeds correspond to the lower 70% of clear days in each period.

By this process, 291 cases were selected as clear, weak-wind nights between 2001 and 2010 (see Table 1). Such cases were more frequent in the cold season than in the warm season. Six cases with missing temperature observations at TT were removed. Figure 13 is a wind-rose diagram of the weak winds on clear nights in Otemachi at 18:00 JST and the next 06:00 JST. On sunny days with low winds in central Tokyo, a southerly sea breeze develops in the daytime and a northerly land breeze develops in the nighttime (Fujibe and Asai 1979). Therefore, the selected cases are assumed as typical cases of clear, weak-wind days.

By the same method, an additional 18 clear nights with weak winds were selected from November 17 of 2016 to February 28 of 2017 (see Table 2).

5 Classification of vertical potential temperature

To characterize the vertical potential temperature and its temporal variations, the vertical profiles of potential temperature gradient were classified in each hour (totaling 4365 hours) from 18:00 JST to the next 08:00 JST on 291 clear days with weak winds (Table 1). The potential temperature gradient $\gamma_{t,i}$ given by

$$\gamma_{t,i} = \frac{\theta_{t,i+1} - \theta_{t,i}}{Z_{i+1} - Z_i} \times 100, \tag{1}$$

where Z_i is the observational height (m) ($Z_i < Z_{i+1}$) and $\theta_{t,i}$ is the potential temperature (°C) at Z_i at

time t. A cluster analysis of $\gamma_{t,i}$ is performed by Ward ' s method. The calculation is

$$D_{a,b} = \sum_{i=1}^{N} \sqrt{(\gamma_{a,i} - \gamma_{b,i})^2}. \tag{2}$$

The cluster number was defined from a dendrogram when the total variance was strongly reduced at this level of division.

6 Heat budget analysis

The amount of excessive heat (Q) below the coincident point (H) is given by Eq. (3):

$$Q = \rho C_p \int_0^H (\theta_{u,z} \ - \theta_{r,z}) dz, \tag{3}$$

where $\theta_{u,z}$ and $\theta_{r,z}$, z are the potential temperatures at z (m AGL) in the urban and rural areas, respectively, ρ is the mean air density (1.1 kg m^{-3}) between the surface level and H, and C_p is the specific heat capacity of air at constant pressure (1,004 J kg^{-1} K^{-1}).

In this study, we assumed that the air column moved from rural area to urban area. The heating rate of the air column (Q_H) is obtained by dividing the Q by the total travel time. The heat budget in an air column can be calculated by either of two methods: the Eulerian method (Sugawara *et al.* 2015) or the Lagrangian method (Yoshikado *et al.* 2014). In the Lagrangian approach, the Q_H on a clear night with weak winds is given by

$$Q_H = Q_s + Q_e + Q_{rad} + Q_{ant}, \tag{4}$$

where Q_s, Q_e, Q_{rad}, and Q_{ant} are the sensible heat flux from the surface, the downward sensible heat flux due to mechanical mixing, radiation heating, and the anthropogenic heat supply, respectively. Positive value in each term indicates that heat is added to the considered air volume.

7 Wavelet analysis

Wavelet analysis has been used previously to examine temporal variations, such as pressure and wind in nocturnal boundary layer (e.g., Viana *et al.* 2009). A time series can be simultaneously decomposed in a two-dimensional time–frequency domain by this method, providing unique advantages over other time-series analysis techniques, such as the fast Fourie transform. In this study, continuous wavelet analysis was employed on one-minute time-series of wind component and temperature measured by APMS, respectively.

The wavelet transform of the time-series f at the scale s and time t is defined as

$$F_{s,t} = \int_{-\infty}^{\infty} f(t')\Psi^*_{s,t}(t')dt', \tag{5}$$

where the asterisk means complex conjugation and $\Psi_{s,t}(t)$ is the wavelet function which is generated by scaling and shifting a mother wavelet $\Psi(t)$ along the time-series. The normalizing factor C_Ψ depends on the shape of the wavelet function:

$$C_\Psi = 2\pi \int_{-\infty}^{\infty} (\frac{|\hat{\Psi}(\xi)|^2}{|\xi|} d\xi, \tag{6}$$

with $\hat{\Psi}(\xi)$ being the Fourier transformed mother wavelet. In this study, the Morlet function was chosen as the mother wavelet (Viana *et al.* 2009).

Chapter III Characteristics of vertical potential temperature profile at Tokyo Tower

1 Characteristics of vertical potential temperature profile at Tokyo Tower

1.1 Classification of vertical potential temperature profile at Tokyo Tower

The dendrogram resulting from the cluster analysis is shown in Fig. 14. The cluster number was set to 5 (N = 5), because the total variance was strongly reduced at this level of division. Consequently, the vertical potential temperature distribution was separated into five categories: cluster A (1782 hours), cluster B (831 hours), cluster C (1184 hours), cluster D (372 hours) and cluster E (196 hours).

Hereafter, the atmospheric stability γ (℃ 100 m^{-1}) is defined as neutral (-0.5 $< \gamma \leq$ 0.5), weakly stable (0.5 $< \gamma \leq$ 1.0), stable (1.0 $< \gamma \leq$ 2.0), or strongly stable (2.0 $< \gamma$) (Aikawa and Hiraki, 2009). Panels (a) and (b) of Fig. 15 show the vertical profiles of the potential temperature gradient and the potential temperature offset from 250 m ($\Delta\theta$), respectively, in each cluster. In cluster A, the atmospheric stability was neutral from the surface to the upper layer. The other clusters were characterized as follows: a stable (neutral) layer was formed under (over) 64 m (Cluster B), a stable (weakly stable) layer was formed over (under) 205 m (Cluster C), a stable layer (1.0–γ–1.5) was formed from the surface to the upper layer (cluster D), and a strongly stable (weakly stable) layer was formed over (under) 205 m (cluster E). Note that the atmospheric stability below 250 m was neutral or weakly stable (0.0–γ–1.0) in clusters A, B, and C. In cluster E, the atmospheric stability was weakly stable and similar to that of cluster C under 169 m, but abruptly increased above this height. Between 205 and 250 m, the average and maximum γ were 3.4 ℃ 100 m^{-1} and 9.8 ℃ 100 m^{-1}, respectively.

In the vertical profiles of potential temperature gradient, the potential temperature difference between 250 m and 4 m was higher in cluster A than in cluster B, and higher in cluster B than in cluster C. In cluster E, $\Delta\theta$ was higher than in cluster D at 4 m, and lower than in cluster D at 169 m and 205 m.

1.2 Seasonal and temporal variations of vertical potential temperature

The monthly relative appearance frequencies of the five clusters are shown in Fig. 16. The appearance frequency of each cluster shows clear seasonal changes. For instance, clusters D and E (characterized by

a stable layer below 250 m and a strongly stable layer above 250 m, respectively), frequently appeared in November, indicating that they emerged mainly during the cold season. Conversely, cluster A frequently appeared in the May–August period (although warm-season cases were much rarer than cold-season cases; see Table 1). In July, the frequency of cluster A reached approximately 70%, and clusters D and E were absent during the March–August period. Cluster C, with a weakly stable layer formed under 250 m, was relatively rare in July and August, and common in December and January. The frequency of cluster B was consistent throughout the year.

Based on the above monthly changes, the cases were separated into summer (May–August: 35 days) and winter (November–February: 176 days). Figure 17 shows the nocturnal temporal variations in the relative appearance frequencies of the respective clusters. In summer (Fig. 17a), the frequency of cluster A exceeded 80% between sunset and midnight, whereas that of cluster C gradually increased after midnight. Even around sunrise, clusters A and B together comprised around 70% of the instances, and clusters D and E were absent during nighttime. In winter (Fig. 17b), cluster A comprised approximately 70% of the instances until 20:00 JST, but under 10% around sunrise. On the contrary, the frequencies of clusters D and E increased before midnight, and were maximized at 27% and 17%, respectively, around sunrise. The sunrise period was dominated by cluster D. The frequency of cluster B was approximately 20% through the nighttime. In summer, a stable layer was sometimes formed at the bottom of the TT (under 100 m), but the nighttime period was typified by a neutral or weakly stable layer formed below 250 m. In winter, a stable layer ($\gamma \sim 1$ ℃ 100 m^{-1}) or strongly stable layer ($\gamma \sim 3$ ℃ 100 m^{-1}) was sometimes formed below 250 m or above 250 m around the sunrise period. The γ under 169 m was similar in clusters C and E. Above 205 m, the γ increased in both clusters. Therefore, in some cases of cluster C, a strongly stable layer was formed above 250 m, as observed in cluster E. Cluster C was six times more frequent than cluster E (1184 h vs. 196 h). A strongly stable layer in the upper layer in cluster C suggests that the climatological height of the stable layer in the Tokyo urban area generally exceeds 250 m, the highest observation point at the TT. However, clusters C and E, in which a strongly stable layer was formed under 250 m, were not observed in summer. Therefore the stability change below 250 m was smaller in summer than in winter.

Focusing on clusters D and E, we then analyzed the temporal variation of the vertical potential temperature profile in winter (November–February).

1.3 Vertical potential temperature in winter

During winter, the frequencies of clusters D and E increased after midnight. When a cluster D or E occurred during 03:00 JST to 06:00 JST, and lasted for at least one hour, the case was selected for analysis. Ultimately, 74 cases of cluster D and 45 cases of cluster E were selected. Among these, 27 cases included both clusters. The cases including clusters D or E were classified into their respective groups, and cases common to both groups were assigned to both groups. The temporal cluster changes in each group were then determined. For example, A→B indicated a change of cluster A to cluster B. This analysis included all types with frequencies exceeding 10% for at least one hour. Five patterns of unchanging clusters and nine patterns of changing clusters were finally selected. Figure 18 presents the nocturnal frequency variations indicating the temporal changes in the clusters.

In group D (E) comprising cluster D (E), the frequency of D→D (E→E) cases increased after midnight (Fig.18a, d), eventually accounting for almost all cases. Therefore, the nights were divided into two categories in which cluster D or E persisted throughout the night.

In both D and E groups, D→E were moderately frequent, but C→D and C→E were frequent in clusters D and E, respectively (see Fig.18b, e). Meanwhile, D→C were frequent in group D, and E→D and E→C were frequent around sunrise in group E. The frequencies of A→B, B→C and A→C were similar in both groups from sunset to midnight. The A→A, B→B and C→C instances were also similar in groups D and E. Nights in which the cluster changed from A or B to E or D were very few. Therefore, it was assumed that clusters D and E appear via cluster C.

Thus, in winter, the cluster transits from A→ (B→) C during sunset to midnight. In the midnight to sunrise period, the nights are divided into group D (signified by a cluster change from C to D) and group E (signified by a cluster change from D to E). In Group D, a strongly stable layer is formed under 250 m, and Group E features a strongly stable layer above 200 m. Instances of D→E and E→D changes are also

evident (Fig.18b, c, e, f).

2 Temporal variation of vertical potential temperature in winter

At some heights, the potential temperature gradient changed during a cluster transition. This suggests that the amount by which the potential temperature changes depends on the height. Therefore, this section analyzes the potential temperature changes at each height in high-frequency cases of clusters C, D, and E after midnight. The results at each height during the 24:00–06:00 period JST are presented in Fig. 19. Plotted are the height versus rate of potential temperature change during (a): C→D changes (69 hours), (b): C→E (49 hours), (c): D→E (35 hours), (d): D→C (32 hours), (e): E→C (27 hours) and (f): E→D (28 hours). Between midnight and sunrise, the temperature declined in a time- and height-dependent manner. Therefore, the average hourly change in the potential temperature at each height and time was computed for all winter nights with clear skies and weak winds. The vertical distribution of the potential temperature change was obtained by subtracting the average change in potential temperature at a given time and height from the potential temperature change from time t to time $t + 1$ in each case. Figure 19 shows the rate of potential temperature change and its anomaly from the average rate of change.

The positive/negative values of the change rates of potential temperature in the upper and near-ground layers differ in the C→D and D→C cases (Fig. 19a, d). In a C→D, the atmospheric stability increases under 250 m, so the potential temperature increases in the upper layer and slightly decreases toward the ground. On the contrary, in a D→C, the potential temperature decreases in the upper layer and increases toward the ground. As the atmospheric stability changes from stable to weakly stable during a D→C change, such a change likely occurs by enhanced vertical mixing. On the other hand, if vertical mixing is suppressed over an urban area, the potential temperature difference between the upper and lower layers is increased by the relatively high potential temperature in the upper layer. Therefore, during a C→D (D→E), the atmospheric stability under 250 m is increased (decreased) by the suppression (promotion) of vertical mixing at the surface layer.

Panels (b) and (e) of Fig.19 show the changing vertical potential temperature profiles during C→E and

E→C events, respectively. An elevated inversion layer is formed over the mixing layer in urban areas, suggesting that the potential temperature gradient increases through vertical mixing (Ohara *et al.* 1989; Kikuchi 1993). The C→E and E→C changes little affected the potential temperature at heights below 169 m, but remarkably increased and decreased the potential temperature, respectively, at 250 m. Therefore, a C→E (E→C) corresponds to an increased (decreased) bottom height of the elevated inversion layer (the mixing-layer height, Uno *et al.* 1988; Martilli 2002).

In Fig.19, the potential temperature at 205 m and 169 m markedly decreased (increased) during a D→E (E→D) change. The D→C and C→E changes are assumed to promote vertical mixing and decrease the mixing-layer height, respectively. Conversely, the C→D and E→C changes are thought to suppress vertical mixing and increase the mixing-layer height, respectively. These scenarios are summarized in Fig. 20 (a), which plots the height dependence of the change in the vertical potential temperature. The potential temperature change is slightly smaller than in Fig. 19. The potential temperature noticeably decreased at 205 m (D→C and D→E changes), or increased at 169 m and decreased at 205 m (C→D and E→C changes). The vertical profiles of potential temperature changes follow similar trends. Figure 20 (b) shows the height dependence of the change in vertical potential temperature in cases of vertical mixing suppression (C→D) with increased mixing-layer height (E→C), and in cases of promoted vertical mixing (D→C) with decreased mixing-layer height (C→E).

In summary, the vertical structure of the nocturnal potential temperatures under 250 m in the central Tokyo area is governed by suppression (promotion) of vertical mixing, which increases (decreases) the height of the mixing layer (extending from the bottom of the elevated inversion layer to the upper layer). After midnight, the change of cluster C to cluster D (group D), and the subsequent change of cluster C to cluster E (group E), suggest that suppressed vertical mixing and lowered bottom of the elevated inversion layer are different phenomena that occur under independent conditions. However, the temporal variation of the vertical potential temperature becomes more complicated when two or more cases coincide in time.

The surface inversion layer was formed before sunset. When northern winds penetrated the observational area, the inversion layer was elevated (above 50 m) and a ground-based isothermal layer was formed (Kikuchi 1993). The vertical potential temperature profile was altered in half of the similar wind-field

cases. Moreover, the temporal variation of the vertical structure of potential temperatures corresponded with that of the wind system. This suggests that the temporal variation of the wind system affects the temporal variations of groups D and E.

Numerous observational studies have monitored the temporal variations of boundary layer phenomena such as radiative cooling (Kondo 2001), the penetration of land breezes and local fronts (Ohara *et al.* 1989; Kikuchi 1993), and the temperature fluctuations caused by Kelvin–Helmholtz billowing with periods of several minutes in the elevated inversion layer (Uno *et al.* 1992). In this chapter, the temperature data were hourly, precluding observations of these sub-hourly fluctuations. Chapter V and Chapter VI will analyze the shorter time-scale fluctuations in data with higher temporal resolution.

3 Comparison of observed and simulated vertical potential temperatures

Observations and numerical simulations show that the atmospheric conditions over urban areas are better mixed at night than during the day, stabilizing the upper layer. Table 3 shows the nocturnal potential temperature gradients in the surface layer and the elevated inversion layer, along with the height of the inversion layer, obtained in various observations and numerical simulations of urban areas such as Tokyo. Where the potential temperature gradients or the heights of the elevated inversion layer (mixed layer) were not described in the papers, their values were estimated from the figures. As all papers report a stronger potential temperature gradient in the upper layer than in the surface layer, the height of the elevated inversion layer is confirmed as the height of sudden increase of the potential temperature gradient (Uno *et al.* 1988; Martilli 2002). The potential temperature gradient between 205 and 250 m in cluster E (2.7–9.8 ℃ 100 m^{-1}) corresponds to the observed potential temperature gradient in the upper layer. In winter, the bottom of the elevated inversion layer is formed at approximately 200 m.

In summer, clusters A and B accounted for approximately 70% of the cases around sunrise, and cluster E was absent (Fig.17). Therefore, the mixed layer height, which exceeds 250 m, is considered to remain constant throughout a summer night. Previous numerical studies on the Tokyo area reached the same conclusion (e.g., JMA 2013).

The potential temperature gradient in the upper layer is usually stronger in observations than in numerical models. For example, the potential temperature gradient in cluster E of the present study was larger than that obtained by Saitoh *et al.* (1996), who also studied the Tokyo urban area. In our study, the atmosphere of the surface layer was weakly stable (not neutral) in cluster E, and was sometimes stable in cluster D ($\geq$ 1 ℃ 100 m^{-1}). Such atmospheric stability has been reported in previous observational studies (e.g., Yokoyama *et al.* 1974; Uno *et al.* 1988), but numerical studies yield a neutral atmospheric stability with a near-zero potential gradient, even around sunrise (Saitoh *et al.* 1996).

Consistent with other studies, the present study observed a strongly stable layer at tens-to-200 m over the Tokyo urban area in winter. However, the strongly stable layer at similar heights is absent in numerical studies.This discrepancy is usually attributed to vertical resolution and parameterization limitations, but the potential temperature gradients in the surface and upper layers undoubtedly differ between observations and numerical simulations. In particular, observational studies yield a higher atmospheric stability in the surface layer than numerical studies. In some cases, the above-surface layer is also more stable in observational than in numerical studies.

4 Difference of mixed layer height between the present and past

Between the 1960s and 1980s, the nocturnal mixed layer height over the Tokyo urban area in winter was determined as 75–200 m (see Table 3). In the present study, this height ranged from 205 m to 250 m or higher. Note that whereas most of the previous studies were case studies, the present study statistically analyzes numerous cases. Additionally, the bottom of the strongly stable layer was not below 200 m in the 2000s, confirming that the mixed layer height has risen since the 1960s and 1980s. The height difference exceeded 50 m.

Martilli (2002) reported that increasing the building height increases the elevated inversion layer height. The building height around the TT increased between the 1980s and 2000s (see Fig.5), roughening the landscape and promoting vertical mixing. The roughness is attributable to the increased average building height and the large number of skyscrapers built since the 1970s. These changes probably increase the

mixed layer height, other factors such as atmospheric heating from the surface (Saitoh *et al.* 1996; Yu *et al.* 2013) and rural soil moisture (Martilli 2002) can also alter the mixed layer height.

According to observational studies, the mixed layer is 2–5 times higher than the average building height (Kawamura 1977; Uno *et al.* 1989; Kono *et al.* 2010). Numerical simulations yield a similar height ratio of 3–5 (Martilli 2002). In the present study, the mixed layer height (200–250 m) was 6–8 times greater than the average building height (29.6 m), larger than in previous studies. The Tokyo urban area is among the largest in the world, and certainly larger than other Japanese cities such as Sapporo, Hokkaido (Uno *et al.* 1989), Himeji, and Hyogo (Kono *et al.* 2010). It is summarized that the vastness of the city increases the height of the mixed layer in Tokyo. However, the method for estimating the average building height is unclear in most studies. In this study, the minimum building height was obtained as 4.5 m from DSM data. Of course, changing the minimum building height will change the average building height. Therefore, the above-mentioned difference depends on the method of calculating the average building height.

The TMG (1966) derived the wintertime vertical temperature profile between April 1964 and March 1965 from observational data collected at TT, but did not mention the height and vertical temperature gradient of the stable layer in the upper layer. The present study analyzes the vertical potential temperature profile in the 2000s. To clarify the temporal variations in the vertical structure of the potential temperature, the analysis should include pre-2000 data.

Chapter IV Relationship between HII and atmospheric stability

1 Atmospheric stability dependency of HII

Observational studies in rural areas have reported a positive correlation between the HII and the ground-based vertical potential temperature gradient (Sakakibara 2001; Nakagawa 2011). These studies assume neutral atmospheric stability in urban areas (ΔT in Fig. 2). However, stable surface layers (which characterize cluster D; see Chapter III) is sometimes formed over the Tokyo urban area in winter time. Whether atmospheric stability in an urban area is positively correlated with HII is unknown . In winter in Tokyo, the HII is maximized around sunrise (06:00 JST, Takahashi *et al.* 2014). This section analyzes the relationships between the atmospheric stability and HII in this circumstance.

The difference between the temperature in urban areas and the temperature in the windward of the urban area (ΔT) was defined as the difference between the average temperature of two stations in the urban area (Chiyodakukandatsukasachou, Chuuoukuharumi) and the average temperature of four stations in the rural area (Kiyoseshikamikiyoto, Koganeishihonchou, Kodairashiogawachou, Fuchuushimiyanishichou). Figure 21 shows the locations of the abovementioned stations. The atmospheric stability ($d\theta/dz$) was then defined as the gradient of the regression line obtained by correlating the vertical potential temperature profiles at the TT (4–205 m), and ST (10–125 m).

Figure 22 plots the relationships between ΔT and $d\theta/dz$ around each tower at 06:00 JST. The data were collected over 18 nights (see Table 2). Statistical significance was determined at the 1% significance level using t-test (significant correlation coefficients are marked with asterisks). The dθ/dz and ΔT were significantly positively correlated at the ST (Fig. 22a), consistent with previous studies (e.g., Sakakibara 2001). The dθ/dz and ΔT were also positively correlated at the TT (Fig. 22b), although the correlation was looser than the ST correlation, with a smaller correlation coefficient.

The HII is directly proportional not to γ_r (the potential temperature gradient in the surface layer of a rural area), but to $(\gamma_r - \gamma_u)$, where γ_u is the potential temperature gradient in the surface layer of an urban area. Figure 23 plots the dθ/dz at ST and dθ/dz at TT at 06:00 JST. A significant positive correlation is observed. The dθ/dz was approximately four times larger at ST than at TT. Figure 24 correlates the

potential temperature gradient differences at ST and TT. The correlation coefficient is slightly higher than that in Fig. 22a (increasing from 0.792 to 0.813).

These results suggest that the HII is increased by downward sensible heat fluxes caused by vertical mixing of the surface inversion layer, as noted in previous studies (e.g., Tamiya and Ohyama 1981; Nakagawa 2011). The relationship in Fig. 22b indicated that the HII increased when the atmospheric stability at urban area was stable. This seems to contradict the expected increase in HII through the mechanical processes of vertical mixing (see Fig. 2). However, the relationship between the atmospheric stability at the ST and TT showed positive correlation. These relationships suggest that the stable layer over a non-urban area is preserved even when it penetrates the Tokyo metropolitan area.

Previous studies (e.g., Nakagawa 2011) have assumed neutral atmospheric stability in urban areas. However, the atmospheric stability of columns advected from rural areas is non-neutral, and a stable surface layer can form even in large-scale cities such as the Tokyo metropolitan area.

2 Amount of nocturnal air heating over the Tokyo metropolitan area in winter

According to observational studies in small- and mid-scale cities, mechanical vertical mixing contributes more conspicuously to the nighttime UHI than heating from the urban surface (e.g., Sakakibara 2001). However, the contribution of each factor to the formation of UHIs in large-scale cities such as the Tokyo metropolitan area remains unclear.

Several studies have estimated the amount of heat in the air column in the Tokyo area during daytime in summer (e.g., Yoshikado *et al.* 2014; Sugawara *et al.* 2015). However, few studies have estimated the amount of excessive heat in the urban area (relative to that in non-urban areas) during the night. In general, the mixed layer over an urban area is shallower at night than during the day. The nocturnal boundary layer is more susceptible to heating from the surface and mechanical mixing than the daytime layer (Bohnenstengel *et al.* 2011). This section estimates the amount of excessive nocturnal heat in the Tokyo urban area over that in non-urban areas, based on observational data. Furthermore, it examines the contributions of heating from the urban surface and mechanical vertical mixing of the lower-level

inversion layer to the temperature increase in the urban area.

2.1 Vertical potential temperature profiles over urban and rural areas, and the amount of heat

Figure 25 plots the average potential temperature profiles at the TT and ST from 04:00 JST to 06:00 JST on January 1, 2017. The potential temperatures at the TT and the ST differed by approximately 3.5℃ at the ground surface. A strong inversion layer with a potential temperature gradient of approximately 4.1℃ 100 m^{-1} was present at the ST. Conversely, the TT featured a strongly stable layer (3.1℃ 100 m^{-1}) from 205 m to the upper layer and a weakly stable layer (0.9℃ 100 m^{-1}) below 205 m. The potential temperatures at the TT and the ST matched at approximately 100 m (the coincident point), and a crossover was formed above this height. The coincident point was below 250 m in approximately 58% of the clear nights with weak winds (11 out of 18 nights).

Figure 26 shows the vertical variation in the potential temperature difference between the TT and the ST, averaged over 04:00 JST to 06:00 JST. The data for which a coincident point was found below 250 m (Cross-day; triangles) are separated from the data of other cases (NC-day; diamonds). Because the potential temperatures from 130 m to 250 m at the ST were extrapolated from the observed data, the potential temperature differences above 130 m are distinguished by dashed lines in the plot (the solid lines plot the potential temperature differences below 120 m). In Cross-day cases, the curves show a nearly linear decrease in the mean urban potential temperature excess from 4℃ at the surface to 0℃ at 120 m.

Bornstein (1968) reported a crossover in more than two-thirds of analyzed cases that included summer season observations in New York City. The average height of the coincident point was approximately 300 m. Saito (1977) observed a coincident point at 200 m AGL in the averaged vertical distribution of the potential temperature differences between urban (Otemachi) and non-urban (Machida and Koganei) areas in Tokyo (November, 1974). Therefore, the frequency of crossover phenomena is consistent between the present study and other large cities (e.g., New York City), and the crossover height roughly agrees with that of Tokyo in 1974. The height of a coincident point is one of the essential parameters needed to

calculate the amount of excessive heat Q in an urban area, (Eq. 3). In the Cross-day cases (11 cases), Q was calculated using the averaged vertical potential temperature profiles from 04:00 JST to 06:00 JST at the TT and ST. The coincident-point heights and Qs were averaged over the 11 cases, 123 m and 221 kJ m^{-2} , respectively (Table 2).

2.2 Wind system and air-temperature distribution under clear conditions with weak winds

Figure 27 is a composite map of the temperature deviation from the average spatial temperatures (contours) and the wind system (barbs) on Cross-days in the Tokyo Wards and its surrounding areas, averaged from 04:00 JST to 06:00 JST. In Fig. 27, the dashed, solid, and thick lines indicate negative, positive, and zero temperature deviations, respectively.

Northwesterly winds dominated over the target area. The contour of zero temperature (thick line) runs from the northern part of the Tokyo Wards area (the Itabashi and Adachi Wards) to the southwestern (the Setagaya Ward) and southeastern (the Koto Ward) parts. The basic features of the nighttime temperature distribution shown in Fig. 27 are consistent with those of previous studies (e.g., Takahashi *et al.* 2014). Figure 28 shows the horizontal profile of the temperature deviation from the spatial temperature along the ST–TT cross-section in each case. Note that the air temperature was almost constant from the ST to the western periphery of the Tokyo Wards area (e.g., the Suginami Ward), and began rising in the western part of the Tokyo Wards area (the Nakano Ward) before gradually increasing toward the TT.

2.3 Heat budget of the air column moving from the ST to TT

To estimate the heating rate of the air column, we assumed that the air column moved from the ST to the TT and was heated from the Suginami Ward to the TT.

The wind speed at the coincident point (123 m) at the ST was estimated by averaging the wind speeds from 01:00 JST to 06:00 JST at various heights (Table 4). The result was approximately 4.0 m s^{-1}. Taking the distance over which the temperature increased between the Suginami Ward and the TT ($\sim$9.5

km), and assuming that the air column moved at 4.0 m s^{-1}, the air column moved from the Suginami Ward to the TT in approximately 0.6 hours (2375 s). Dividing the average amount of heating (221 kJ m^{-2}) by the total travel time between the Suginami Ward and the TT (2375 s), the heating rate of the air column was approximated as 93 W m^{-2}. In contrast, the heating rate of the daytime sea breeze during summer in Tokyo is approximately 600 W m^{-2} (Yoshikado *et al.* 2014). This indicates that in Tokyo, the heating rate of the air column during a typical winter night is approximately 15% of that of a typical summer day.

We now estimate the contribution of each term in Eq. 4 to the nighttime heating rate of the air column in Tokyo. In Basel City, Switzerland, Christen and Vogt (2004) approximated the same values for the nighttime heat balance Q_s and the anthropogenic heat generation Q_{ant} (namely, 20 W m^{-2}), but did not consider the temporal variations. Kusaka and Kimura (2004) estimated the surface energy balance at an urban site using an urban canopy model with an additional anthropogenic-heat term. They obtained a sensible heat flux of 10–20 W m^{-2} at midnight. Therefore, in the present study, 20 W m^{-2} was assumed as the typical nocturnal Q_s in urban areas at night. Meanwhile, the estimated Q_{ant} in central Tokyo is 5–20 W m^{-2} summer mornings (e.g., JMA 2005). Substituting Q (93 W m^{-2}), Q_s (20 W m^{-2}), and Q_{ant} (5–20 W m^{-2}) into Eq. 4, the residual (Q_e + Q_{rad}) was estimated as 53–68 W m^{-2}. Sugawara *et al.* (2015) estimated the Q_{rad} during summer daylight as -3 W m^{-2} to 22 W m^{-2} from radiosonde measurements. The humidity profiles required for estimating Q_{rad} were unavailable, but the weather conditions of the present analysis (clear winter nights with weak wind) imply a negative Q_{rad} (i.e., radiative cooling). Consequently, the Q_e should exceed 53–68 W m^{-2}; that is, Q_e should be roughly three times larger than Q_s and larger than (Q_s + Q_{ant}). Although this result is preliminarily estimated from the reported values of other urban areas, it suggests that the temperature difference between the urban and non-urban areas of the Tokyo metropolis is considerably more influenced by the downward sensible heat flux caused by vertical mixing of the surface inversion layer than the sensible heat flux from the urban surface.

Chapter V Characteristics of the temperature distribution and wind system

1 Temperature distribution and wind system

Takahashi *et al.* (2014) characterized the temperature distribution and wind system during nights with large HII in the Tokyo metropolitan area. They also related the HII to the weather conditions (e.g., cloud amount and wind speed). Even if under same weather conditions, HII differ in each case (Chapter IV). Therefore, the relationships between HII and the temperature distribution, and between HII and the wind system, remain contentious.

Because the averaged ΔT and Δ(dθ/dz were 4.5℃ and 3.0℃ 100 m^{-1} in Fig. 24, we can distinguish two categories of HII nights: 1) large-HII nights (6 nights) with $\Delta T > 4.5$℃, and 2) small-HII nights (9 nights) with $\Delta T < 4.5$℃and Δ(dθ/dz) > 3.0℃ 100 m^{-1}. Three days were not included in both categories because their ΔT and Δ(dθ/dz did not satisfy the abovementioned conditions. Figures 29 and 30 show the composite maps of temperature distribution (contours), temperature deviations from the average spatial temperature (shaded regions), and the wind systems (barbs) in the Tokyo Wards and its surrounding areas during large- and small-HII nights, respectively. The data are plotted at 3-hour intervals starting from 18:00 JST.

On large-HII nights, northwesterly winds dominated until 21:00 JST. After 24:00 JST, the winds turned westerly around the western part of the Tokyo Wards area (e.g., the Suginami Ward), and the wind speed decreased. In the urban area, the wind speed was higher than in the western part of the Tokyo Wards area, and did not decrease. Throughout the night, the temperature deviations from the 0.0℃ contour line extended from the northern part of the Tokyo Wards area (the Itabashi and Adachi Wards) to the southwestern (Setagaya Ward) and southeastern (Koto Ward) parts. A heat cliff in this area was formed after 24:00 JST. The temporal variations in the nighttime temperature distribution and wind system (Fig. 29) are consistent with those of previous studies (e.g., Yamashita 1996; Takahashi *et al.* 2014).

On small-HII nights, the target area was dominated by northerly winds after 24:00 JST. The temperature deviations from the 0.0℃ contour line spatially coincided with those on the large-HII nights, but the horizontal temperature gradient was smaller than on large-HII nights.

Whereas the average WD veered west after midnight on large-HII nights, northerly winds dominated throughout the small-HII nights. To clarify the temporal variation of the wind system, Figs. 31 and 32 plot the wind-rose distributions at two-hourly (121 min) intervals during large- and small-HII nights, respectively. On small-HII nights, the northerly wind was clearly developed in the Tokyo Wards area after midnight (Fig. 32). On large-HII nights, the winds were northwesterly and westerly in the urban area and the west-Tokyo area, respectively, between 23:00 JST and 01:00 JST (Fig. 31). At this time, the prevailing WD from the Setagaya Ward to the Nerima Ward was not clarified. We emphasize that this area coincided with the heat cliff.

The Panels (a) and (b) of Fig. 31 superimpose the wind-rose distributions on the plots of temperature difference versus potential temperature-gradient difference in Suginamikukugayama (Sugi) and Shibuyakuudagawachou (Shib), respectively, between 23:00 JST and 01:00 JST. Northerly winds developed on most of the small-HII nights at both stations. When ΔT exceeded 4.5℃, northwest and southwest winds were frequent at Sugi, whereas northeasterly or southwesterly winds clearly prevailed at Shib. This suggests that when ΔT is large, the WD varies around the heat cliff.

2 Nocturnal heat island circulation in winter

There are two known types of urban boundary layer: urban domes when the regional wind is weak (Fig. 34a), and urban plumes when the regional wind is moderate or strong (Fig. 34b) (Oke *et al.* 2017). Laboratory and numerical studies (e.g., Kimura 1975; Mori and Niino 2002; Niino *et al.* 2006) have identified two heat island circulation (HIC) patterns in urban domes: type-E, in which the HIC develops over the edge of the urban core (Fig. 34c), and type-C, in which the HIC centralizes over the urban core (Fig. 34d). Niino *et al.* (2006) showed a type-E to type-C transition in a flow regime governed by two non-dimensional parameters (ε_n and α, see Fig. 5 of Niino *et al.* 2006).

$$\varepsilon_n = \frac{\Delta\theta}{\gamma\,\delta}, \tag{7}$$

and

$$\alpha \equiv \frac{\delta}{l}. \tag{8}$$

In these expressions, $\Delta\theta$ is the potential temperature difference between the urban and non-urban areas, γ denotes the potential temperature gradient, and δ and l are the vertical and horizontal scales of the heat island, respectively.

Niino *et al.* (2006) applied the above flow regime to a typical daytime heat island. Their estimated ε_n and α ranges were 1–30 and 0.01–0.1, respectively. These values suggested that both type-E and -C can be realized in the atmosphere, but type-C may occur more frequently.

Here, we apply the same flow regime to clear, low wind nights in the Tokyo area on large-HII days. The four parameters (ΔT,γ , l and) were obtained as follows. Firstly, ΔT was defined as the temperature at urban area and rural area are defined as the average temperatures at two stations at the center of the urban area (Kandakutsukasachou and Chuuoukuharumi) and at three stations outside of the heat cliff (Setagayakuseijou, Suginamikukugayama and Nakanokuwakamiya), respectively. Next, γ was defined as the vertical potential temperature gradient at ST. Next, l is defined as the distance between the Suginami and Chiyoda Ward (15 km) because the heat cliff is formed around the Suginami Ward. Finally, δ was assumed as 200 m, the height at which the elevated inversion layer sometimes forms. As l and δ are constants, α is also constant (0.013). The relative frequency of ε_N at 10-min intervals from 20:00 JST to 06:00 JST in large-HII nights is shown in Fig. 35. Therefore, the flow regime is depended on only ε_N. The nighttime ε_N are < 1.0, smaller than daytime-reported value (Niino *et al.* 2006). According to Niino *et al.* (2006), the threshold value of ε_N between above two types is larger than 3 at α =0.013. From the estimated ε_N and α, the HIC pattern in the study area was assumed as type-E. In our study area, the nighttime $\Delta\theta$ and γ are larger than their daytime values, and δ was lower than its daytime value.

Note that this flow regime was derived mainly from the surface temperature differences, whereas in the atmosphere, there are other causes which affect to wind flow, for example, distribution of roughness length. However, it is concluded that type-E patterns are commoner at night than during the daytime. In type-E, the HIC develops over the edge of urban area. This suggests difference of wind flows between urban and non-urban areas. The characteristics of wind roses at Suginamikukugayama and Shibuyakuudagawachou

may indicate this difference of wind flows. Additionally, this difference may lead to the formation of the heat cliff. The relationships between wind and the heat cliff is analyzed in next chapter.

Chapter VI Relationships between wavelike variation and UHI

1 A case study of wind and temperature variations

On large HII-nights, the prevailing WD was unclear in the western part of the Tokyo Wards area, and a north-westerly wind developed in the urban area (Chapter V). The wind and temperature exhibit wavelike intermittent motions in the nocturnal stable boundary layers (e.g., Yokoyama *et al.* 1981; Sun *et al.* 2015; Lyulyukin *et al.* 2015). As the atmospheric stability is approximately four times higher over rural areas than over urban areas (Chapter IV), the fluctuations probably differ between the two types of areas. To analyze the wind variation, the three nights are analyzed: January 11–12, 2017 (Case-1), January 09–10, 2017 (Case-2), and November 16–17, 2016 (Case-3). The fluctuation of wind developed at several observational stations in Cases-1 and 2. Northerly winds dominated throughout the night in Case-3.

1.1 Case-1 (January 11–12, 2017)

Figure 36 shows the temporal variations in the wind direction (WD), zonal (U), and meridional (V) components of the wind speed, and the temperature deviation from the 61-min moving-average (T') at Nakanokuwakamiya (Naka), Suginamikukugayama (Sugi), Shibuyakuudagawachou (Shib) and Megurokuhimonya (Megu). Positive U and V indicate westerly and northerly winds, respectively. The winds at Naka and Sugi fluctuated between southwesterly and northerly from 23:00 to 02:00 JST. The temperature T' fluctuated accordingly, and tended to be positive in northerly winds (positive V). The prevailing winds became westerly after the fluctuations (02:00 JST). Figure 37 shows the correlation coefficient lags between V and T' from 23:00 to 02:00 JST at Naka and Sugi. The correlations were positive near ΔTime =0. On the contrary, the U, V and T' fluctuations were small and the periodic motions were unclear at Shib and Megu. At 02:00 JST, the WD at Shib and Megu shifted from northerly to southwesterly. Hereafter, we focus on the wind and temperature fluctuations.

To analyze the period of the wind and temperature fluctuations, the time-series of the wavelike motions were subjected to Morlet wavelet analysis. As V was larger than U at Sugi and Naka, the wavelet analysis

at the four stations was performed on V and T'. The time–frequency distributions of V and T' are displayed in Figs. 38 and 39, respectively. Periodic maxima both in V and T', with wave periods of 20–50-mins, appear in the Naka and Sugi analyses between 23:00 and 01:00 JST. In contrast, no clear periodic maxima appear in the Shib and Megu analyses during this period. The strong signal at Shib around 02:00 JST resulted from the shifted WD (Fig. 36).

To clarify the regional characteristics of the wind fluctuations, the changes in WD between 23:00 and 02:00 JST (181 mins) were counted at each station (Fig. 40). Calm periods (wind speed ≤ 0.1 m s^{-1}) were omitted. Only one or two northerly winds dominated at the east of the Setagaya Ward (excepting the Chiyoda Ward). Frequent changes in WD occurred from the southern part of the Nerima Ward to Tama City. No prevailing WD appeared in this area. At Sugi, the WD changed every three minutes.

For a detailed analysis of the horizontal characteristics of the wavelike motion, Fig. 41 plots the 5-min moving-averaged winds in Case-1 at six stations recording frequent changes in WD: Fuchuushimiyanishi-chou (Fuch), Koganeishihonchou (Koga), Musashinoshisekimae (Musa), Suginamikukugayama (Sugi), Nakanokuwakamiya (Naka) and Nerimakunerima (Neri) and Otemachi (Otem). The 20–60-mins band-pass filtered V (V') are also shown (except at Otem, where the data were collected at 10-min intervals). Northerly winds dominated between 19:00 and 22:00 JST. A westerly wind developed in Fuch after 22:00 JST, and except at Otem, the westerly and northerly winds thereafter fluctuated periodically until 02:00 JST. At Fuch, the time when wind fluctuations occurred seemed to be earlier than that at Neri. Therefore, the wavelike variation might move eastward. The periodic motion degraded after 03:00 JST, and a westerly wind (WSW–WNW) dominated until 05:00 JST. Notably, the northerly winds persisted at Otem between 22:00 JST and 02:30 JST, when the wavelike motions appeared at the other sites. The wind at Otem shifted to westerly after 02:30 JST.

To analyze the formation processes of the UHI and the heat cliff, we calculated four averaged temperature (T_1, T_2, T_3, and T_4) as follows. First, T_1 is defined as the temperature of the urban area obtained by averaging temperatures of two stations (Kandakutsukasachou and Chuuoukuharumi). Next, T_2 is defined as the temperature of the urban side of the heat cliff obtained by averaging temperature of three stations (Shibuyakuudagawachou, Setagayakusetagaya, and Megurokuhimonya). Next, T_3 is

defined as the temperature of the outside of the heat cliff obtained by averaging temperatures of three stations (Nakanokuwakamiya, Suginamikukugayama, Setagayakuseijou). Finally, T_4 is defined as the temperature of the west of the Tokyo Wards area obtained by averaging temperatures of four stations (Fuchuushimiyanishichou, Koganeishihonchou, Kodairashiogawachou, and Kiyoseshikamikiyoto). The locations abovementioned stations are shown in Fig. 21. Then, the temperature differences between T_1 and T_4 and between T_2 and T_3 are referred to as the heat island intensity and the heat cliff intensity, respectively. Figure 42 plots the temporal variations of these temperatures and the temperature differences. Because T_3 and T_4 decreased more rapidly than T_1 and T_2 until 19:00 JST, the temperature differences increased over this period. T_3 suddenly decreased after 22:00 JST (-0.7 ℃ 10 min^{-1}), when the wind fluctuations started around the Suginami Ward. On the contrary, T_2 linearly decreased between 19:00 and 06:00 JST, leading to rapid heat cliff formation.

Next, the temporal variations of the vertical potential temperatures and potential temperature gradient profiles were determined at TT (Fig. 43) and ST (Fig. 44). The atmospheric stability under 250 m at the TT was nearly neutral until 01:00 JST. Between 02:00 and 04:00 JST, the potential temperature gradually decreased at heights under 64 m, but remained constant between 103 and 205 m. Consequently, the potential temperature gradient increased between 64 m and 103 m. Above 205 m, it fluctuated after 02:00 JST. The potential temperature reduced more slowly than in the upper layer. A ground inversion layer was formed at the ST.

Figure 45 shows the temporal variations in the fluctuation component of the potential temperature (θ') at TT. θ' is the deviation from the 61-mins moving-average. θ' were small at all heights between 20:00 and 02:00 JST, and increased at heights above 169 m after 03:00 JST. In the upper layer around the tower, the fluctuations tended to be larger in magnitude than in the lower layer, and tended to begin earlier. In addition, the fluctuations were small below 64 m. The fluctuations began increasing at the time of the northerly-to-westerly wind change at Otem.

1.2 Case-2 (January 09–10, 2017)

Figure 46 shows the temporal variations of WD, U, V and T' at Naka, Sugi, Shib, and Megu in Case-2. The WD fluctuated at Sugi and Megu between 23:00 and 01:00 JST, but persisted in the northwest direction at Naka. The fluctuation period was approximately 30 minutes. The U and V fluctuations could not be estimated at Shib, where the wind speed was very low.

Figure 47 shows the frequencies of the changes in WD (similar to Fig. 38 but for Case-2). Only one or two northerly winds dominated in the northern parts of the Tokyo Wards areas such as the Nakano and Kita Wards, and directional changes were rare. In other areas, including the Suginami and Chiyoda Ward, the westerly winds frequently changed direction, and no prevailing winds were evident.

Figure 48 plots the 5-min moving-averaged winds and V' in Case-2 at Fuch, Sugi, Naka, Otem, Setagayakuseijou (SetW), Setagayakusetagaya (SetE) and Megurokuhimonya (Megu) for Case-2. The northerly wind dominated at each station between 19:00 and 23:00 JST. The wind direction at all stations except for Naka, and V' fluctuated after 23:00 JST. The V' minimum moved eastward from Fuch to Megu. Although no clear WD fluctuations appeared at Shib (Fig 46), the wind direction at Otem shifted to westerly after 23:00 JST. Recall that in Case-1, wavelike motions were absent at Shib and Otem, and the northerly-to-westerly wind change occurred approximately 2.5 hours after the fluctuation at Sugi. In Case-2, the wind-direction change at Otem lagged that at Sugi by up to one hour.

Figure 49 plots the temporal variations of T_1, T_2,T_3, T_4 and their differences in Case-2. This plots are similar to Fig. 42 in Case-1. T_3 decreased after 23:00 JST when the fluctuation started at Sugi, increasing ($T_2 - T_3$). T_2 also decreased at this time, so the heat cliff was unclear compared with Case-1.

The temporal variations of the vertical potential temperature and potential temperature gradient profiles were determined at TT (Fig. 50) and ST (Fig. 51). At the TT, the atmospheric stability under 250 m was nearly neutral until 23:00 JST. Above 169 m, the potential temperature gradient increased and the potential temperature fluctuated between 23:00 and 03:00 JST. The elevated inversion layer was formed at this time. From around 23:00 JST, the potential temperature fluctuated above 103 m. A ground-based inversion layer with a height exceeding 125 m was formed throughout the night. The potential temperature above

90 m fluctuated between 23:00 and 01:00 JST.

Figure 52 shows the temporal variation of θ' at the TT. At all heights, θ' remained small until 22:00 JST. The fluctuations increased above 169 m after 23:00 JST. At heights above 169 m, the fluctuations increased after 23:00 JST. The fluctuations exhibited larger magnitude, and tended to begin earlier, in the upper layer than the lower layer. Fluctuations remained low under 64 m. The amplitudes increased at the time of the northerly-to-westerly wind change at Otem. These features are consistent with those of Case-1.

1.3 Case-3 (November 17–18, 2016)

Figure 53 shows the variations of WD, U, V and T' at Naka, Sugi, Shib and Megu in Case-3. At each station, a northerly wind persisted through the night. The U, V and T' were considerably more stable than in Cases-1 and 2.

Figure 54 plots the temporal variations of T_1, T_2,T_3, T_4 and their differences in Case-3. This plots are similar to Fig. 42 in Case-1. As the temperatures decreased at uniform rates until 19:00 JST, the temperature differences fluctuated little during this time. The T_2-T_3 increased after 24:00 JST, but never exceeded 2.0℃. Therefore, no obvious heat cliff was formed.

The temporal variations of the vertical potential temperatures and potential temperature gradient profiles were determined at TT (Fig. 55) and ST (Fig. 56). The atmospheric stability at the TT was nearly neutral throughout the night, and an elevated inversion layer was not formed. A ground-based inversion layer developed at the ST, but the potential temperature gradient at this site was smaller than in Case-1 and Case-2. Figure 57 presents the time series of θ' at each height of at TT. This plot is similar to Fig. 45 in Case-1. At all heights, the θ' amplitudes remained small throughout the night.

2 Characteristics of wavelike variation

2.1 Period of wavelike variation

In Case-1 and Case-2, ground-based inversion layers were formed at the ST and periodic variations were observed some stations. In a stable layer, the Brunt-Väisälä oscillation (BVO) is known as one of periodic variation in stable layers (e.g., Holton 2004).

The frequency (N) and period (T) of the BVO are respectively given by

$$N = \sqrt{\frac{g}{\theta + 273.15} \times \frac{d\theta}{dz}}\,, \tag{9}$$

and

$$T = \frac{2\pi}{N}\,, \tag{10}$$

where g, θ and $d\theta/dz$ are the gravitational acceleration (9.8 m s^{-2}), the average potential temperature at the ST (10 m, 20 m,40 m, 90 m, and 125 m AGL), and the potential temperature gradient at the ST, respectively. The potential temperature gradient was obtained by regressing the potential temperature against the height AGL.

Figure 58 shows the temporal variations of the BVO period, the potential temperature gradient at the ST (10–125 m) and the lower (4–205 m) and upper (205–250 m) layers of the TT for Case-1. The atmosphere at the ST was strongly stable (2.0 ℃ 100 m^{-1}) until 01:00 JST. Thereafter, the potential temperature gradient increased to 5.0℃ 100 m^{-1} around sunrise. Meanwhile, the lower layer at the TT was atmospherically neutral until 24:00 JST, and weakly stable (0.9 ℃ 100 m^{-1}) at 06:00 JST. In the upper layer at the TT, the potential temperature gradient was relatively constant up to 02:00 JST, then fluctuated between 0.0 and 1.6℃ 100 m^{-1} as the wind direction shifted to westerly at Otemachi. Between 22:00 and 24:00, the BVO period was approximately 4 minutes, 5–10 times shorter than the observed wavelike motion period at Sugi and Naka (20–50 mins, Figs. 38 and 39). Assuming constant θ, the periods of the BVO and observed wavelike motion can be reconciled only if $d\theta/dz$ is neutral (0.08–0.005 ℃ 100 m^{-1}). Figure 59 shows the temporal variations of the potential temperature gradient

around the ST and in the lower and upper layers around the TT, along with the BVO period, in Case-2. Between 23:00 and 01:00 JST, when the winds fluctuated at Sugi, the BVO period was 2–4 min, clearly shorter than the period of the wavelike wind motions at Sugi (see Fig. 46).

Observed wind periods in Cases-1, and -2 were clearly longer than BVO periods. Yokoyama *et al.* (1981) observed the wavelike motion of wind with period of 10–20 times the BVO period at Nerima. The ratios of the BVO periods observed in the present cases are roughly consistent with those of previous studies (Yokoyama *et al.* 1981; Sun *et al.* 2015).

2.2 Propagation of wavelike variation

In Case-1 and Case-2, wavelike variations seemed to move eastward (Figs. 41 and 48). To clarify the horizontal propagation of the wavelike motion, the times of maximum V (northerly wind) or minimum V (southerly wind) were read from the temporal wind behaviors in Case-1 as follows. The winds and the real part of the wavelet coefficient for V temporal variations are shown in Fig. 60 during 22:00 and 01:00 JST. In this figure, the wavelet coefficient are averaged during 20 and 50 mins because the wavelike variation period are 20–50 mins. Moreover, red triangles indicate the coefficient maxima and V > 0, and blue triangles indicate the coefficient minimum and V $\leq$ 0. In addition to this, these triangles are connected as the propagation of wavelike variation. According to this figure, two propagation patterns (P_1 and P_2) can be obtained. First, P_1 derived from only the coefficient temporal variations. However, northerly WD at Sugi, Naka, and Neri developed before 23:15 JST even though WD changed to westerly at Fuch and Koga before this time. Therefore, it is difficult to refer to P_1 as a propagation of wavelike motion. Next, P_2 derived from coefficient and WD temporal variation. For example, WD at Musa, Sugi, Naka changed to westerly at approximately 23:05, 23:45, and 23:50 JST, respectively. These times are referred to as propagation times. Therefore, P_2 is assumed to as propagation of wavelike variation in this study.

Distributions of above-mentioned times (P_2) are plotted in Figure 61. Periodic motions were not evident at some stations (marked with x in the figure). During the night, the maximum and minimum fronts

moved from Fuchu to Nerima. From the de-clarified wavelike motion of the Fuchu-to-Nerima movement in the urban area, we could locate the boundary of the wavelike motion. This boundary was consistent with the heat cliff (Fig. 29). Moreover, the time difference and distance between Fuch and Neri are 125 mins and 20 km, respectively. As a result, the propagation speed of the wavelike variation is obtained as 2.7 m s^{-1}.

A wavelike motion in stable layer has a characteristic of shallow water wave (Yokoyama *et al.* 1983). A phase speed of the shallow water wave (c) is given by

$$c = \overline{u} \pm \sqrt{\frac{\theta}{\Delta\theta} \times g\, H}\,, \tag{11}$$

where $\overline{u}$, g, H, θ and $\Delta\theta$ are average wind speed, gravitational acceleration (9.8 m s^{-2}), height of inversion layer, potential temperature at bottom of inversion layer, and potential temperature different between top and bottom of inversion layer, respectively (Yokoyama *et al.* 1983).

In this study, $\overline{u}$ is defined as the average wind speed at Sugi between 23:00 and 02:00 JST in Case-1 (1.0 m s^{-1}). H (125 m), θ (279.4 K) and $\Delta\theta$ (2.7 K) are obtained from vertical potential temperature profile at ST (Fig. 44), respectively. As a result, c is estimated as 1.0$\pm$3.5 m s^{-1}. This value is consistent with the observed propagation speed of wavelike variation. In addition to this, it agrees with previous studies such as estimated phase speeds at Nerima Ward (Yokoyama *et al.* 1983) and propagation speeds observed by Doppler radar in Chiba Prefecture (Kusunoki *et al.* 2000).

On the other hand, the other propagation speed in P_1 is estimated as 10.8 m s^{-1} (Fig. 60). This speed may be too fast compared with wind speed (approximately 1.0 m s^{-1}). Further insight into this propagation speed of wavelike variation is left to future work. However, it seems reasonable to conclude that the wavelike motion propagated to eastward and did not develop over the center of the Tokyo metropolitan area.

2.3 Generation of wavelike variation

There are some causes, which produce wavelike motion such as: 1) topography (e.g., Yokoyama *et al.* 1984), 2) vertical windshear (e.g., Ohya *et al.* 2008), and the 3) convergence between background flow and density currents (e.g., Sun *et al.* 2015). Sun *et al.* (2015) observed the wavelike motions of temperatures and wind speeds and suggested that such motions result from the convergence of background flow and density currents. They referred to the observed wavelike motion as gravity wave (GW). In Case-1 and Case-2, the wavelike motion developed in areas where the northerly winds passing through urbanized areas such as Saitama intercepted by the western cold current. Therefore, This supports that the wavelike motions were GW generated by the convergence of the northerly and westerly flows (Fig. 62a).

Figure 62b illustrates the effects of the wavelike wind and temperature motions. When V' $<$ 0, the penetration of cold and stable westerly flow reduces the surface air temperature. Conversely, when V' $>$ 0, the surface layer receives positive sensible heat and momentum from the upper northerly wind layer. The vertical motion enhances vertical mixing. A downward sensible heat flux is also generated by mechanical mixing in the stable surface layer. Consequently, $\overline{V'T'}$ indicates positive (Fig. 37).

In Case-1, the penetration of the westerly wind apparently stagnated around the Shibuya Ward until 02:00 JST. Because a near-neutral urban boundary layer develops in the Shibuya Ward, the energy of an GW arriving in the region is vertically displaced, and the wavelike motion is less clear than in rural areas such as Sugi (Fig. 63a). Therefore, the different wind fluctuations on the suburban side (e.g., the Suginami Ward) and the urban side (e.g., the Shibuya Ward) suggest a change in the atmospheric stability between these areas.

After 02:00 JST, the wind reduced in amplitude and its direction shifted westward at each station (Figs. 36 and 41). The wind shift indicates a penetration of cold current (westerly wind) into the urban area (Fig. 63b). At that time, the potential temperature fluctuations at the TT increased at heights above 169 m (Fig. 45), suggesting an perpendicular movement of the bottom of the elevated inversion layer (Ohara *et al.* 1989). The height at which the potential temperature fluctuates widely agrees with that of Ohara *et al.* (1989).

Previous observations were limited to one location (Yokoyama *et al.* 1981), or to homogeneous topographies within hundreds of square meters (Sun *et al.* 2015). The regional characteristics of these wavelike motions have not been investigated in metropolitan areas or in heterogeneous rural–urban areas with different surface conditions. The present study elucidated the wavelike motions and their regional characteristics over a larger area (tens of square kilometers) than in previous studies.

3 Relationships between wind system and temperature distribution

Mori and Niino (2002) suggested three distinct flow regimes in the formation processes of horizontal convections: the diffusion regime, the gravity current regime, and the gravity wave regime. Niino *et al.* (2006) derived the time T_{GW} (T_{GC}) required for a gravity wave (gravity current) to reach the center of a heat island. They suggested that gravity waves initiated from the edge of the heat island arrive at its center when $T_{GW} < T_{GC}$. Note that these regimes were derived solely from the surface temperature differences (Mori and Niino 2002), whereas in the present study, wavelike motions are generated by the convergence of two wind flows. The wavelike variations of temperature and wind at Sugi and Naka in Case-1 (Fig. 36) suggest that the gravity wave regime (23:00–02:00 JST) progressed to the gravity current regime (after 02:00 JST). On the contrary, the gravity wave regime was probably bypassed at Shib, and the gravity current regime developed after 02:00 JST (Fig. 36). In Case-2, both the gravity wave and gravity current regimes were thought to develop at Sugi (as in Case-1), but the endurance time of the gravity wave regime was shorter than in Case-1. Owing to the weak winds at Shib and the low temporal resolution (10-min data interval) at Otem, whether the gravity wave regime developed in the urban area cannot be concluded. However, the temporal wind variations suggest that a gravity current developed at Otem.

We can now relate the wavelike motions to the heat cliff. In Case-1, the westerly wind penetrated eastward from west of the Tokyo and a GW was generated. This penetration led to the decreasing temperature at the western part of the Tokyo metropolitan area. The GW arrived near Sugi, but it cannot penetrate to the urban area owing to near neutral layer. Hence, a clear heat cliff developed. According to

Niino *et al.* (2006), HIC basically develops at the western part of the Tokyo Ward area and suppresses a penetration of westerly cold current, forming the heat cliff. After that, the gravity current penetrated to the urban area. The time when the wind direction changed to west at Shib was same as that at Sugi. It is expected that penetration of cold current promotes temperature decreasing. The temperature decreasing rate did not change in the urban area. The downward sensible heat from the elevated inversion layer probably suppress the temperature decreasing in a surface layer (Uno *et al.* 1988).

In Case-2, the westerly wind appeared to penetrate the Shibuya Ward without stagnating. The penetration increased the potential temperature gradient in the lower layer around the TT, suggesting that the stable layer over a non-urban area is preserved even when the air column penetrates an urban area. Therefore, the temperatures decreased at similar rates in the urban and rural areas of Tokyo, and no obvious cliff was formed. However, although Case-2 is included in the small-HII days (Chapter V), which are dominated by northerly winds, its wind field differs from those of other small-HII days. Whether the penetration of westerly winds observed in Case-2 is a common phenomenon raises some interesting questions.

In Case-3, northerly wind dominated nighttime. The heat cliff was unclear, the atmospheric stability was nearly neutral, and the temperature fluctuations at the TT were small. Using Doppler LIDAR and radiosonde observations, Oda *et al.* (2011) investigated the structural characteristics of the atmospheric boundary layer over Koganei, Tokyo, on February 21 of 2010. They reported near-neutral atmospheric stability and low vertical-velocity fluctuations below 1 km during the night (03:50–04:30 JST). Figure 64 shows the wind system, temperature distribution, and temperature deviation from the spatial average around the Tokyo Wards during the night of February 20, 2010. At Otemachi, the wind speed and WD from 18:00–06:00 JST were averaged as 3.4 m s^{-1} and north-northwest, respectively. A northerly wind dominated throughout that night in Tokyo. The horizontal temperature gradient was small around the Suginami Ward, where the heat cliff is sometimes formed. The average wind speed was stronger than in the present study, which focused on clear nights with weak winds, but the wind system resembled those in Case-3 and small-HII days (Chapter V). Figure 65 shows the temporal variations of the potential temperature and its gradient at the TT. The atmospheric stability was neutral from the surface to 250

m. These results imply that when northerly winds dominate throughout the night, the zone of neutral atmospheric stability in urban Tokyo extends to hundreds of meters AGL. The potential temperature gradient at the ST tended to be small. The heat cliff was smeared by dispersal of heat from the surface, which eventually exerts a uniform heating effect.

4 Nocturnal urban boundary layer in Tokyo metropolitan area

4.1 Characteristics of nocturnal vertical potential temperature profiles

The vertical potential temperature distribution was separated into five categories. During summer months (May–August), the ground-based mixed layer formed at night and its height was at least 250 m deep. This result is consistent with previous numerical simulations of the Tokyo urban area. During winter months (November–February), the bottom height of the elevated inversion layer with strong atmospheric stability ($2.0 < \gamma$) was approximately 200 m or more above 250 m (cluster E). Moreover, stable layer from the surface to the upper layer (1.0–γ–1.5) was formed (cluster D). These atmospheric stabilities in the surface layer and its upper layer were consistent with previous observational studies. The observed stabilities tended to be higher than the previously simulated values.

In winter, the temporal variation of the vertical potential temperature profile (from the surface to 250 m above the Tokyo urban area) was well explained by the suppression (promotion) of vertical mixing, which increased (decreased) the bottom height of the elevated inversion layer.

The atmospheric stability at urban area has been assumed near neutral. However, this study indicated its diversity and temporal variations.

4.2 Relationships between atmospheric stability in urban area and HII

There is a positive correlation between atmospheric stability at the Tokyo metropolitan area and the HII (Fig. 22b). This relationship indicates the HII tends to increase when the atmospheric stability at urban area was stable. This seems to contradict the expected increase in HII through the mechanical processes of vertical mixing (Fig. 2). However, the relationship between the atmospheric stability at the ST and TT also showed positive correlation. These relationships suggest that the stable layer over a non-urban area

is preserved even when it penetrates the Tokyo metropolitan area.

The atmospheric stability of columns advected from rural areas to urban area has been assumed to be near neutral. However, it is non-neutral, and a stable surface layer can form even in large-scale cities such as the Tokyo metropolitan area.

4.3 Mechanism of the heat cliff

According to the flow regimes derived by Niino *et al.* (2006), the HIC pattern in nighttime was assumed as type-E (Fig. 34). In type-E, the HIC develops at the edge of the urban area. Therefore, this suggests difference of wind flows and atmospheric stability between urban and non-urban areas.

In winter nighttime, GW was generated by the convergence of the northerly and westerly flows at the west of the Tokyo metropolitan area and it moved to eastward. Penetration of GW reduces the temperature at non-urban area. On the contrary, the GW was dispersed around the boundary non-urban and urban areas owing to near neutral atmospheric stability at urban area. Therefore, decreasing rate of the temperature at urban area does not change. Consequently, the clear heat cliff was formed. However, the stable layer on a non-urban area was sometimes preserved even if it penetrates to the urban area (Case-2). In these days, the heat cliff was unclear. The westerly wind was suggested to affect the nocturnal urban boundary layer and the horizontal temperature distribution.

Chapter VII Conclusions

This study characterized the nocturnal urban boundary layer and related it to the distribution of surface air temperature and the wind system in the Tokyo metropolitan area. The temperature values at the TT were validated prior to analysis. Although the vertical potential temperature profile in the surface layer was expected to be neutral under strong-wind conditions, the potential temperature in the top 2% of wind speeds (based on the dry adiabatic lapse rate) was higher at some specific heights than at others. The potential temperature at each height was statistically corrected, assuming that the vertical potential temperature profile becomes neutral in sufficiently strong winds. The statistical corrections were made twice: once in the April 2001–March 2011 period, the other in the April 2016–March 2017 period. The results are summarized below:

1) During summer months (May–August), the ground-based mixed layer formed at night was at least 250 m deep. This result is consistent with previous numerical simulations of the Tokyo urban area. During winter months (November–February), the bottom height of the elevated inversion layer with strong atmospheric stability was approximately 200 m or more above 250 m. Moreover, the atmospheric stability in the surface layer and its upper layer were consistent with previous observational studies. The observed stabilities tended to be higher than the previously simulated values. In winter, the temporal variation of the vertical potential temperature profile (from the surface to 250 m above the Tokyo urban area) was well explained by the suppression (promotion) of vertical mixing, which increased (decreased) the bottom height of the elevated inversion layer. The depth of the nighttime mixed layer was 50 m higher in the 2000s than in the 1960s–1980s. The mixed layer depth was probably increased by urbanization, with increasingly high building structures. The estimated ratio of the mixed layer depth to the typical building height was 6–8, larger than in other cities.
2) Both of the vertical potential temperature gradient at the rural area and the difference of vertical potential temperature gradient between the rural area and the urban area have significant positive correlations with HII, as observed in previous studies. The vertical potential temperature gradient on the urban area also has a significant positive correlation with HII. In a heat budget analysis of

the air column moving from non-urban to urban areas via nocturnal land breezes, the heating rate of the air column was determined as 93 W m^{-2}. The downward sensible heat flux induced by vertical mixing was estimated to exceed the upward sensible flux from the urban surface, as reported in previous observational studies of small- or mid-scale cities. Previous studies have postulated neutral atmospheric stability over urban areas. However, the present study suggests that the stable layer over a non-urban area is preserved even when it penetrates the Tokyo metropolitan area.

3) Clear nighttime conditions with weak winds were categorized into HII formation and atmospheric stability. Northerly winds dominated during small-HII nights. In contrast, the wind directions on large-HII nights were unclear in the western part of the Tokyo Wards area. The HII and atmospheric stability on winter nights at Tokyo were interpreted in terms of the parameters derived from numerical simulations of HIC (Niino *et al.* 2006). These parameters admit a regime in which the HIC develops over the edge of the urban area that corresponds to the heat cliff.

4) The wavelike motions on three clear nights with weak winds were investigated in 1-min data of the Tokyo metropolitan area. The period of the wavelike motion (20–50 mins) was 5–10 times longer than the BVO period. This ratio agreed with a previous observational study by Yokoyama *et al.* (1981). The wavelike motions were presumed as GW generated by the convergence of two wind flows: the northerly wind passing through the urbanized areas such as Saitama, and the westerly cold current. The GW moved eastward from Fuchu-to-Nerima. The wind and temperature fluctuations were explained by vertical mixing between the upper neutral warmer layer and the surface stable cooler layer. When a heat cliff formed, the wavelike motion developed in the western part of the Tokyo Wards area, but was suppressed in the central urban area. The boundary of the wave-like motion developed or not was consistent with the heat cliff. The GW was considered to be dispersed around the central urban area because the atmospheric stability was near neutral there. The atmospheric stability probably changed between the Suginami and Shibuya Wards. The potential temperature fluctuations above 169 m at the TT increased with the arrival of the westerly wind. Their presence suggested a downward sensible heat flux from the elevated inversion layer to the surface layer. The wave-like motion infrequently occurs in the urban area. In this case, the atmosphere in the urban

area was stable, and no clear heat cliff developed.

Based on the flow regime derived by Niino *et al.* (2006), the HIC on winter nights in Tokyo primarily develops over the western part of the Tokyo Wards area, where the heat cliff is formed. The stable layer over non-urban areas is infrequently preserved even when it penetrates the Tokyo metropolitan area. The westerly wind is suggested to affect the nocturnal urban boundary layer and the horizontal temperature distribution. The stable layer on a non-urban area was sometimes preserved even if it penetrates to the Tokyo metropolitan area. Although this study focused on the heat cliff formed in the western part of the Tokyo Wards area, heat cliffs also develop in the eastern part of this area. The formation process of the eastern heat cliff remains a challenge for future research.

The elevated inversion layer probably formed above the observation height of the TT (250 m) in cluster C (Chapter III). In addition, the depth of the elevated layer remains undefined. These problems could be resolved by higher observations using a temperature profiler (e.g., Khaikine *et al.* 2006; Kadygrov *et al.* 2007; Melecio *et al.* 2018).

The regional characteristics of the wavelike motion were examined in case studies. Wavelike motions in both cases were considered to result from the convergence of two wind flows. However, as other phenomena can also generate wavelike motions, the formation process of these motions should be clarified in accumulated cases. Fujibe (2018) derived the climatological features of surface-air temperature variations in Japan from one-minute data collected by 917 AMeDAS. The horizontal interval of AMeDAS is approximately 17 km. One-minute meteorological APMS data in Tokyo have been recorded since the 2010s. The horizontal interval of APMS in this area is approximately 4.7 km. In future studies, these higher-resolution data will provide better insights into the climatological features of the wind and temperature fluctuations in the Tokyo urban area.

References

Aikawa, M. and Hiraki, T. 2009. Characteristic seasonal variation of vertical air temperature profile in urban areas of Japan. *Meteorology and Atmospheric Physics*, **104**: 95–102.

Bohnenstengel, S. I., Evans, S., Clark, P. A. and Belcher, S. E. 2011. Simulations of the London urban heat island. *Quarterly Journal of the Royal Meteorological Society*, **137**: 1625–1640.

Bornstein, R. D. 1968. Observations of the urban heat island effect in New York City. *Journal of Applied Meteorology*, **7**: 575–582.

Christen, A. and Vogt, R 2004. Energy and radiation balance of a central European city. *International Journal of Climatology*, **24**: 1395–1421.

Fujibe, F. 2018. Climatological features of sub-hourly temperature variations in Japan. *Journal of the Meteorological Society of Japan*, **96**: 147–160.

Fujibe, F. and Asai, T. 1979. A study of local winds in Kanto district. Part I: Structures of wind systems with diurnal variation. *Tenki*, **26**: 595–604.*

Godowitch, J.M., Ching, J.K.S. and Clarke, J.F. 1985. Evolution of the nocturnal inversion layer at an urban and nonurban location, *Journal of climate and applied meteorology*, **24**: 791-804.

Holton, J. R. 2004. *An introduction to dynamic meteorology fourth edition*. Academic press, San Diego.

Japan Meteorological Agency 2005. *Urban Heat Island Monitoring Report, 2003*.*

Japan Meteorological Agency 2013. *Urban Heat Island Monitoring Report, 2012*.*

Kadygrov, E. N., Koldaev, A. V., Miller, E. A., Sokolov, V. V and Khaikin, M. N. 2007. Study of urban heat island inhomogeneity in Nizhni Novgorod on the basis of a mobile atmospheric temperature profiler. *Russian Meteorology and Hydrology*, **32**: 110–118.

Kawamura, T. 1977. *Toshikikou no bunpu no jittai (Characteristics of urban climate distribution). Meteorological Research Note*, **133**: 26-47.*

Khaikine, M. N., Kuznetsova, I. N., Kadygrov, E. N. and Miller, E. A. 2006. Investigation of temporal-spatial parameters of an urban heat island on the basis of passive microwave remote sensing. *Theoretical and Applied Climatology*, **84**: 161–169.

Kikuchi, R. 1993. Sudden change of surface inversion of air temperature on suburban area in the Chiba Prefecture. *Quarterly Journal of Geography*, **45**: 1–12.**

Kimura, R. 1975. Dynamics of steady convections over heat and cool islands. *Journal of the Meteorological Society of Japan*, **9**: 191-200.

Kondo, H. 2001. *Ningenkuukan no kisyougakku (Climatology of human environment)*, Asakura Publishing, Tokyo.*

Kono, H., Watanabe, S. and Iwai, Y. 2010. Observation of the vertical temperature profile for one year using a tower for estimating the atmospheric stability in the urban boundary layer. *Tenki*, **57**: 589–600.*

Kusaka, H. and Kimura, F. 2004. Thermal effects of urban canyon structure on the nocturnal heat island: Numerical experiment using a mesoscale model coupled with an urban canopy model. *Journal of Applied Meteorology*, **43**: 1899–1910.

Kusunoki, K., Hisaki, E. and Akaeda, K. 2000. A case study of low-level internal gravity waves using Doppler radar and ACARS. *Journal of the Meteorological Society of Japan*, **78**, 511–525.

Kuttler, W., Miethke, A., Dütemeyer, D. and Barlag, A.-B. 2015. *The climate of Essen*, Webstarp Verlagsservicegesellschaft mbH.

Lyulyukin, V. S., Kallistratova, M. A., Kouznetsov, R. D., Kuznetsov, D. D., Chunchuzov, I. P. and Chirokova, G. Yu. 2015. Internal gravity-shear waves in the atmospheric boundary layer from acoustic remote sensing data. *Izvestiya, Atmospheric and Oceanic Physics*, **51**: 193–202.

Martilli, A. 2002. Numerical study of urban impact on boundary layer structure: Sensitivity to wind speed, urban morphology, and rural soil moisture. *Journal of Applied Meteorology*, **41**: 1247–1266.

Martilli, A., Clappier, A. and Rotach, M. W. 2002. An urban surface exchange parameterization for mesoscale models. *Boundary-Layer Meteorology*, **104**: 261–304.

Melecio, D., Ramamurthy, P., Arend, M. and González, J. E. 2018. Thermal structure of a coastal-urban boundary layer. *Boundary-Layer Meteorology*, *(Published online)*. https://doi.org/10.1007/s10546-018-0361-7

Mori, A. and Niino, H. 2002. Time evolution of nonlinear horizontal convection: Its flow regimes and

self-similar solutions. *Journal of the Atmospheric Sciences*, **59**: 1841–1856.

Nakagawa, K. 2011. Trends in studies on the formation mechanism of the urban heat island in Japan with special emphasis on the relationships between heat island intensity and boundary layer of urban areas. *Journal of Geography (Chigaku Zasshi)*, **120**: 255–284.**

Niino, H., Mori, A., Satomura, T. and Akiba, S. 2006. Flow regimes of nonlinear heat island circulation. *Journal of the Atmospheric Sciences*, **63**: 1538–1547.

Oda, R., Iwai, H., Ishii, S., Sekizawa, S., Mizutani, K. and Murayama, Y. 2011. Structure of turbulence in the urban atmospheric boundary layer detected in the Doppler lidar observation. *Journal of Japan Society of Civil Engineers Ser. B1 Hydraulic Engineering*, **67**: 313–318.**

Ohara, T., Uno, I. and Wakamatsu, S. 1989. Observed structure of a land breeze head in the Tokyo Metropolitan area. *Journal of Applied Meteorology*, **28**: 693–704.

Ohta, Y. 1966. Studies on the meteorological analysis of air pollution. *Journal of Meteorological Research*, **17**: 661–726.*

Ohya, Y., Nakamura, R. and Uchida, T. 2008. Intermittent bursting of turbulence in a stable boundary layer with low-level jet. *Boundary-Layer Meteorology*, **126**: 349–363.

Oke, T. R. 1982. The energetic basis of the urban heat island. *Quarterly Journal of the Royal Meteorological Society*, **108**: 1–24.

Oke, T. R. 1987. *Boundary layer climates second edition*, Cambridge University Press, UK.

Oke, T. R. and Maxwell, G. B. 1975. Urban heat island dynamics in Montreal and Vancouver. *Atmospheric Environment*, **9**: 191–200.

Oke, T. R., Mills, G., Christen, A. and Voogt, J. A. 2017. *Urban climate*, Cambridge University Press, UK.

Osawa, A. 2008. *Tatemonotakasa no rekishitekihensen Part1: Nihon niokeru tatemononotakasa to kousouka nituite (Histrical transition of building height. Part I: Buildings height and verticalization in Japan). The Journal of the Land Institute*, **16**: 15–28.*

Saito, N. 1977. Temperature and wind field in the atmospheric boundary layer on the southern Kanto plains. *Tenki*, **24**: 432–448.*

Saitoh, T. S., Shimada, T. and Hoshi, H. 1996. Modeling and simulation of the Tokyo urban heat island. *Atmospheric Environment*, **30**: 3431–3442.

Sakakibara, Y. 2001. Comparison between the effect of heating from urban surface and that of mechanical mixing of urban atmosphere to heat island. *Tenki*, **48**, 305–311.**

Sakakibara, Y. and Nakagawa, K. 2011. Vertical temperature profiles with light breezes at night in urban and rural areas of Obuse, Nagano. *Journal of Geography (Chigaku Zasshi)*, **120**: 392–402.**

Sparks, N. and Toumi, R. 2015. Numerical simulations of daytime temperature and humidity crossover effects in London. *Boundary-Layer Meteorology*, **154**: 101–117.

Sugawara, H., Aiso, H., Oda, R. and Seino, N. 2015. Comparison of daytime air heating amount between city and surrounding areas. *Journal of Heat Island Institute International*, **10**: 8–12.**

Sun, J., Mahrt, L., Nappo, C. and Lenschow, D. H. 2015. Wind and temperature oscillations generated by wave–turbulence interactions in the stably stratified boundary layer. *Journal of the Atmospheric Sciences*, **72**: 1484–1503.

Takahashi, H. 1998. Climatological feature of diurnal variation in wind systems and divergence field over Kanto district under stable synoptic conditions – In the cases of summertime land-sea brazers and strong winter monsoon–. *New Geography*, **45**: 34–53.**

Takahashi, H., Shimizu, S., Yamato, H., Seto, Y. and Yokoyama, H. 2014. Wintertime nocturnal temperature distribution based on spatially high density observation data in the Tokyo Metropolitan area under clear sky and weak wind conditions. *Journal of Geography (Chigaku Zasshi)*, **123**: 189–210.**

Tamiya, H. and Ohyama, H. 1981. Nocturnal heat island of small town, its manifestation and mechanism. *Geographical Review of Japan*, **54**: 1–21.**

Tokyo Metropolitan Government 1966. *Tokyo to taikiosentyousa no gaiyou, 1964 (Air Pollution Monitoring Report in Tokyo, 1964).**

Tokyo Metropolitan Government 2008. *Taiki osen jouji sokuteikyoku kekka houkoku (Observational Report of Air Pollution, 2007).**

Uno, I., Wakamatsu, S., Ueda, H. and Nakamura, A. 1988. An observational study of the structure of the

nocturnal urban boundary layer. *Boundary-Layer Meteorology*, **45**: 59–82.

Uno, I., Ueda, H. and Wakamatsu, S. 1989. Numerical modeling of the nocturnal urban boundary layer. *Boundary-Layer Meteorology*, **49**: 77–98.

Uno, I., Wakamatsu, S. and Ueda, H. 1992. Observed structure of the nocturnal urban boundary layer and its evolution into a convective mixed layer. *Atmospheric Environment. Part B. Urban Atmosphere*, **26**: 45–57.

Viana, S., Yagüe, C. and Maqueda, G. 2009. Propagation and effects of a mesoscale gravity wave over a weakly-stratified nocturnal boundary layer during the SABLES2006 field campaign. *Boundary-Layer Meteorology*, **133**: 165–188.

Yamashita, S. 1990. The urban climate of Tokyo. *Geographical Review of Japan*, **63B**: 98–107.

Yamashita, S. 1996. Detailed structure of heat island phenomena from moving observations from electric tram-cars in metropolitan Tokyo. *Atmospheric Environment*, **30**: 429-435.

Yamazaki, H., Sofuku, M., Nagata, T. and Nakano, K. 1971. *Kytoon niyoru toshinbu no kisyoukansoku nituite (Meteorological observation in urban area using kytoon). Annual Report of the Tokyo Metropolitan Research Institute for Environmental Protection*, **2**: 34–38.*

Yamazoe, Y. and Ichinose, T. 1994. An analysis of urban heat islands in Tokyo and its environs: The comparison of cloudless nights with cloudy nights in autumn. *Geographical Review of Japan*, **67A**: 551–560.**

Yokoyama, O. 1980. An exploration of the atmospheric boundary layer. *Tenki*, **27**: 5–12.*

Yokoyama, O., Hayashi, M., Kitabayashi, K., Simokata, S., Gamo, M., Yamamoto, S., Yoshikado, H. and Sugawara, K. 1974. *Taikikyoukaisoutyuu no ondo to huukouhuusoku no entyokubunpu Part1: Toshiiki deno settigyakutensou no seiseisyoumetsu (The vertical profile of temperature, wind direction and wind speed in boundary layer Part1: Generation/extinction of ground-based inversion layer in urban layer). Pollution Control (Kogai)*, **9**: 86–97.*

Yokoyama, O., Mizuno, T. and Yamamoto, S. 1981. Observational study of turbulence and wave motion in the nocturnal surface inversion layer. *Pollution Control (Kogai)*, **16**: 67–76.**

Yokoyama, O., Hayashi, M., Mizuno, T. and Yamamoto, S. 1983. *Seiyaanteisou no ranryuukouzou*

(Structure of turbulence in nocturnal stable layer). Pollution Control (Kogai), **18**: 1–8.*

Yokoyama, O., Mizuno, T., Yamamoto, S., Hayashi, M, and Suzuki, M. 1984. An analysis of turbulence and wave-like motion appearing in the surface stable layer. *Pollution Control (Kogai)*, **19**: 303–312.**

Yoshikado, H., Nakajima, K., Kawamoto, Y. and Ooka, R. 2014. Heat budget of sea breezes passing through urbanized areas of Tokyo. *Tenki*, **61**: 541–548.**

Yu, M., Liu, Y., Dai, Y. and Yang, A. 2013. Impact of urbanization on boundary layer structure in Beijing. *Climatic Change*, **120**: 123–136.

(*: in Japanese, **: in Japanese with English abstract)

要旨

論文題目：

東京における夜間都市境界層の特徴とその地上気温分布および風系との関係

氏名：中島 虹

都市ヒートアイランド現象 (UHI) は，都市の気温がその周囲の気温と比べて高くなる現象であり，都心と郊外との気温差 (ヒートアイランド強度，HII) は一般に冬季夜間に大きくなる．UHI の発現には，人工排熱や地表面の熱・放射収支の変化とともに，下層大気の鉛直混合に伴う境界層の変形が関与しており，都市では郊外と異なり夜間でも逆転層は接地しにくく，地上付近は中立に近いとされる．広域的な都市の熱環境の解明には，地上の面的な気温分布とともに都市境界層の鉛直構造を把握し，都市大気を立体的に理解する必要がある．しかしながら東京を対象とした都市境界層の調査は，短期間の観測があるものの，夜間を対象とした長期的・系統的な研究は乏しく，鉛直気温分布の現れ方や水平気温分布との関係など未解明の課題が多い．

本研究は，夜間の都心における境界層の特徴を提示した上で，特に冬季夜間の地上気温分布や風系との関係から，東京の都市大気の多様性・変動性の解明を目的とする．解析に用いたデータは，東京タワー (TT) の気温観測値 (2001–2010 年度 (5 高度) と 2016 年度冬季 (6 高度)) や郊外のスカイタワー西東京 (ST) で独自に観測した気温 (6 高度，2016 年度冬季) および大気汚染常時監視測定局 (常監局) など多数地点の気象観測値である．

本論文は全 7 章で構成されている．以下に概要を示す．

第 1 章では，UHI や境界層に関する既往研究をレビューし，東京を対象とした本研究の背景や目的と論文構成を述べた．

第 2 章では，東京都心部の地表面粗度を構成する建築物群の概要や使用データを述べるとともに，TT における気温観測値の妥当性を検討した．大気下層で十分な鉛直混合が期待される夜間強風時を抽出し，鉛直方向の温位の一様性を検討した結果，特定高度の温位が系統的に高いことが判明したため，これを器差とみなし，回帰式を用いた補正を施した．

第 3 章では，2001–2010 年度のデータを用いて都心 (TT) における温位鉛直分布の特徴を統計的に

提示した．晴天弱風夜間における毎時刻の温位傾度 ($\partial\theta/\partial z$) の鉛直分布にクラスター分析を施し，5類型に分類した．冬季 (11〜2 月) には，地上付近から 250 m まで安定 ($\partial\theta/\partial z$ ∼1℃/100m) あるいは 200 m より上空で強い安定 ($\partial\theta/\partial z$ ∼3℃/100m) を示す場合が夜半前から増加し日の出前にはそれぞれ 27% と 17% を占めるが，夏季 (5∼8 月) にはまったく現れない．後者の強い安定層は都市上空の安定層の底面とみなされ，冬季夜間の混合層高度は 200 m かそれ以上であり，1960 年代の観測結果と比べて 50 m 程度高く，都市化による混合層高度の上昇が示唆された．数値モデルによる既往研究の都市大気再現結果と比較して，観測に基づく本研究で示された接地層や上空の安定層の温位傾度は大きく，従来考えられてきたよりも冬季夜間の東京都心における大気下層は安定であることが分かった．また，冬季の温位鉛直分布の時間変化には，鉛直混合の促進・抑制とともに，上空安定層底面の上昇・下降の関与が考えられた．

第 4 章では，夜間に内陸から東京都心に向かう陸風に沿った郊外 (ST) と都心 (TT) における気温鉛直観測値により，風向に沿う地上気温の上昇 (HII) と安定度との関係を解析した．既往研究と同様に，郊外における鉛直温位傾度や，郊外と都心との鉛直温位傾度差は，HII と有意な正相関を示し，大気下層の気温鉛直分布の変化が HII と密接に関わることが確認された．次に陸風によって気柱が郊外から都心に移流したと仮定し，気柱の加熱率と熱収支を推算した結果，中小都市を対象とした既往研究と同様に，東京の HII には地表面からの顕熱よりも，鉛直混合に伴う境界層上部からの顕熱輸送 (逆転層の破壊) の寄与の大きいことが示唆された．なお，都心における鉛直温位傾度も，HII や郊外の鉛直温位傾度と有意な正相関を示す．すなわち都心においても陸風の強い安定層は十分に破壊されず，そのため都心域においても安定層が現れる (第 3 章) と考えられた．

第 5 章では，雲量や風速の条件が同一であっても HII に差異が現れることに着目し，常監局の 1 分値を用いて地上の気温分布および風系の特徴を提示した．HII が小さい場合には，都区部内外で北寄りの風が夜間を通して卓越する．一方で HII が大きい場合には，多摩地域から都区部西部にかけて，ブラント・ヴァイサラ振動の 5∼10 倍 (20∼50 分) の周期を持つ風向変動と気温変動が認められた．また，本研究で得られた気温分布や安定度，都市のスケール等のパラメータを，ヒートアイランド循環 (HIC) の数値モデル (Niino *et al.* 2006) にあてはめたところ，東京の冬季夜間の HIC は高温な都市域と低温な非都市域との境界 (気温急変域に相当) において発達するレジームに該当した．

第 6 章では，以上の解析をふまえ，大気下層の安定度と風・気温の変動性および都区部西部の気温

急変域との関係について解析と考察を行った．上述の風向変動は北寄りの風と西寄りの風が収束する際に，西寄りの風の強い安定層内に発生した重力波と考えられた．都区部西部の気温急変域が明瞭な場合，風向変動はその都心側で不明瞭となる．この時，都心の安定度は小さいことから，西寄りの風の強い安定層を東進した重力波が，都心では拡散されて風向変動が不明瞭となったと考えられた．一方で，都心域でも風向変動が認められる場合も少数あり，その場合には都心の安定度は大きく，都区部西部の気温急変域は不明瞭であった．すなわち，Niino *et al.* (2006) に従えば，基本的には HIC が都区部西部の気温急変域付近に局在し，都心への冷気の侵入が弱く気温急変域が明瞭となるが，安定層を伴う陸風が都心付近まで侵入する場合もあり，このような西寄りの陸風の挙動が東京の都市境界層構造や水平気温分布に影響を与えていると結論される．

第 7 章では，本論文で得られた結果をまとめ，今後の課題について述べた．

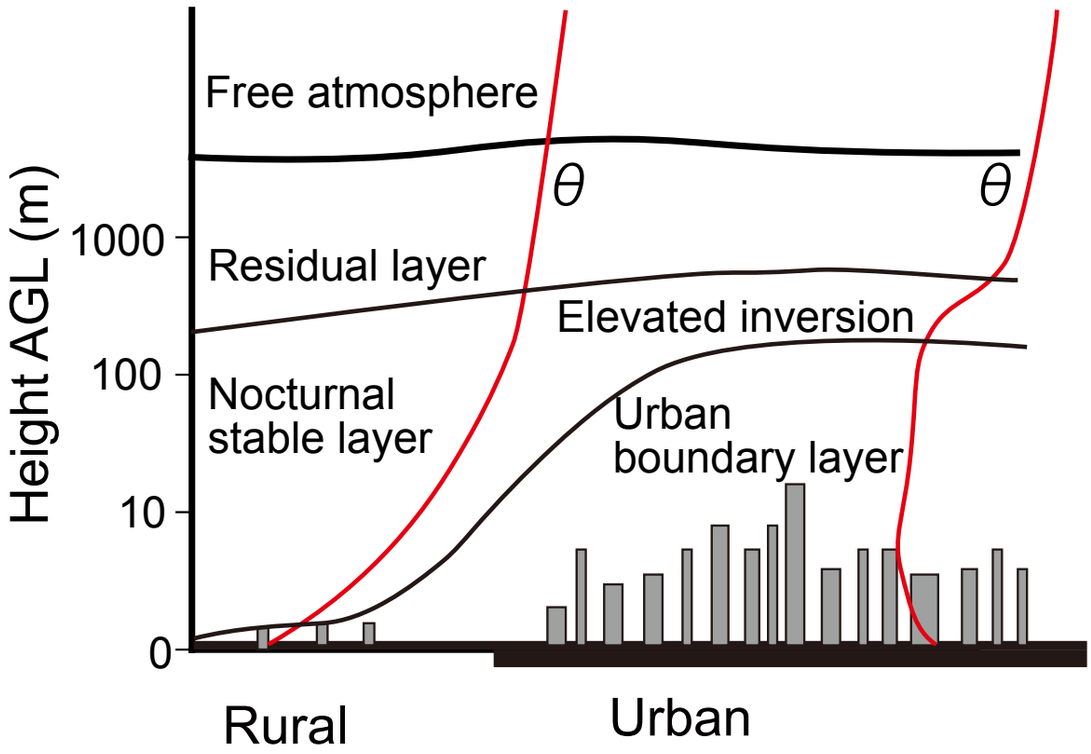

Figure 1: Schematic of the typical layering of the atmosphere over a city at night

The height scale is logarithmic, except near the surface. Red lines indicate vertical potential temperature (θ) profiles from surface. (after Oke *et al.* (2017))

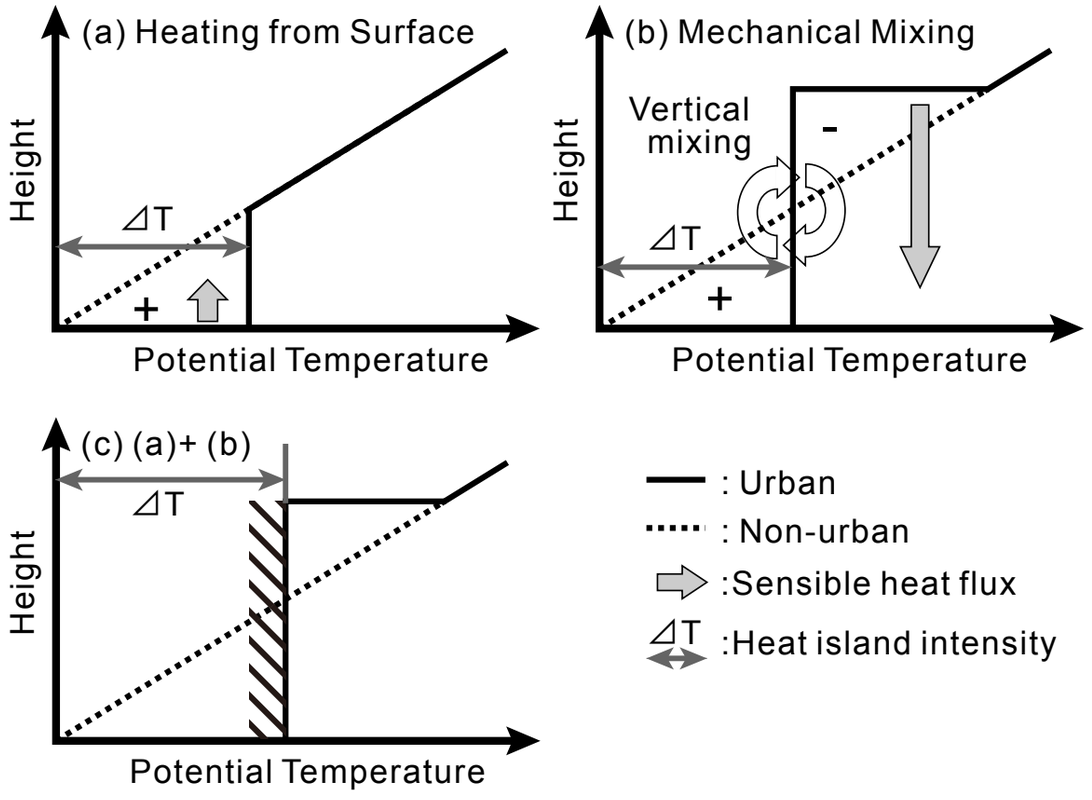

Figure 2: Schematic of the vertical potential temperature profiles over urban and non-urban areas in the cases of (a) heating from a surface, (b) mechanical mixing, and (c) both (a) and (b)

The $+$ $(-)$ symbols indicate that the potential temperature is higher (lower) in the urban area than the rural area.

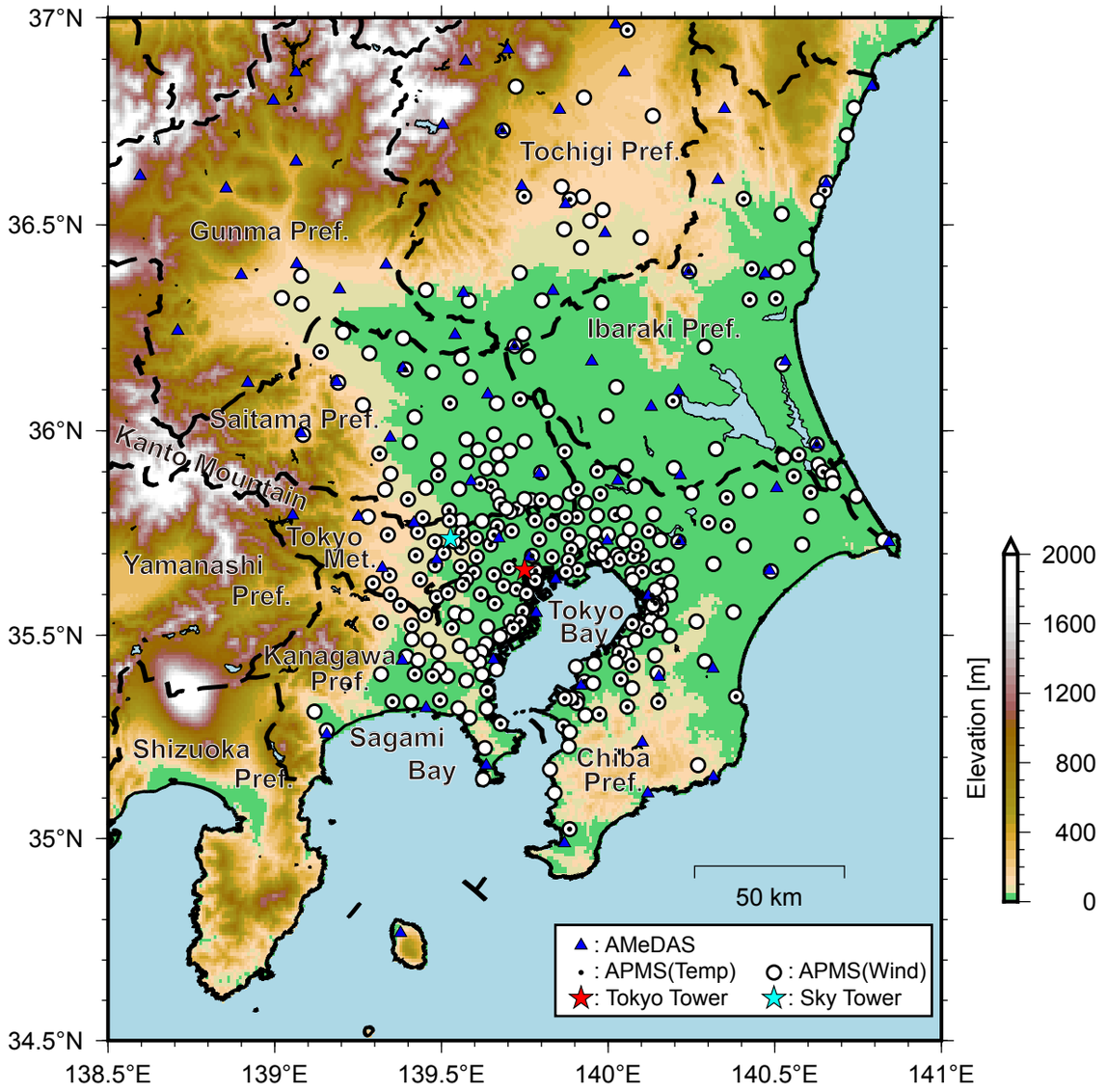

Figure 3: Map of the study area

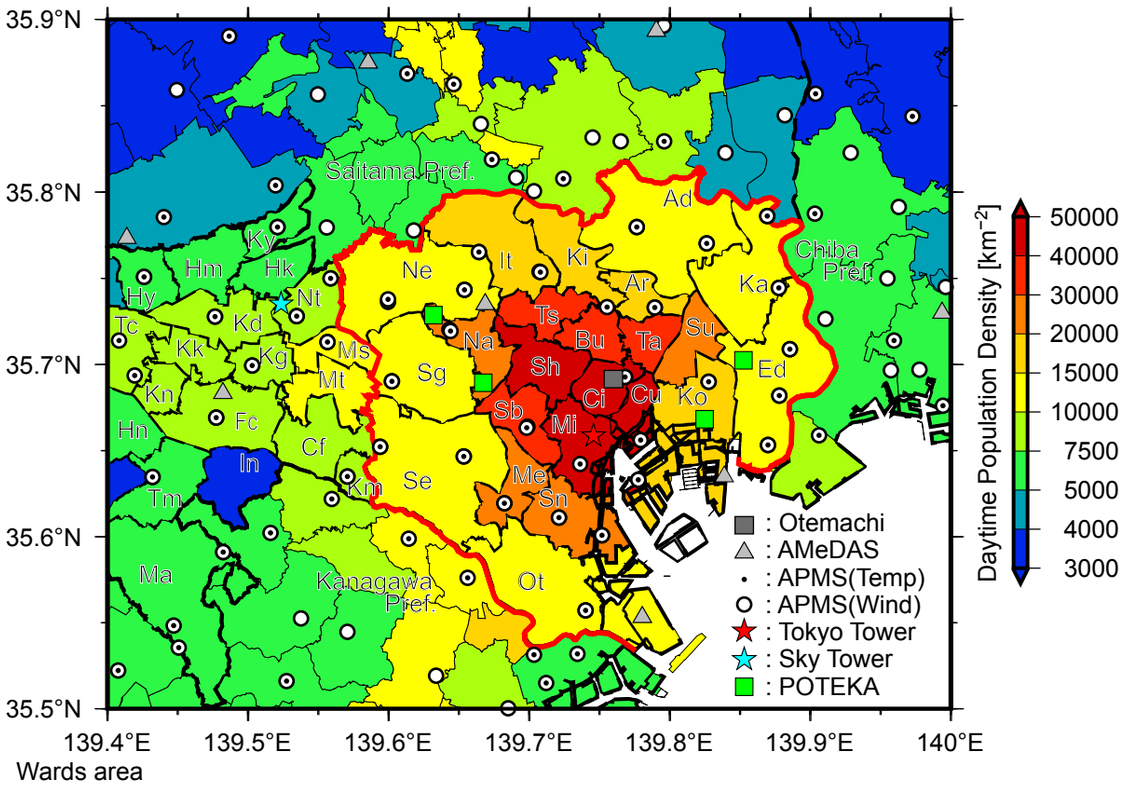

Wards area

Ad: Adachi	Ar: Arakawa	Bu: Bunkyo	Ci: Chiyoda	Cu: Chuo	Ed: Edogawa
It: Itabashi	Ka: Katsushika	Ki: Kita	Ko: Koto	Me: Meguro	Mi: Minato
Na: Nakano	Ne: Nerima	Ot: Ota	Sb: Shibuya	Se: Setagaya	Sn: Shinagawa
Sg: Suginami	Sh: Shinjuku	Su: Sumida	Ta: Taito	Ts: Toshima	

Municipalities

Cf: Chofu	Fc: Fuchu	Hn: Hino	Hk: Higashikurume	Hm: Higashimurayama
Hy: Higashiyamato		In: Inagi	Kk: Kokubunji	Kn: Kunitachi	Kd: Kodaira
Kg: Koganei	Kom: Komae	Ky: Kiyose	Ma: Machida	Mt: Mitaka	
Ms: Musashino	Nt:Nishitokyo	Tc: Tachikawa	Tm: Tama		

Figure 4: Distribution of daytime population density in the target area and the distribution of observatories

The red thick line indicates the boundary of the Tokyo Wards area.

Data are taken from the population census in 2015.

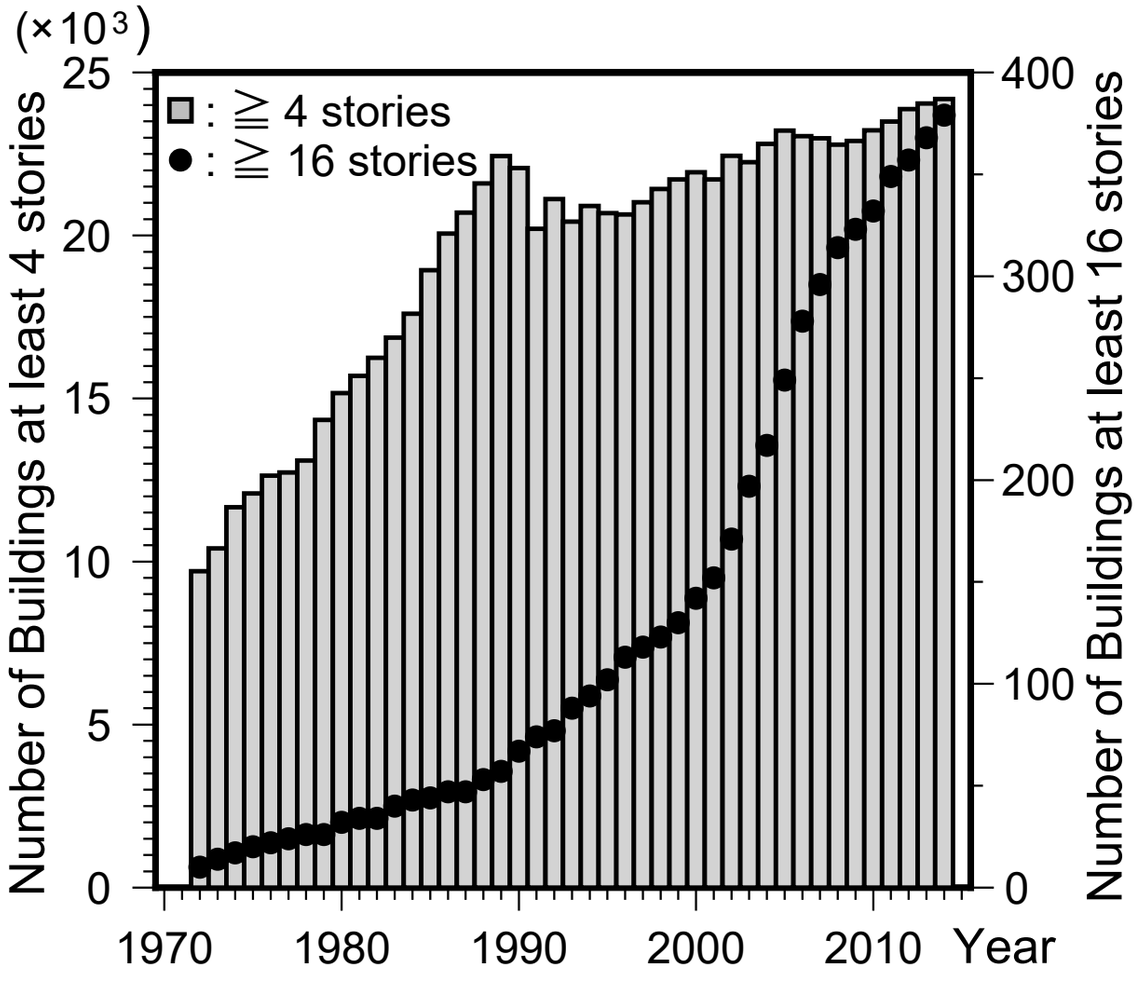

Figure 5: Historical changes in the number of buildings with at least 4 stories and at least 16 stories around Tokyo Tower in the Minato, Chuo, and Chiyoda wards

Data are taken from the statistics of the Tokyo Fire Department published annually from 1973 to 2015.

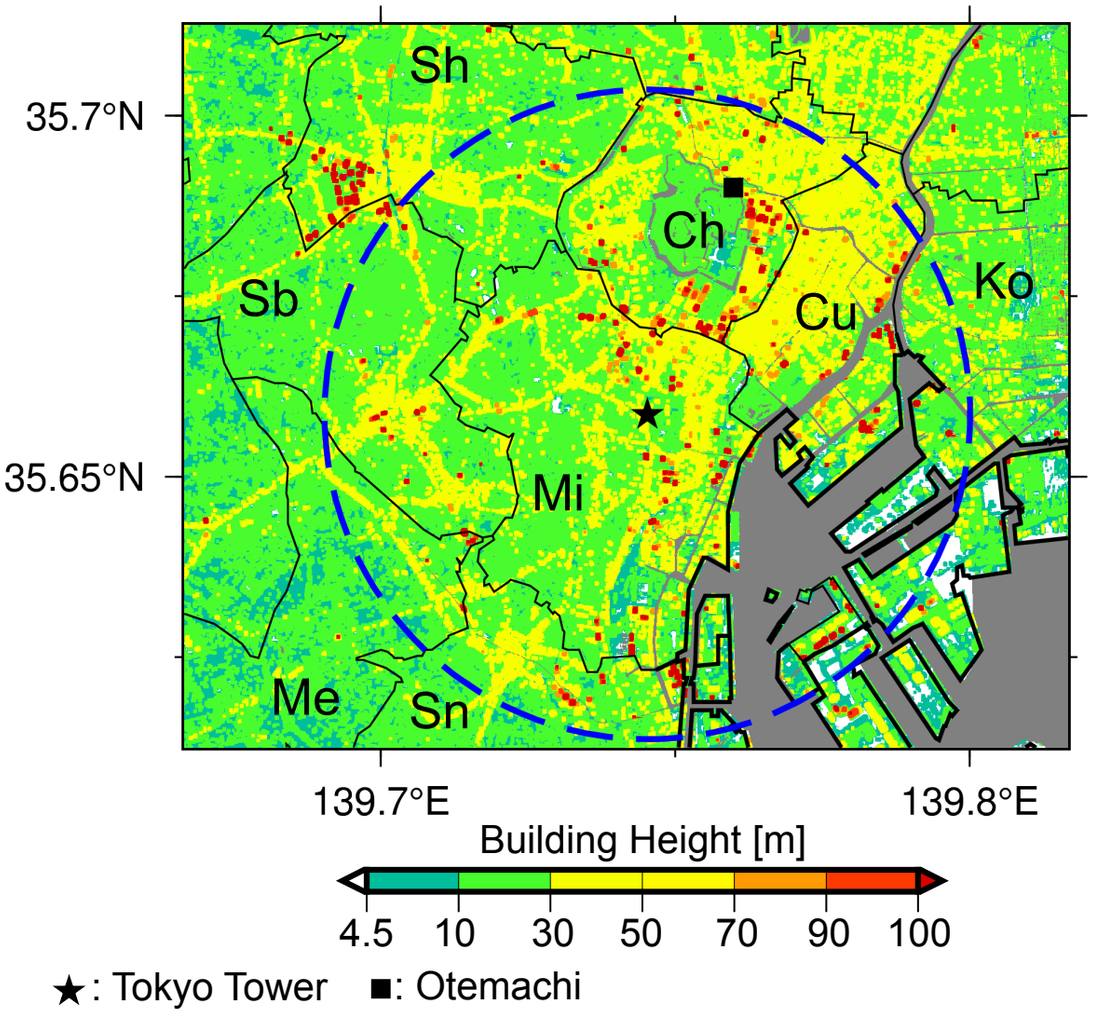

Figure 6: Distribution of building heights around TT, and the locations of TT and Tokyo District Meteorological Observatory (Otemachi)

Ch, Cu, Ko, Me, Mi, Sb, Sn, and Sh denote Chiyoda, Chuo, Koto, Meguro, Minato, Shibuya, Shinagawa, and Shinjuku Wards, respectively. The dashed blue line line encloses an area of 5 km radius from the TT.

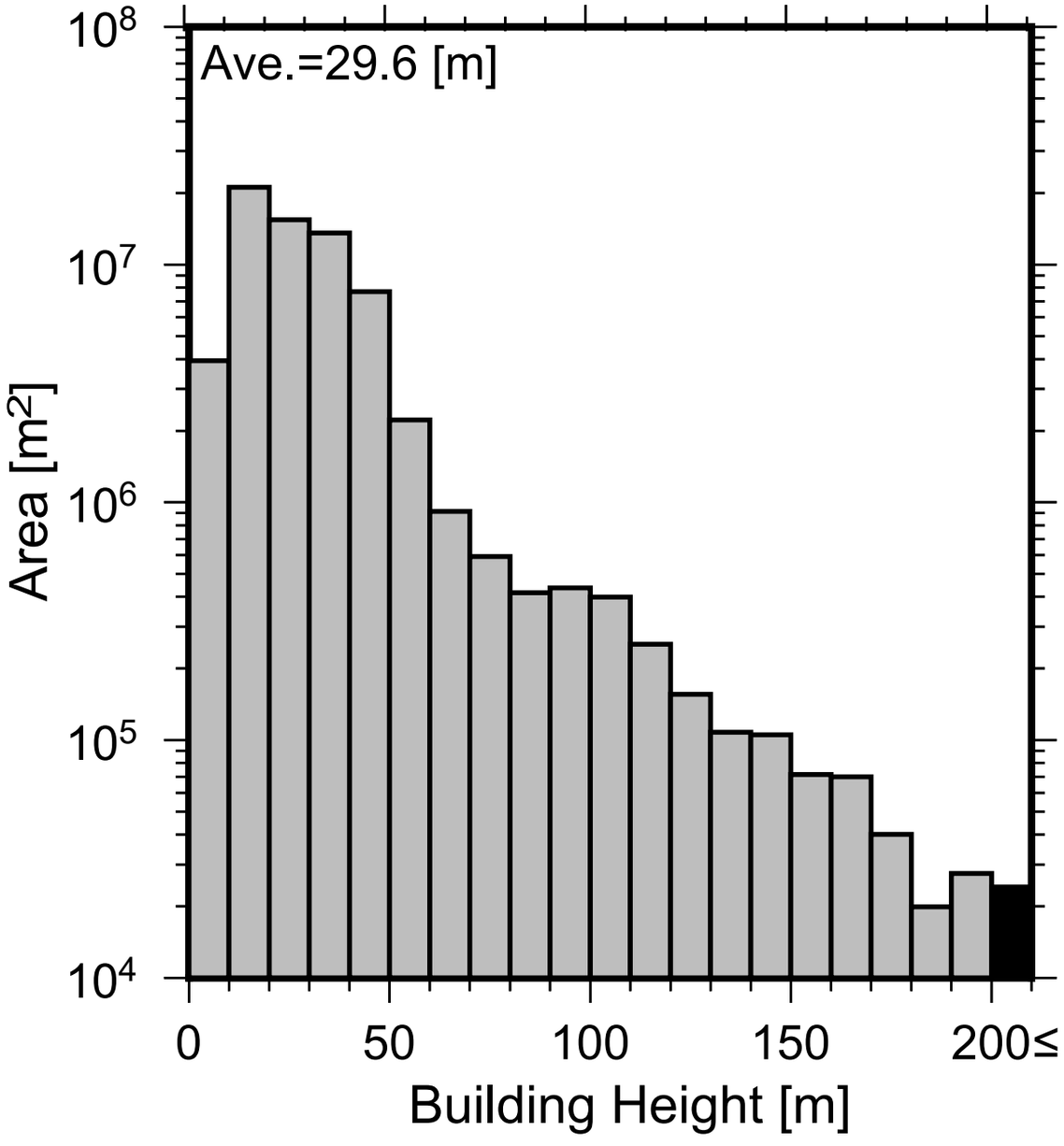

Figure 7: Area coverage of buildings within a 5-km radius from TT (circled area in Fig. 6)

The building heights are binned into 10-m intervals.

The total areas of buildings over 200 m are combined in the last bin.

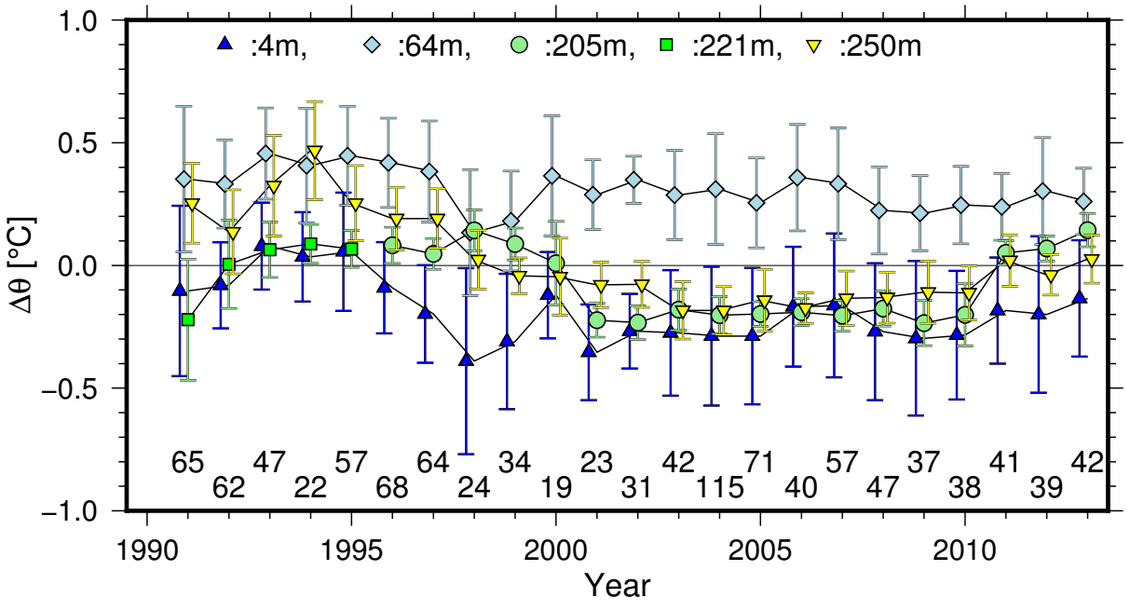

Figure 8: Inter-annual changes in potential temperature differences from that at 169 m, and the numbers of strong-wind hours

Error bars indicate standard deviations. The symbols are horizontally shifted to avoid overlap. $\Delta\theta$ indicates potential temperature difference from 169 m.

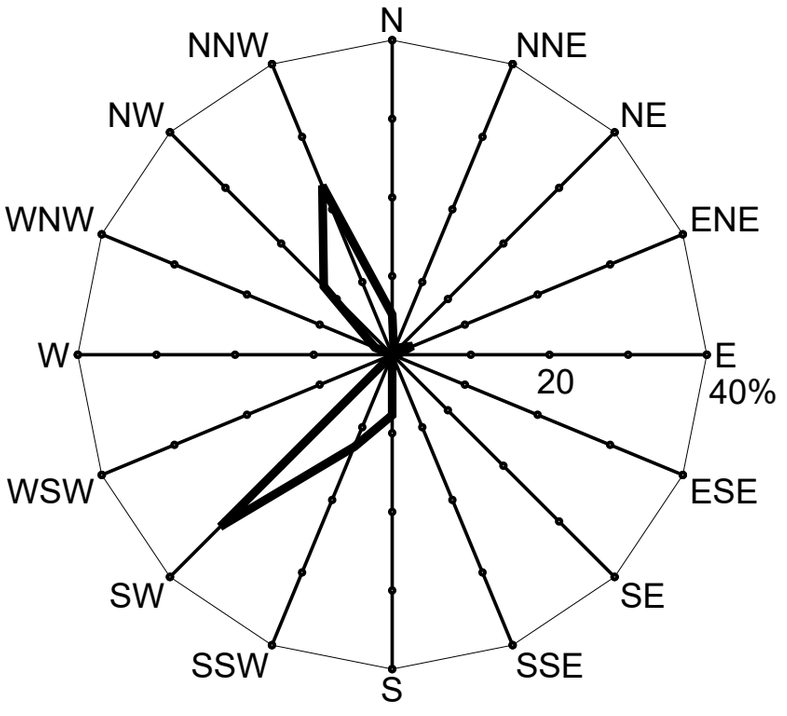

Figure 9: Wind rose at Otemachi in the case of strong winds in 2001–2010

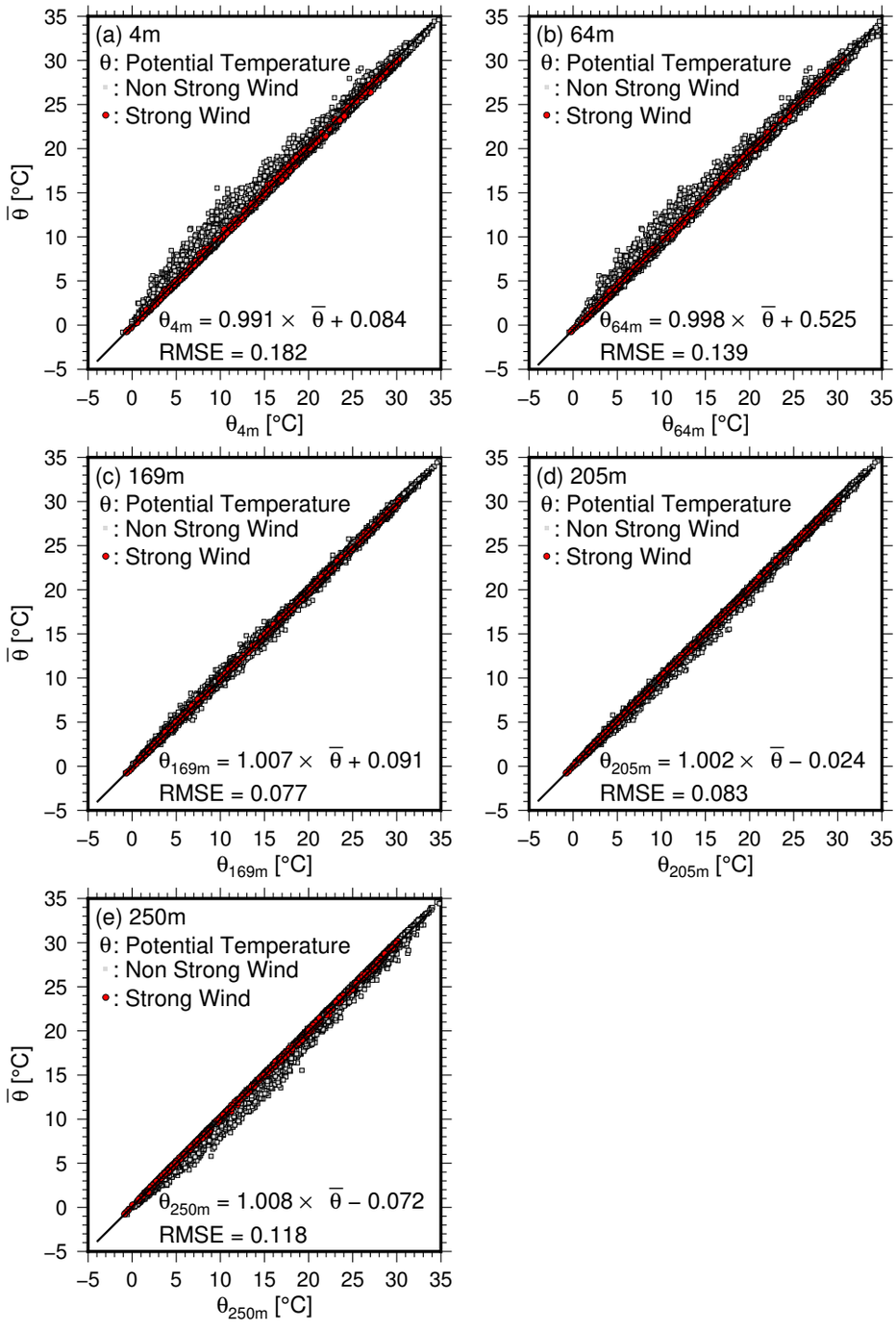

Figure 10: Relationships between potential temperature at each height and in average in cases of strong (red) and weak (grey) winds

$\bar{\theta}$: Average potential temperature averaged over 4 m, 205 m, and 250 m.

The formula, solid line, and RMSE in each panel are the regression formula, regression line, and root mean square error, respectively, in the strong-wind cases.

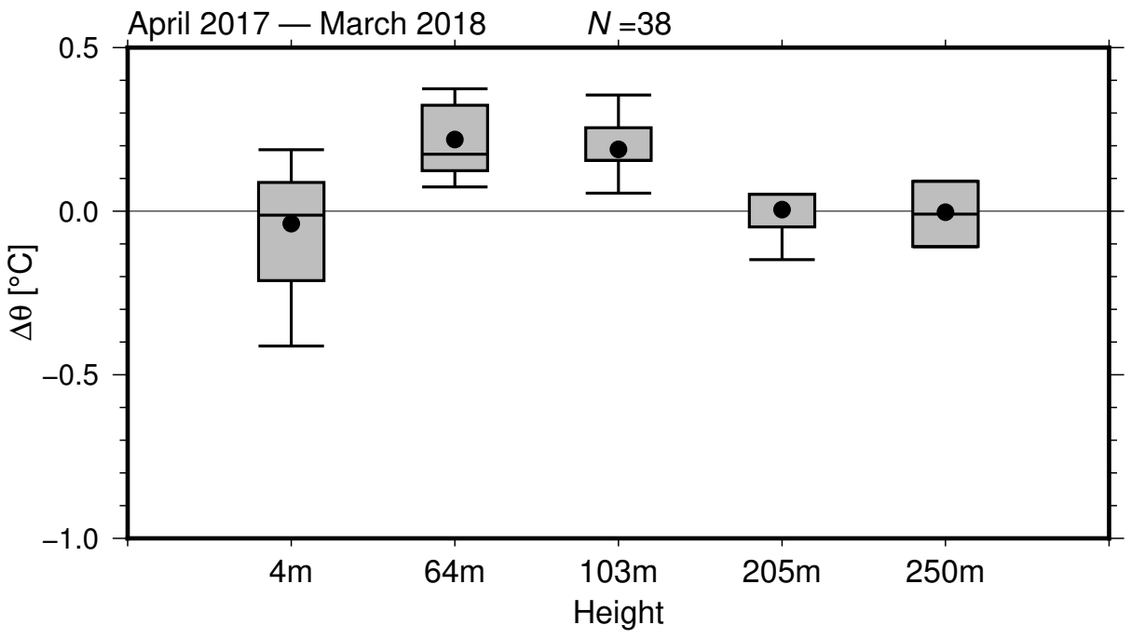

Figure 11: Potential temperature differences from that at 169 m and the number of strong wind hours

$\Delta\theta$ indicates potential temperature difference from 169 m.

N indicates the number of strong wind hours.

Black circle and boxplot indicate average, 10th, 25th, 50th, 75th and 90th percentiles.

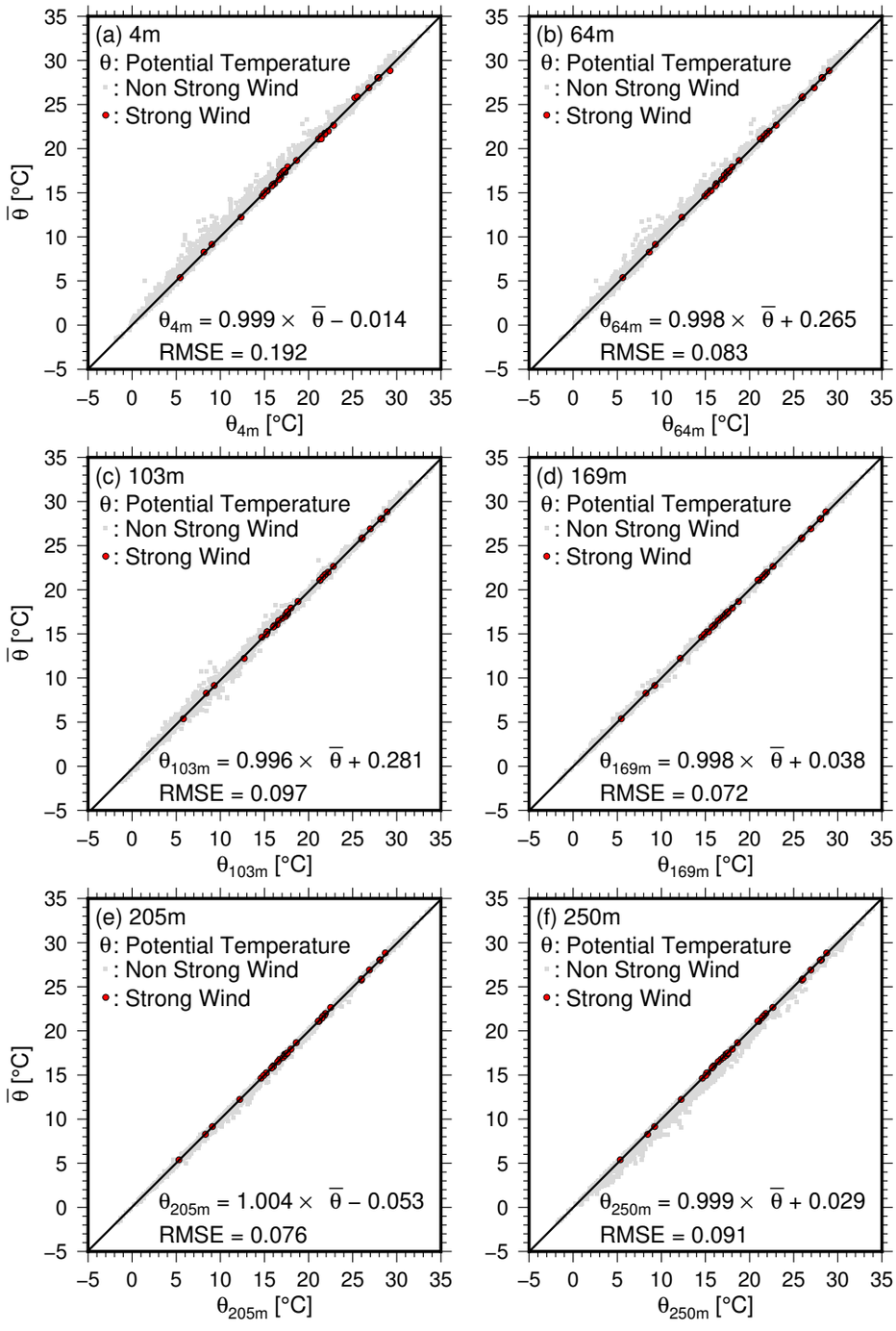

Figure 12: Relationships between potential temperature at each height in cases of strong (red) and weak (grey) winds

$\bar{\theta}$: Average potential temperature for 4 m, 169 m, 205 m, and 250 m.

The formula, solid line, and RMSE in each panel indicate regression formula, regression line, and root mean square error, respectively, in the strong-wind cases.

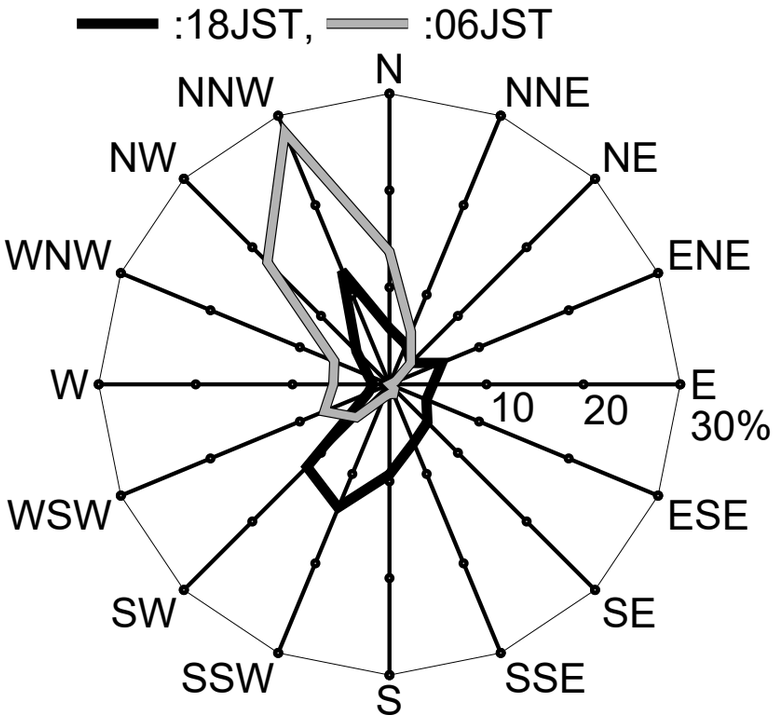

Figure 13: Wind rose at Otemachi at 18:00 JST (black) and 6:00 JST (gray) in clear nights with weak winds in 2001–2010

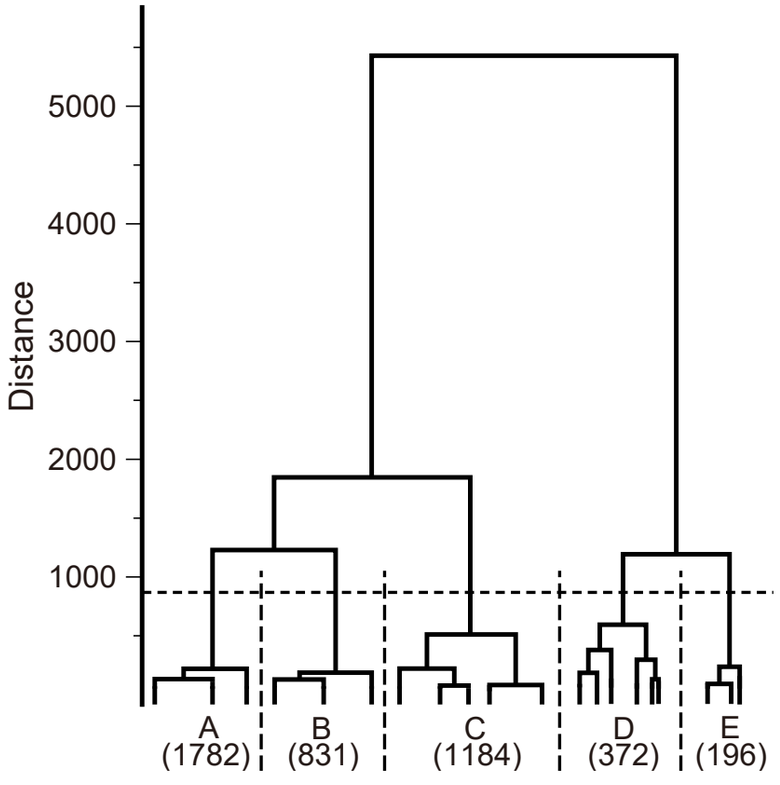

Figure 14: Cluster-analysis dendrogram for categorizing the vertical profiles of potential temperature

The bottom numerals state the number of hours in each cluster.

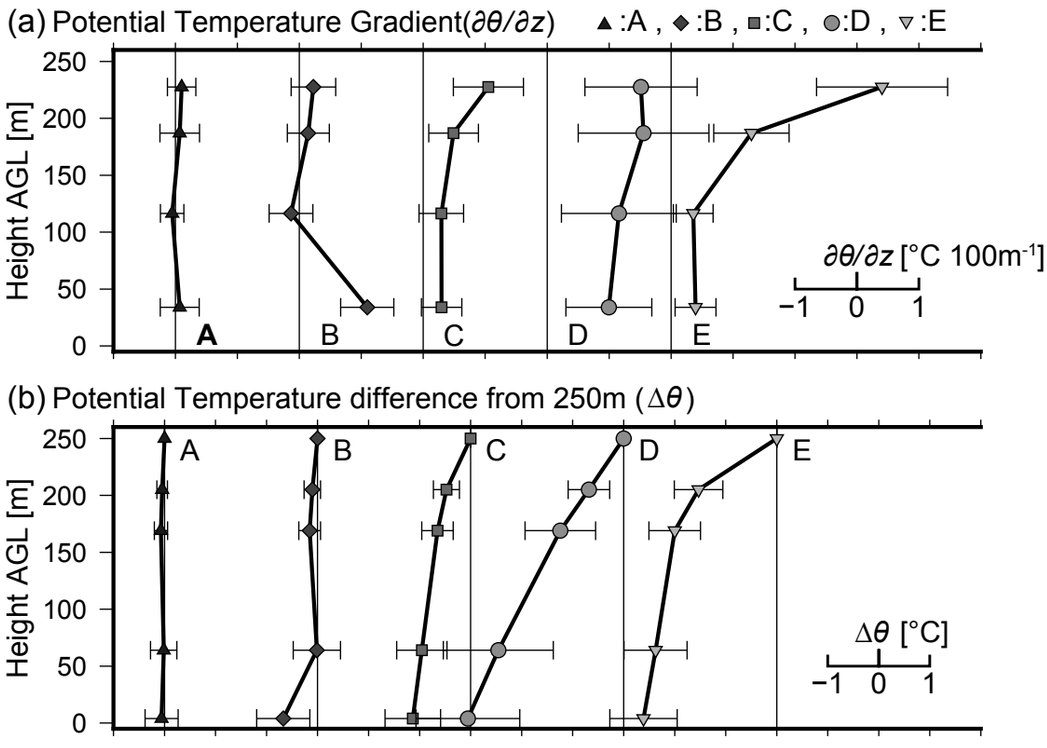

Figure 15: Vertical profiles of (a) potential temperature gradient and (b) difference of potential temperature from that at 250 m in each cluster

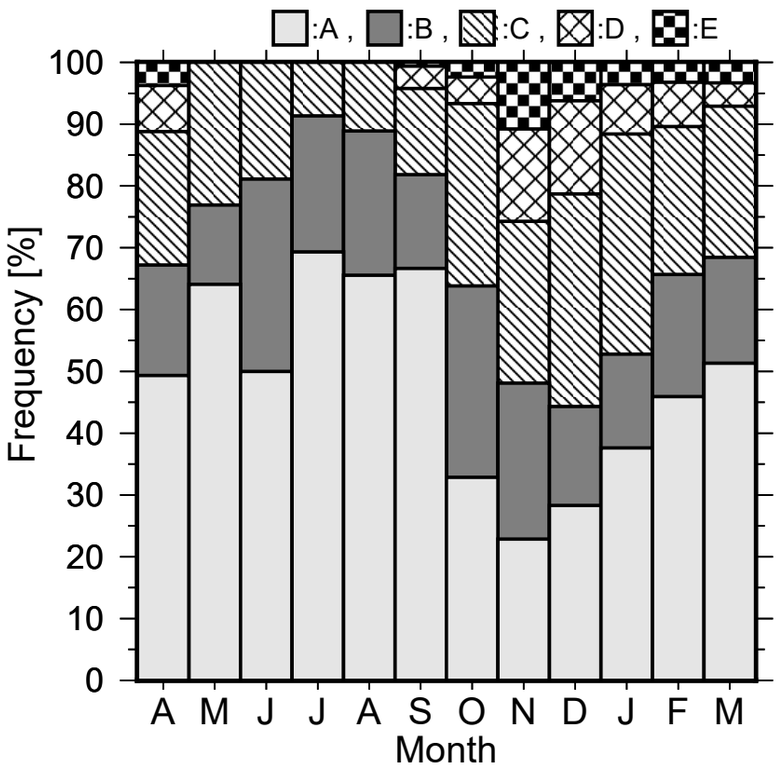

Figure 16: Monthly relative appearance frequencies (%) of the five clusters of vertical potential temperature profiles

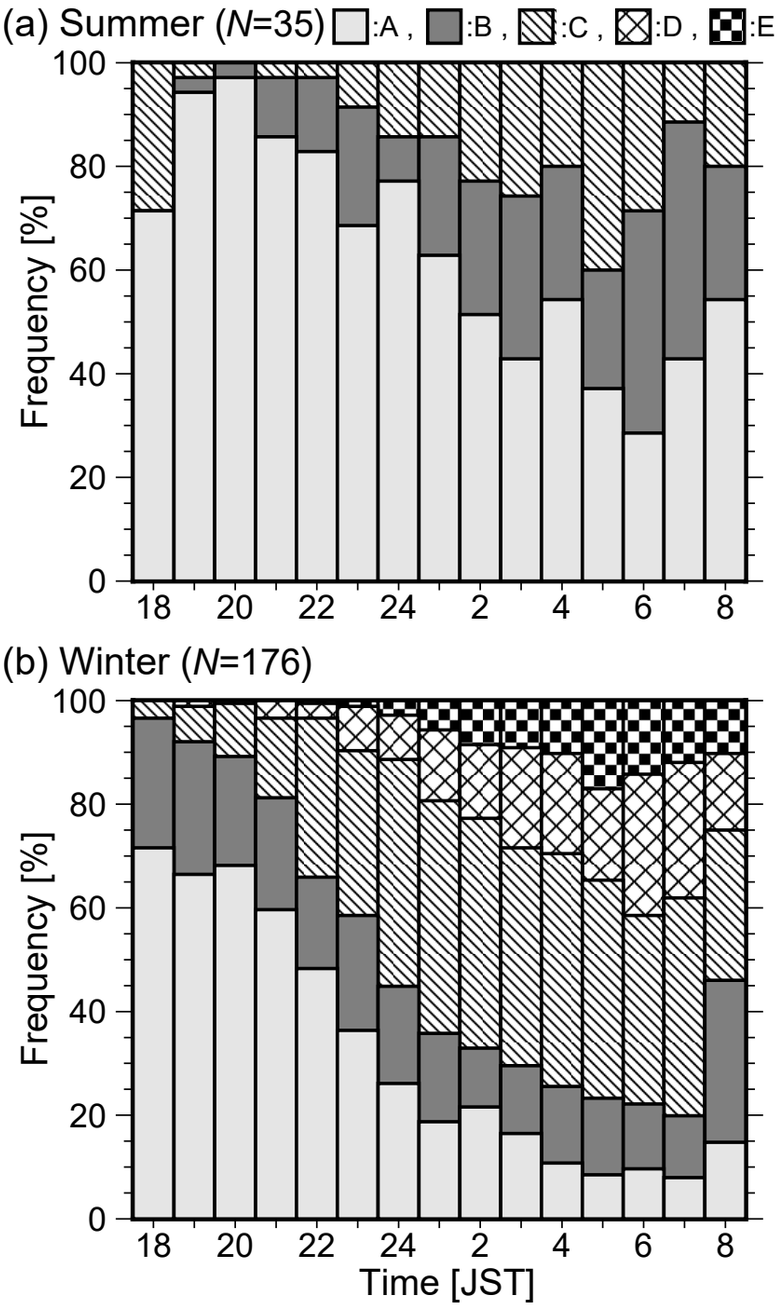

Figure 17: Nocturnal variations in the relative appearance frequencies of the five clusters of vertical potential temperature profiles in (a) summer and (b) winter

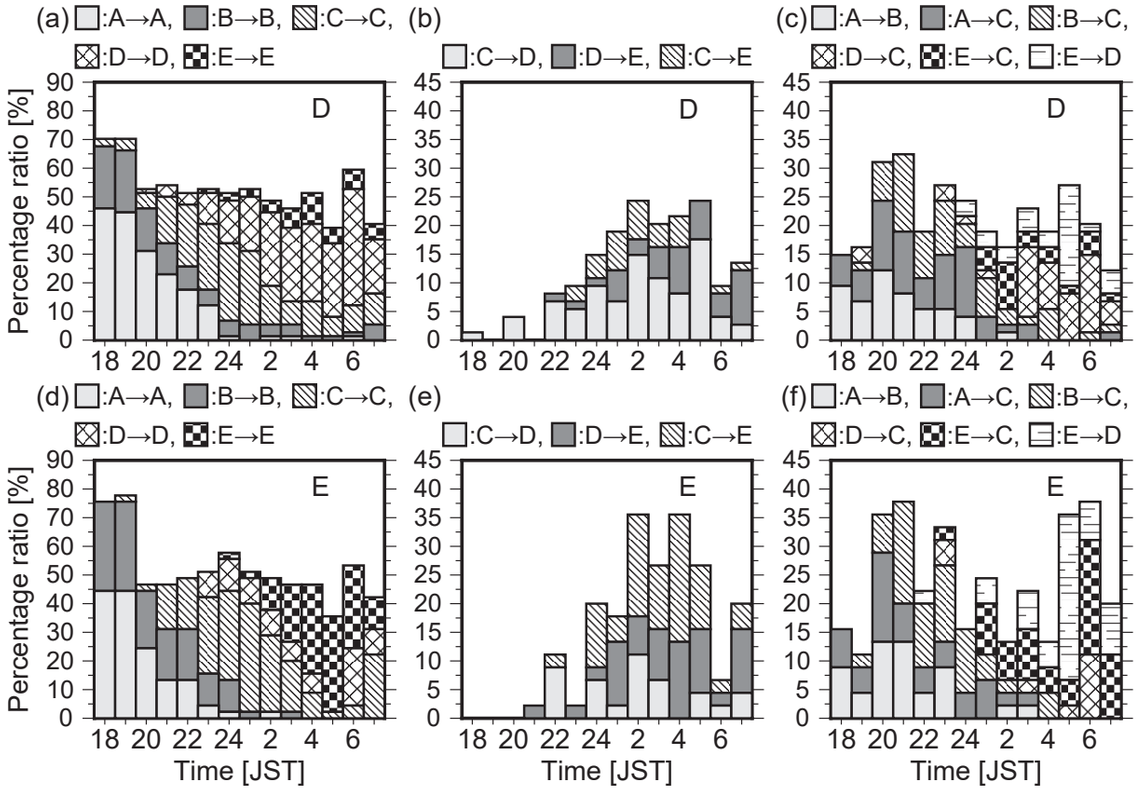

Figure 18: Nocturnal changes in the clusters of vertical potential temperature profiles

(a)–(c) On these nights, cluster D appeared between 03:00 and 06:00 JST.

(d)–(f) On these nights, cluster E appeared between 03:00 and 06:00 JST.

(a) , (d) No changes in the clusters.

(b) , (e) Cluster C changed to cluster D or cluster E, or cluster D changed to cluster C.

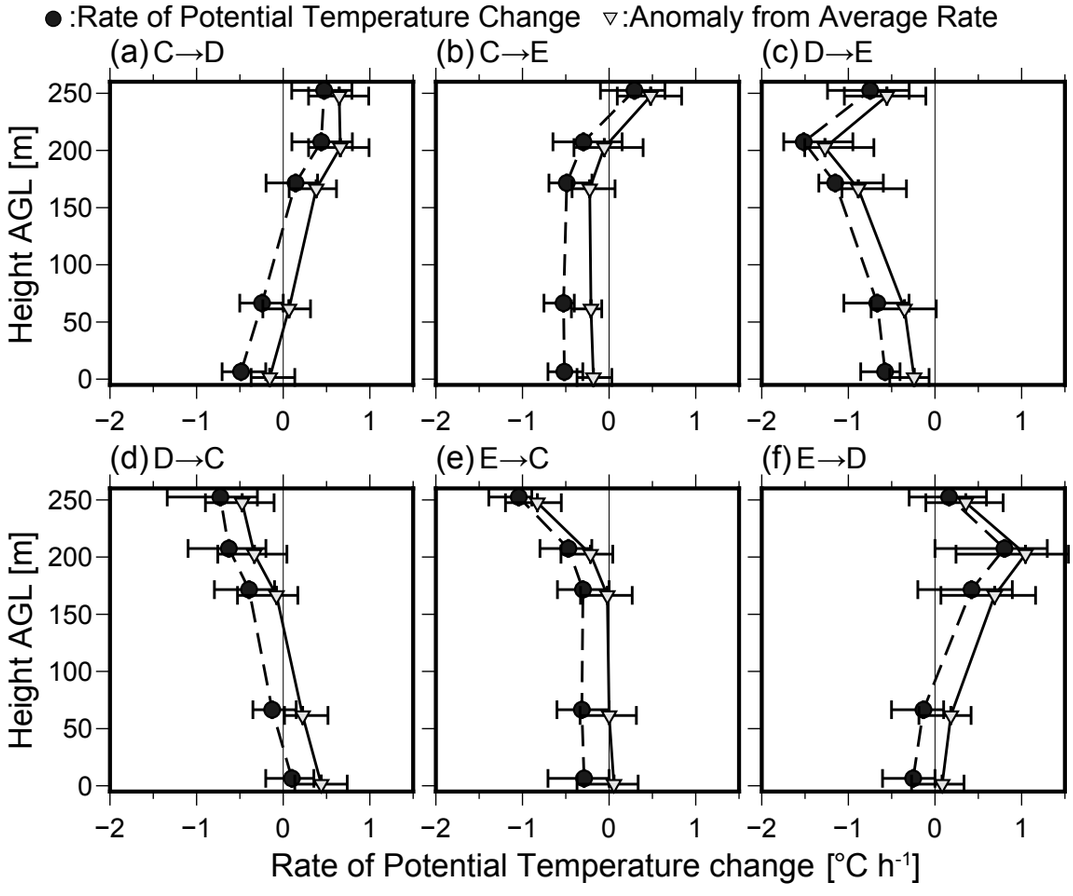

Figure 19: Rate of potential temperature change ($^\circ$C h^{-1}) during each cluster transition, and its anomaly from the average rate of potential temperature change during the 24:00–06:00 JST period

Error bars in each panel span the 25th to 75th percentiles. The symbols are vertically shifted to avoid overlap.

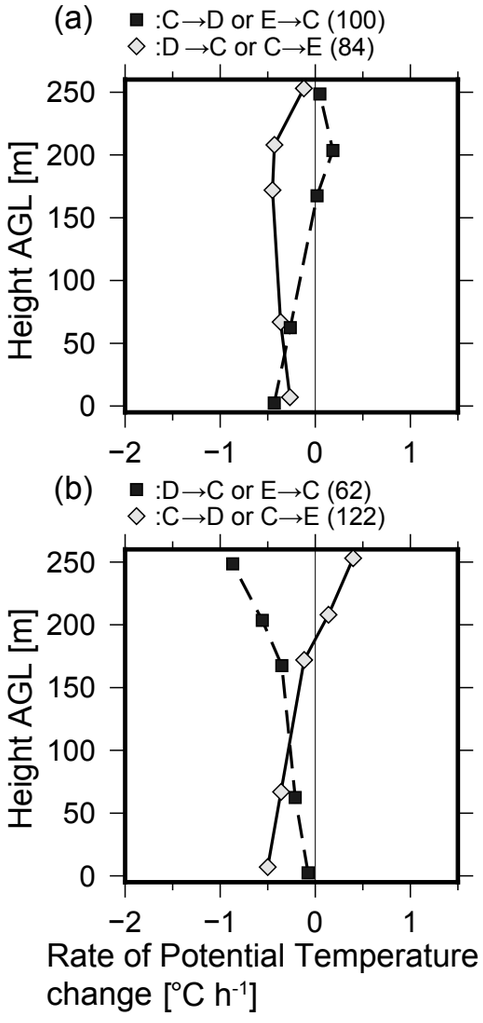

Figure 20: Average rate of potential temperature change during different clusters transitions

Numbers in parentheses indicate the occurrence numbers of these transitions.

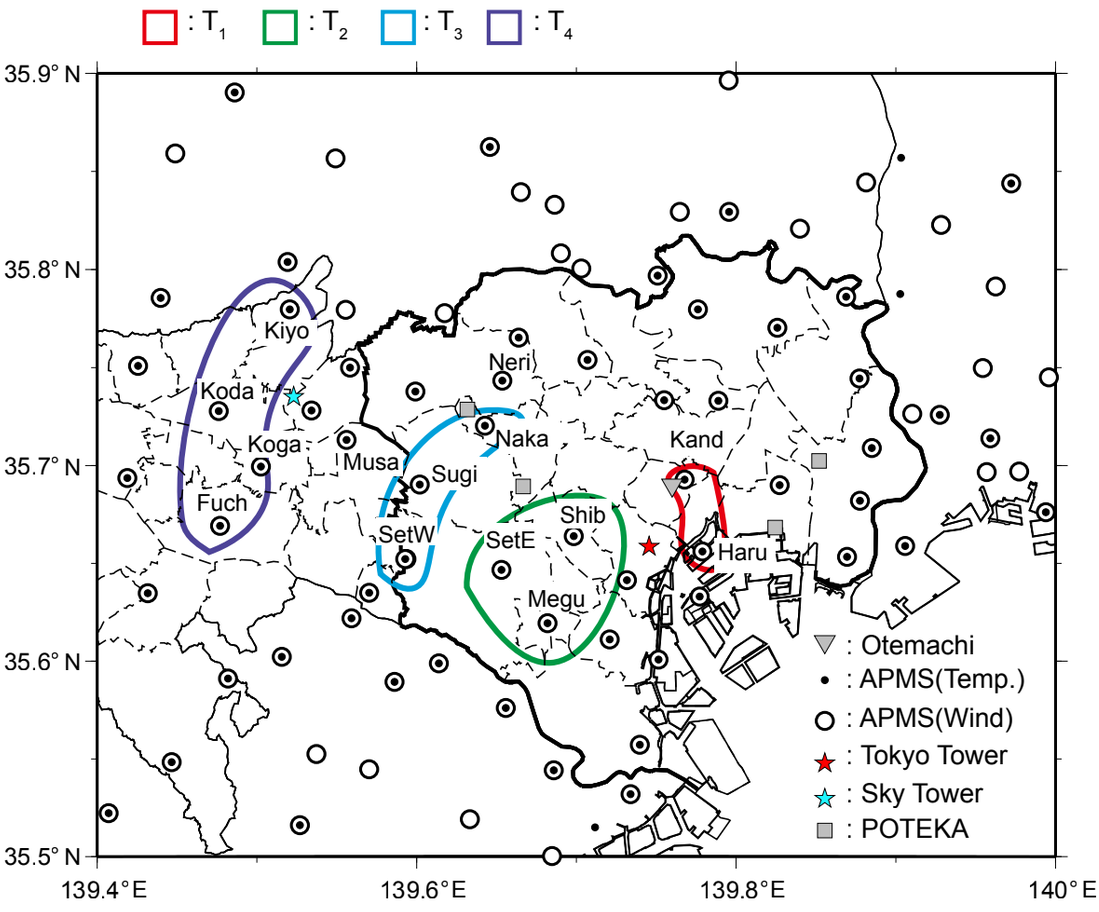

Abbreviation of APMS

Fuch: Fuchuushimiyanishichou
Haru: Chuuoukuharumi
Kand: Chiyodakukandatsukasachou
Kiyo: Kiyoseshikamikiyoto
Koda: Kodairashiogawachou
Koga: Koganeishihonchou
Megu: Megurokuhimonya
Musa: Musashinoshisekimae
Naka: Nakanokuwakamiya
Neri: Nerimakunerima
SetE: Setagayakusetagaya
SetW: Setagayakuseijou
Shib: Shibuyakuudagawachou
Sugi: Suginamikukugayama

Figure 21: Index map showing the target area and the distribution of observatories.

The APMS stations mentioned in text are listed as abbreviation. The thick line indicates the boundary of the Tokyo Wards area.

The stations within the red, green, blue, purple lines were used to derive ave rage temperatures T_1, T_2, T_3 and T_4, respectively (see text details).

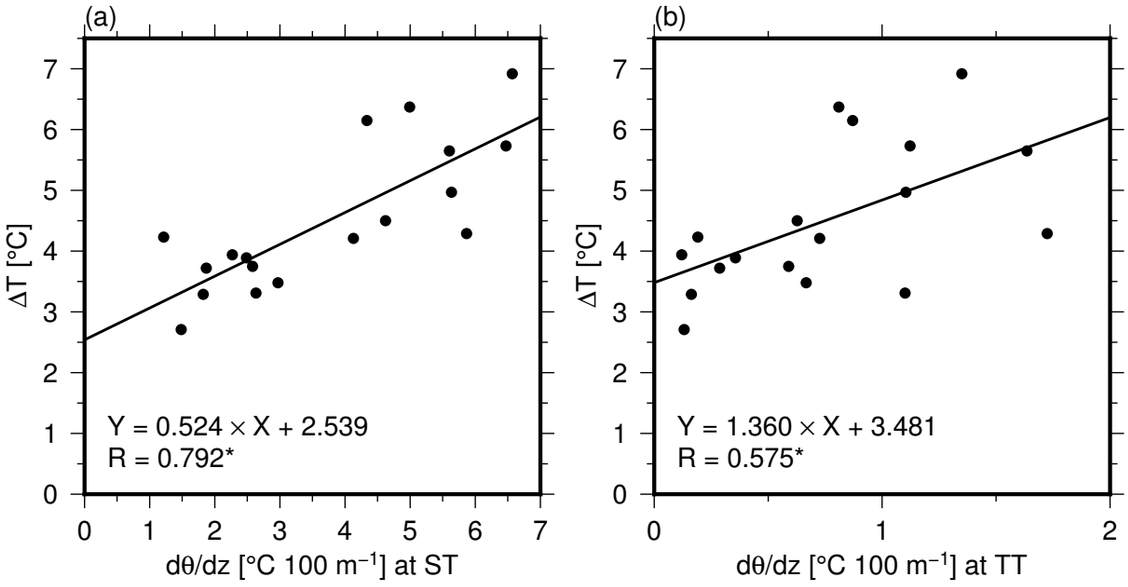

Figure 22: Relationship between temperature difference (ΔT) and potential temperature gradient at (a) ST and (b) TT at 06:00 JST

The formula and R at the bottom left of each panel denote the regression equation and correlation coefficient, respectively. Asterisks indicate that the correlation is statistically significant at the 1% level.

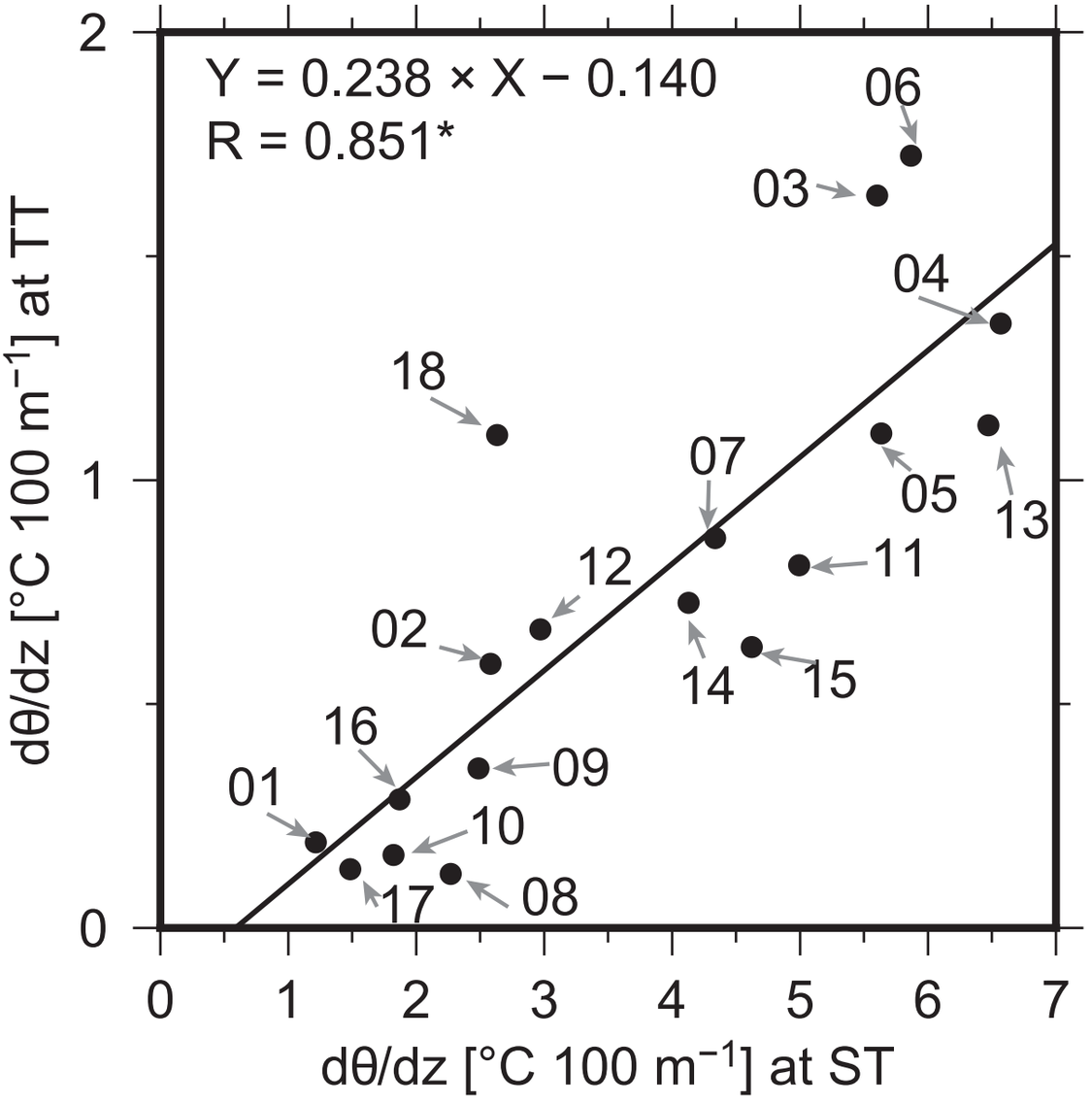

Figure 23: Relationship between the potential temperature gradients (dθ/dz) at the ST and TT at 06:00 JST

The formula and R at the top left in each panel denote the regression formula and correlation coefficient, respectively. Asterisks indicate that the correlation is statistically significant at the 1% level. Numbers mean the date of clear nights width weak wind (see Table 2).

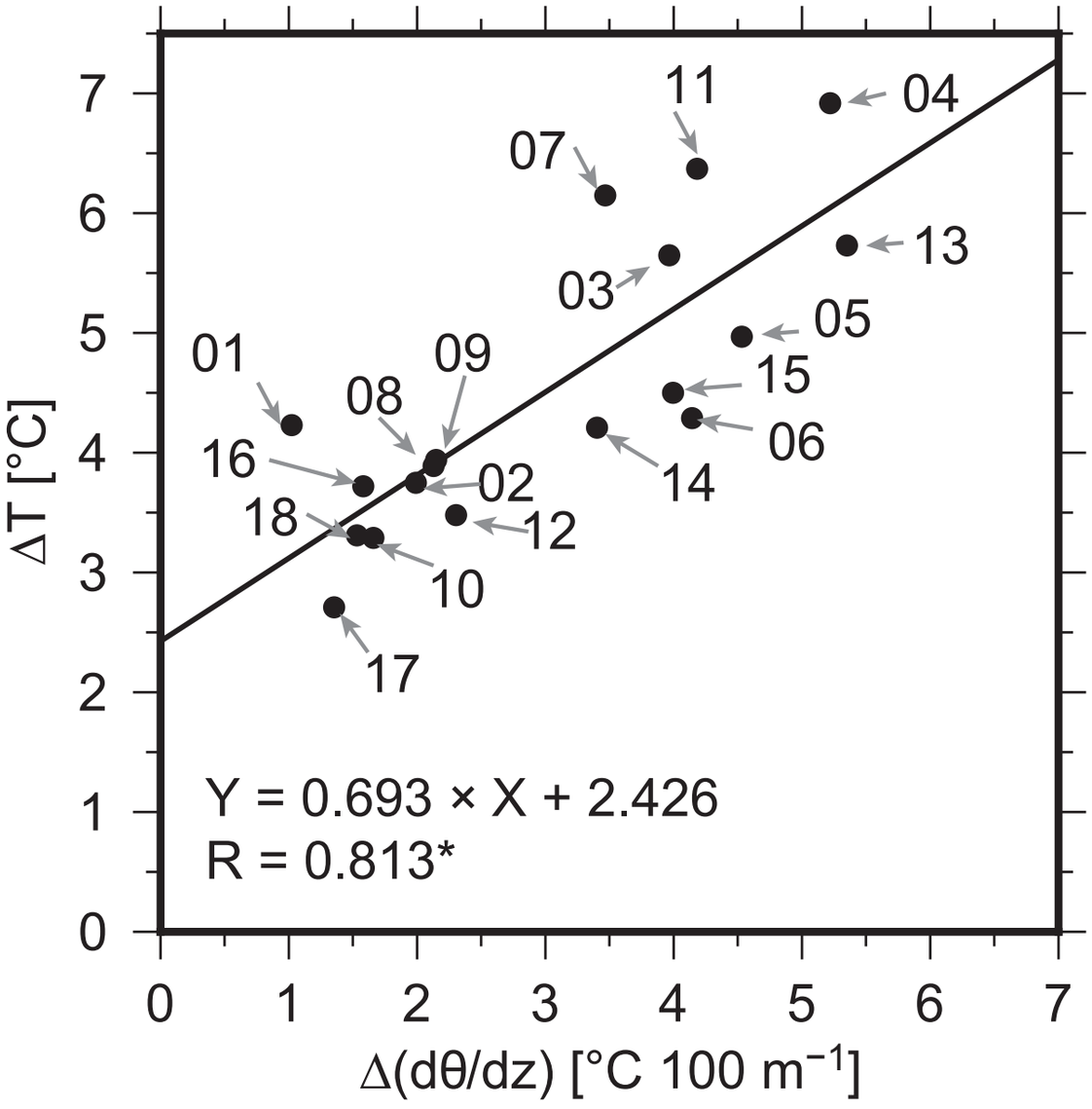

Figure 24: Relationship between the temperature difference (ΔT) and difference in potential temperature gradient Δ(dθ/dz) at 06:00 JST

Δ(dθ/dz) is potential temperature difference between at the ST and TT. The formula and R at the bottom left of each panel denote the regression formula and correlation coefficient, respectively. Asterisks indicate that the correlation is statistically significant at the 1% level. Numbers mean the date of clear nights width weak wind (see Table 2).

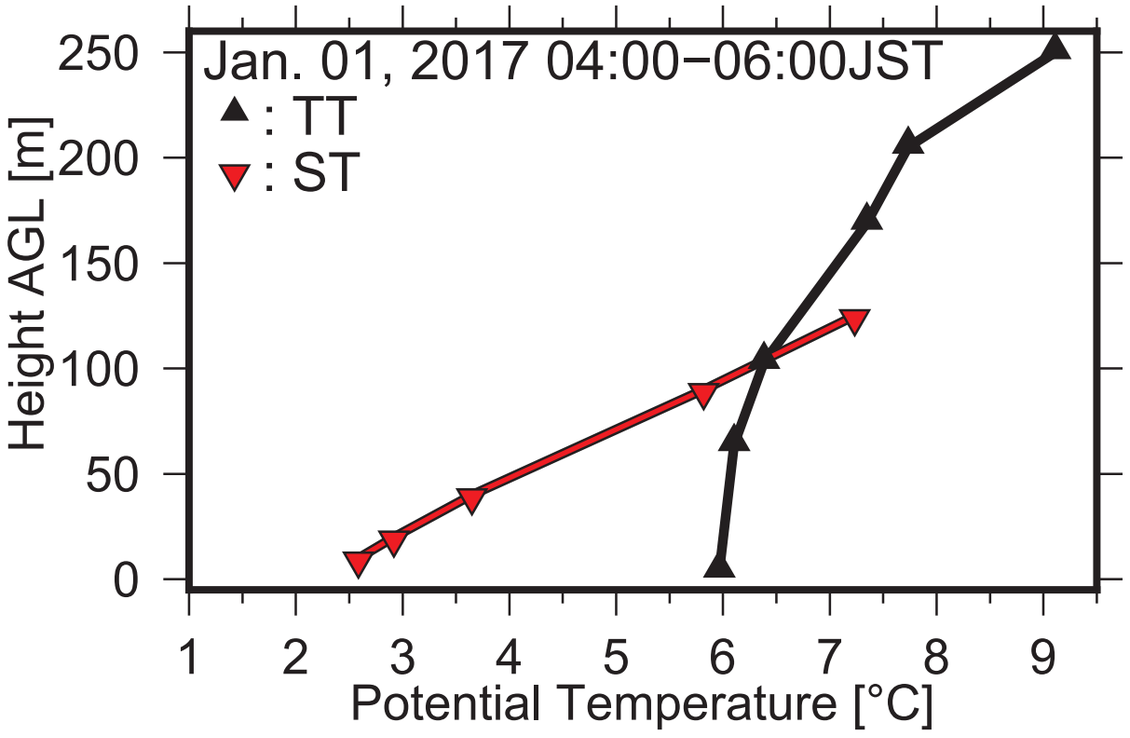

Figure 25: Vertical potential temperature profiles at the TT and ST on the night of January 1, 2017, averaged over 04:00–06:00 JST

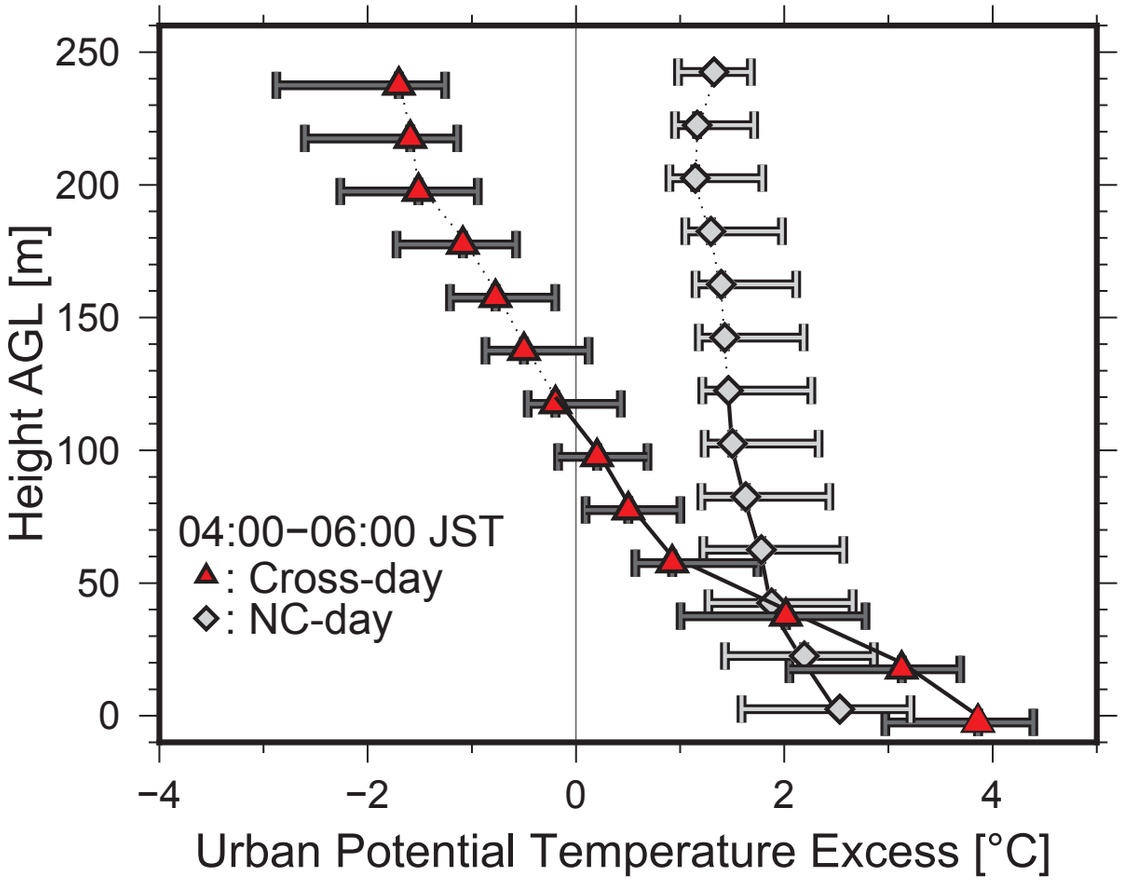

Figure 26: Vertical variations in potential temperature difference between the urban (TT) and non-urban (ST) areas (HII), averaged over 04:00–06:00 JST

On Cross-days, the coincident point was found below 250 m; on NC-days, no coincident point was found at this height. Symbols are placed at the 50th percentile, and error bars span the 25th to 75th percentiles.

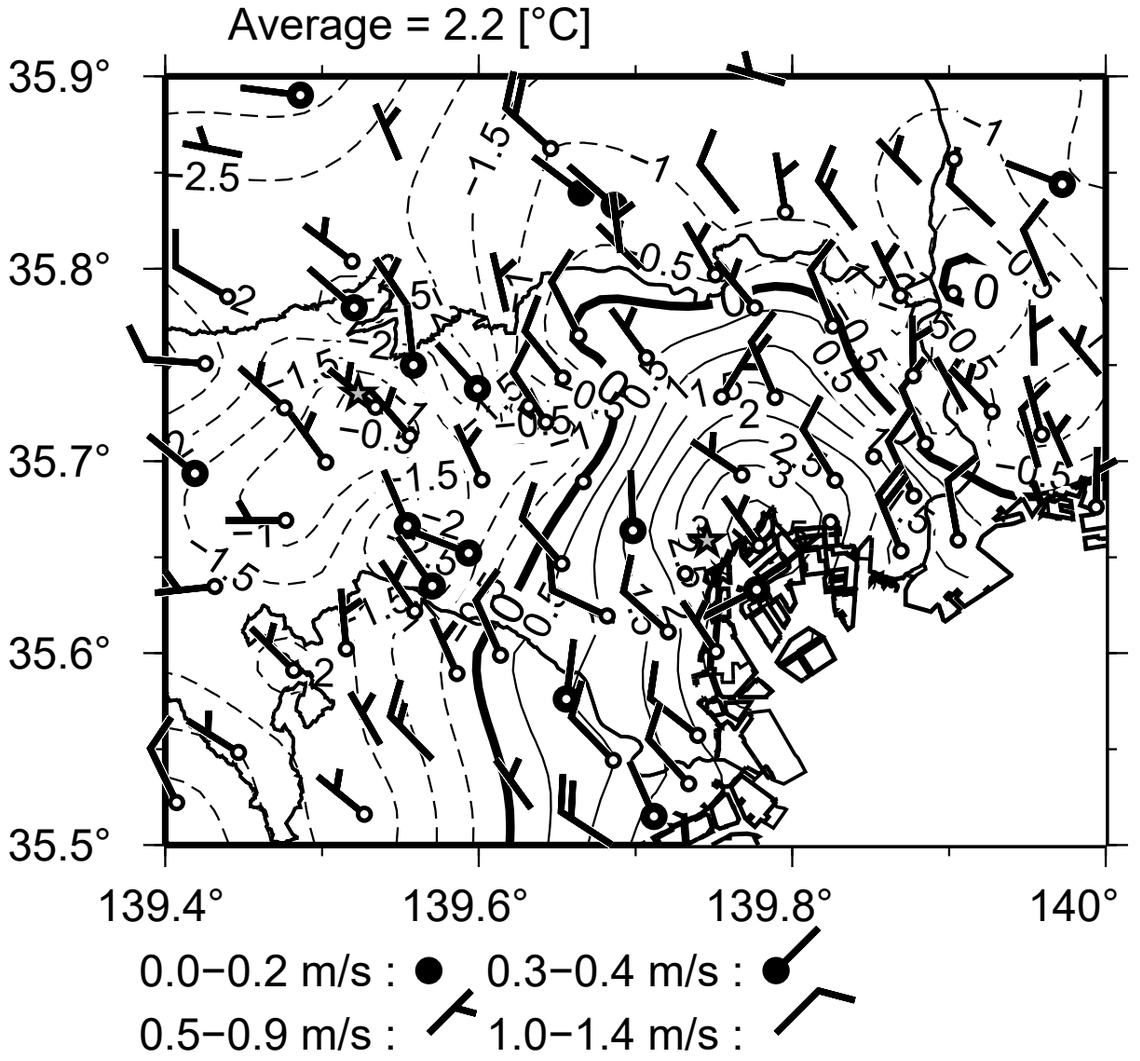

Figure 27: Composite map of temperature deviation from the average spatial temperature and the wind system in and around the Tokyo Wards area, averaged over 2400–0600 JST on Cross-days

The dashed, solid, and thick lines represent the negative, positive, and zero temperature deviations, respectively.

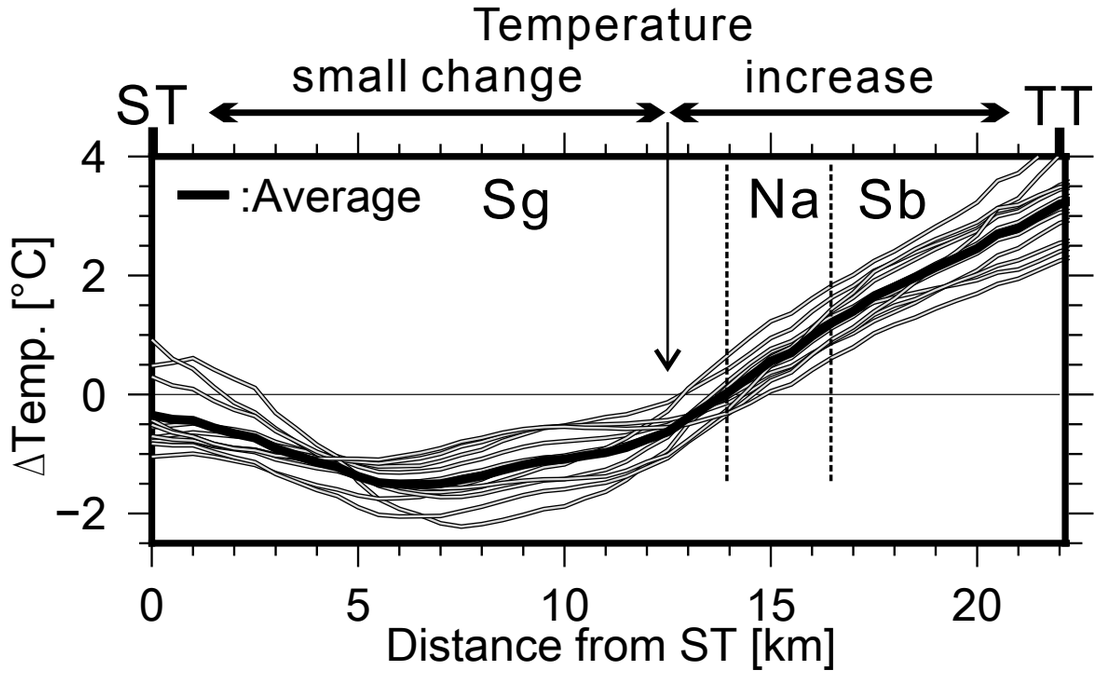

Figure 28: Horizontal profiles of temperature deviation (gray) from the average spatial temperature (black) in various cases on Cross-days along the ST–TT cross-section.

The left and right dotted lines indicate the boundaries between Suginami (Sg) and Nakano (Na) Wards and between Na and Shibuya (Sb) Wards, respectively.

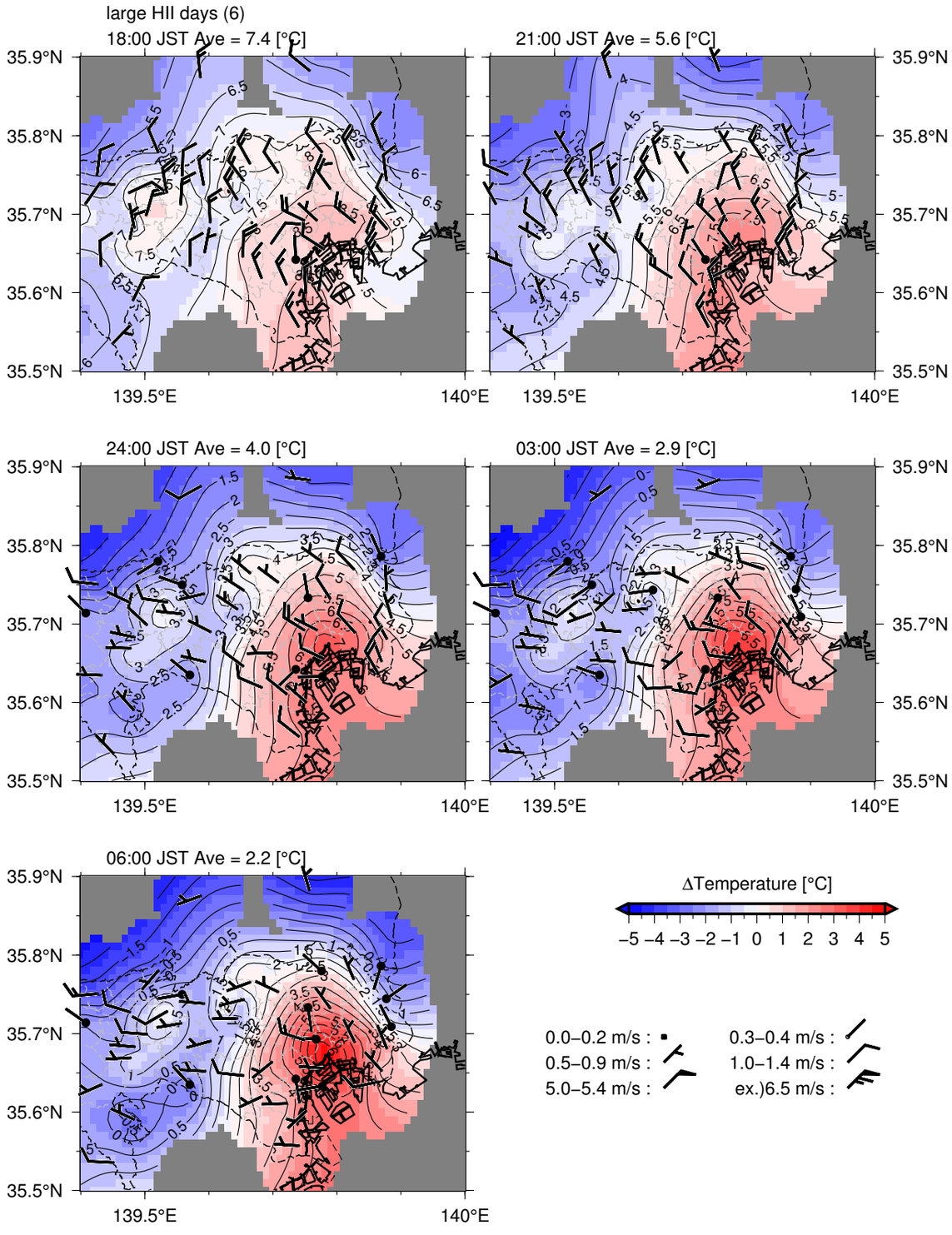

Figure 29: Distributions of temperature deviation (colors), temperature (contours) and the wind system around the Tokyo Wards area on large-HII days at 4-h intervals starting from 18:00 JST

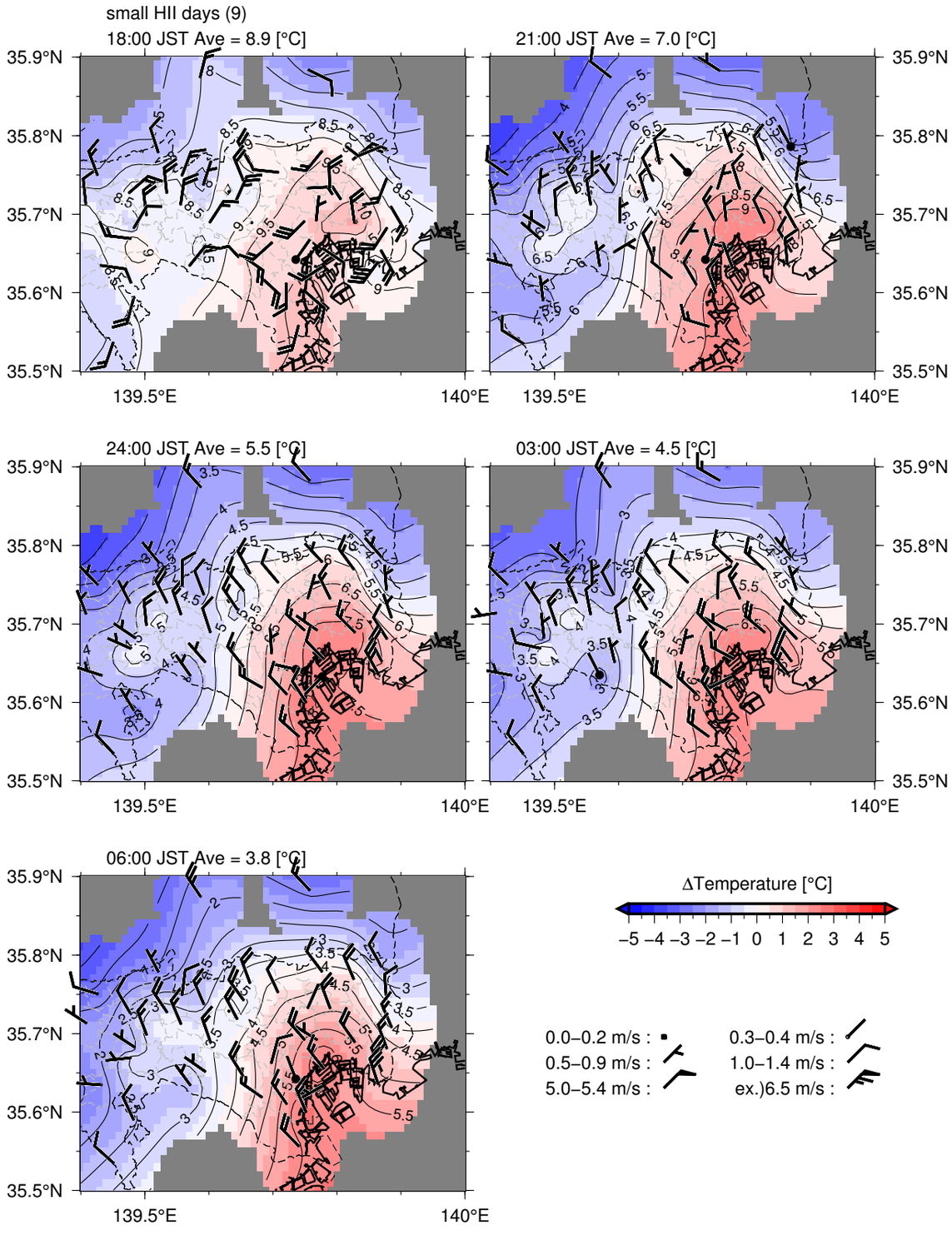

Figure 30: Distributions of temperature deviation (colors), temperature (contours) and the wind system around the Tokyo Wards area on small-HII days at 4-h intervals starting from 18:00 JST

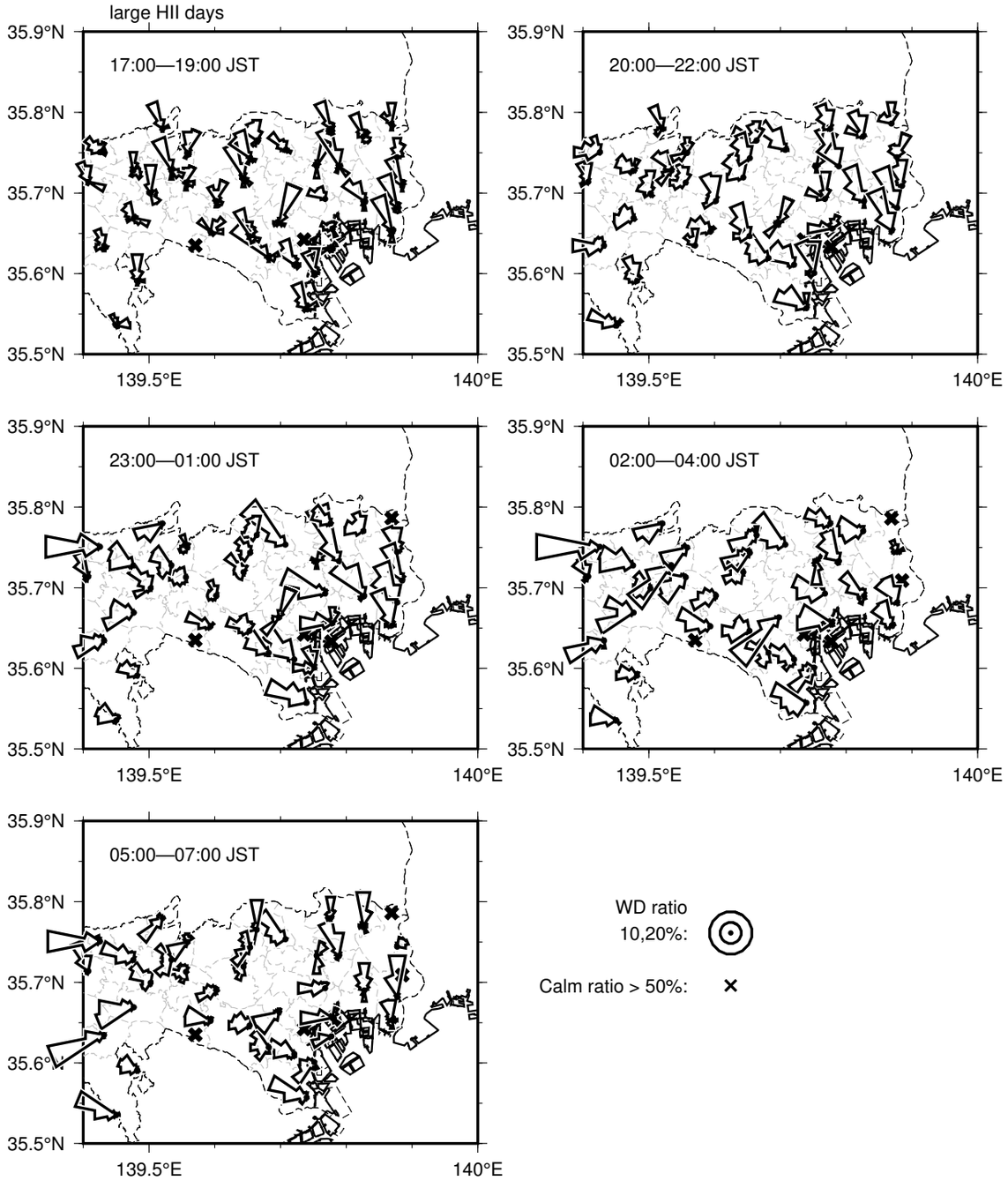

Figure 31: Wind rose at each APMS on large-HII nights at 4-h intervals starting from 18:00 JST

The station at which the recording frequency of calm winds ($\leq$0.1 m s^{-1}) exceeded 50% is marked by a cross (x). The sizes of wind roses indicate the ratio of wind direction.

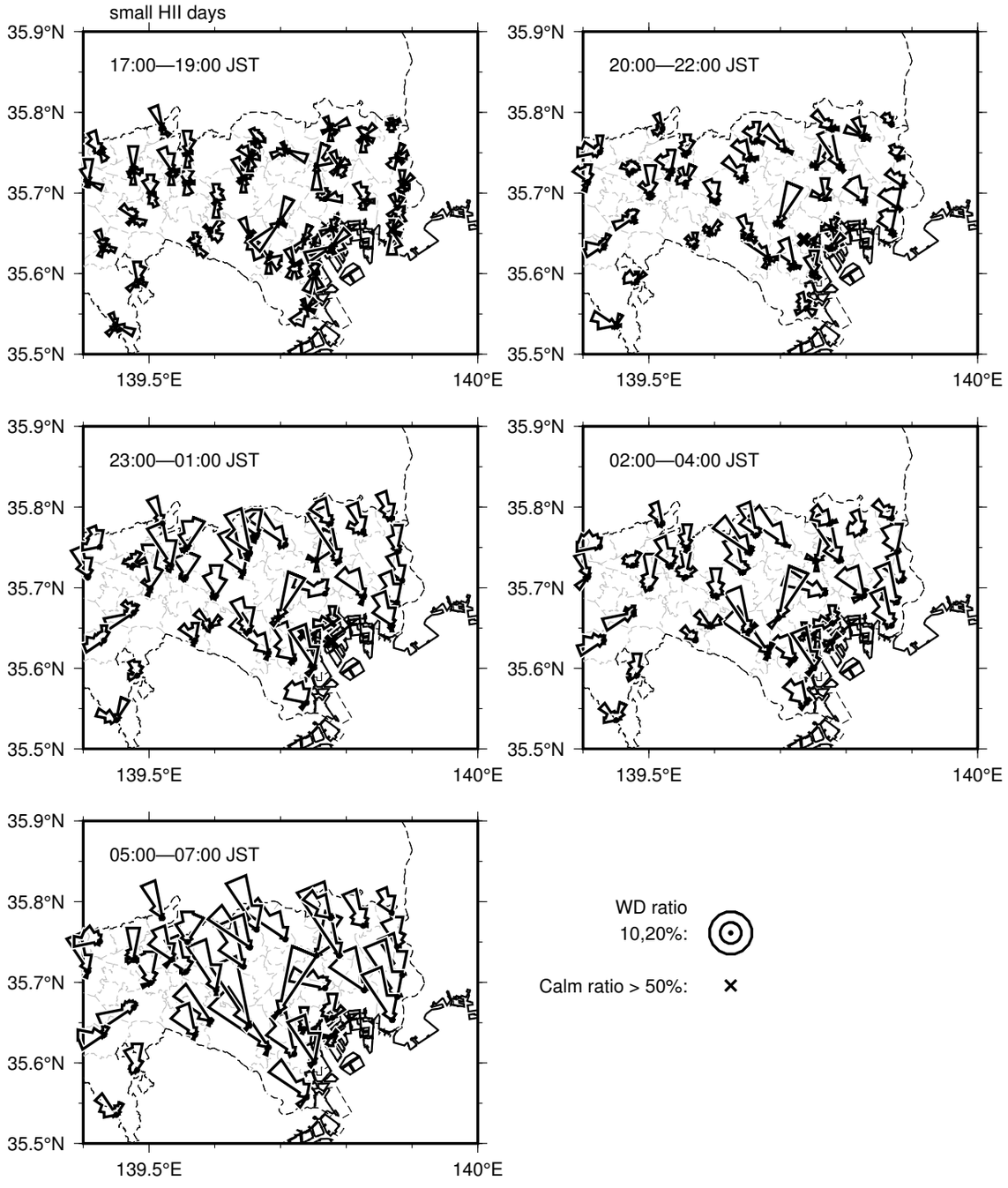

Figure 32: Wind rose at each APMS on small-HII nights at 4-h intervals starting from 18:00 JST

The station at which the recording frequency of calm winds ($\leq$0.1 m s^{-1}) exceeded 50% is marked by a cross (x). The sizes of wind roses indicate the ratio of wind direction.

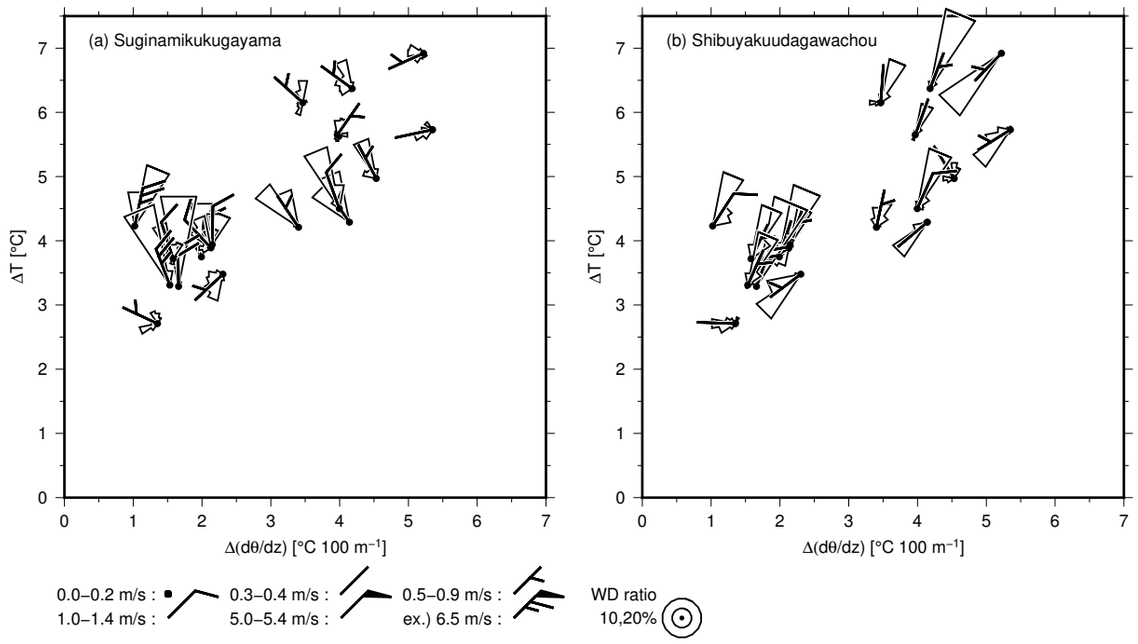

Figure 33: Wind barbs and wind roses at (a) Suginamikukugayama and (b) Shibuyakuudagawachou are superimposed on the plot of temperature difference (ΔT) and difference potential temperature gradient between ST and TT Δ(dθ/dz) at 06:00 JST

ΔT is temperature difference between the urban side of the cliff and the area outside of the cliff same as Fig. 23 (b). The wind barbs and wind roses are the vector averages and frequencies of the WD, respectively, during 23:00–01:00 JST.

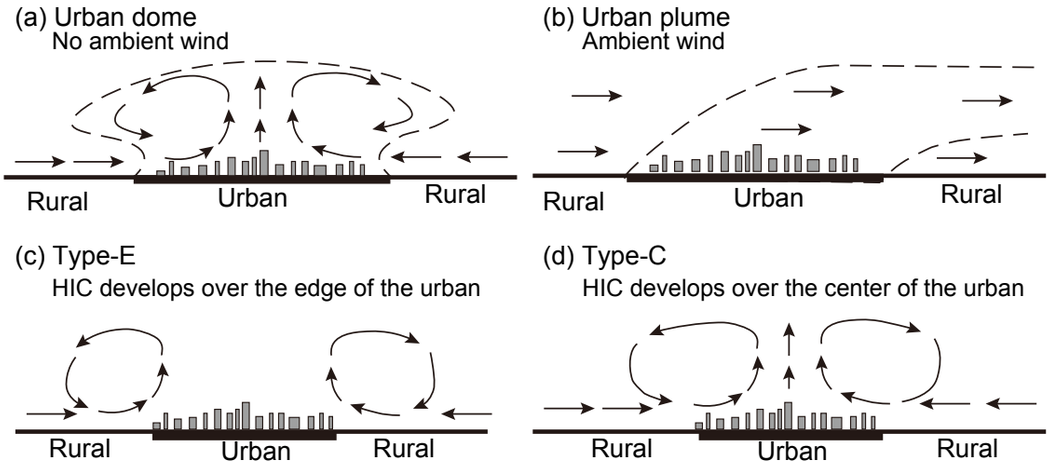

Figure 34: Typical mesoscale formations of urban boundary layers: (a) urban dome, (b) urban plume, (c) type-E urban dome, in which the heat island circulation (HIC) develops over the edge of the urban area, and (d) type-C urban dome, in which the HIC develops over the center of the urban area

(after Oke *et al.* (2017) and Kimura (1975)).

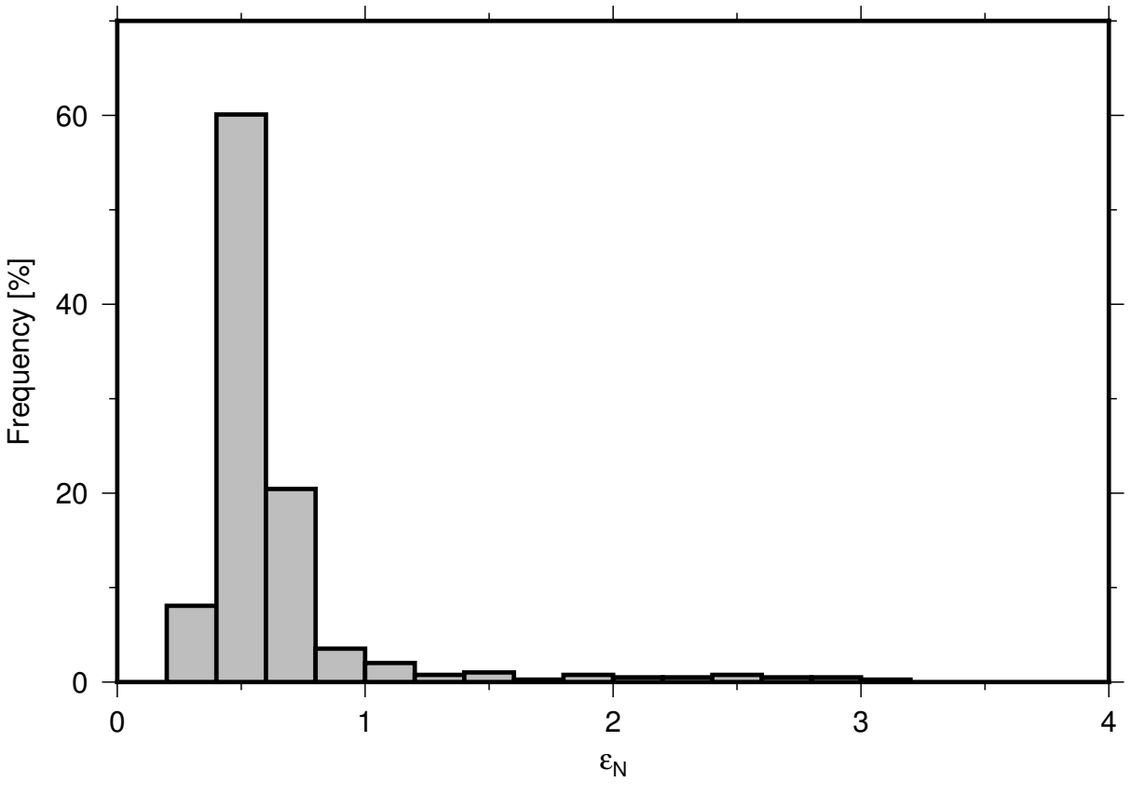

Figure 35: Relative occurrence frequencies (%) of the non-dimensional parameter ε_N characterizing type-E to type-C transitions. Data were recorded between 20:00 JST and 06:00 JST

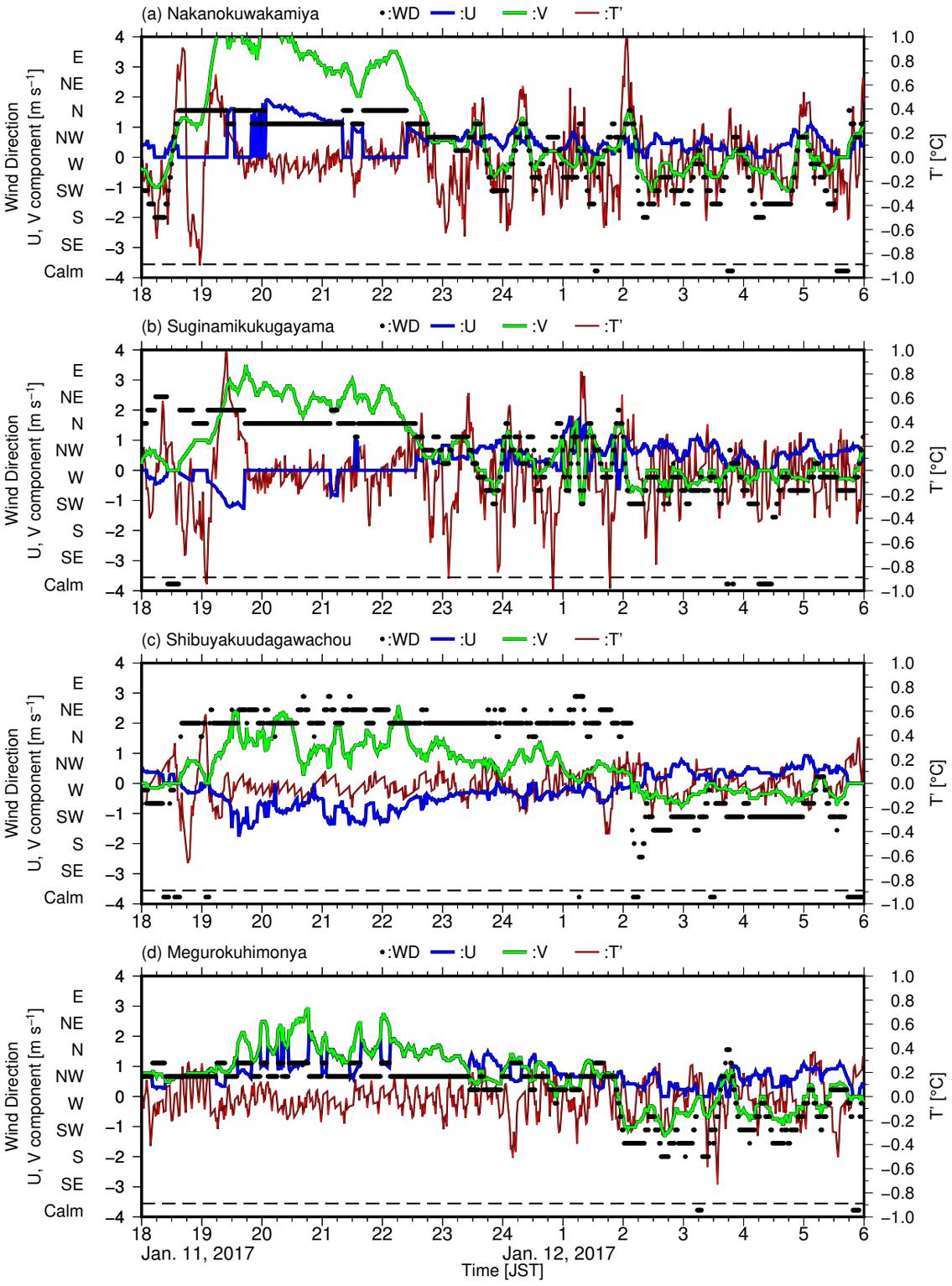

Figure 36: Temporal variations of the WD, the zonal (U) and meridional (V) components of the wind speed, and the temperature deviation from $\overline{T}$ (T') in Case-1 (January 11–12, 2017)

(a) Nakanokuwakamiya, (b) Suginamikukugayama, (c) Shibuyakuudagawachou, and (d) Megurokuhimonya. $\overline{T}$ is 61-min moving-average temperature.

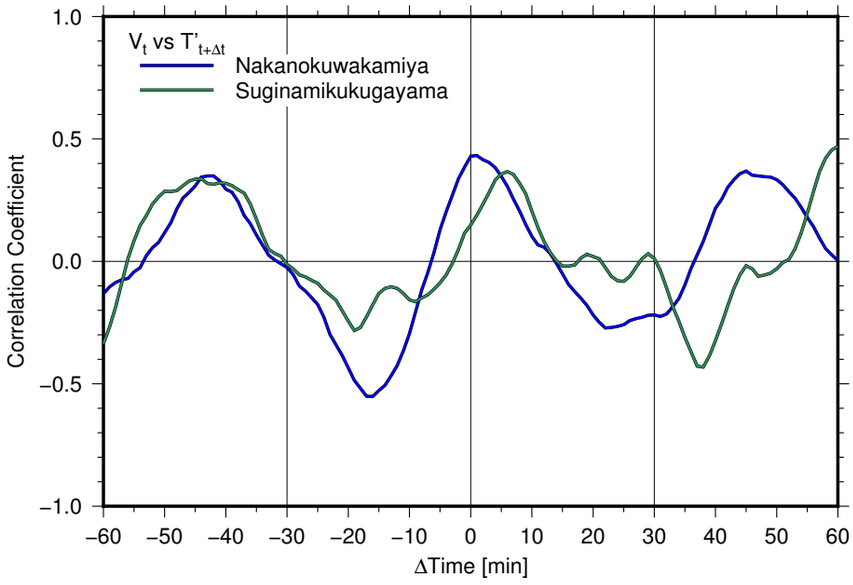

Figure 37: Lag in correlation coefficient between V and T' at Nakanokuwakamiya and Suginamikukugayama between 23:00–02:00 JST

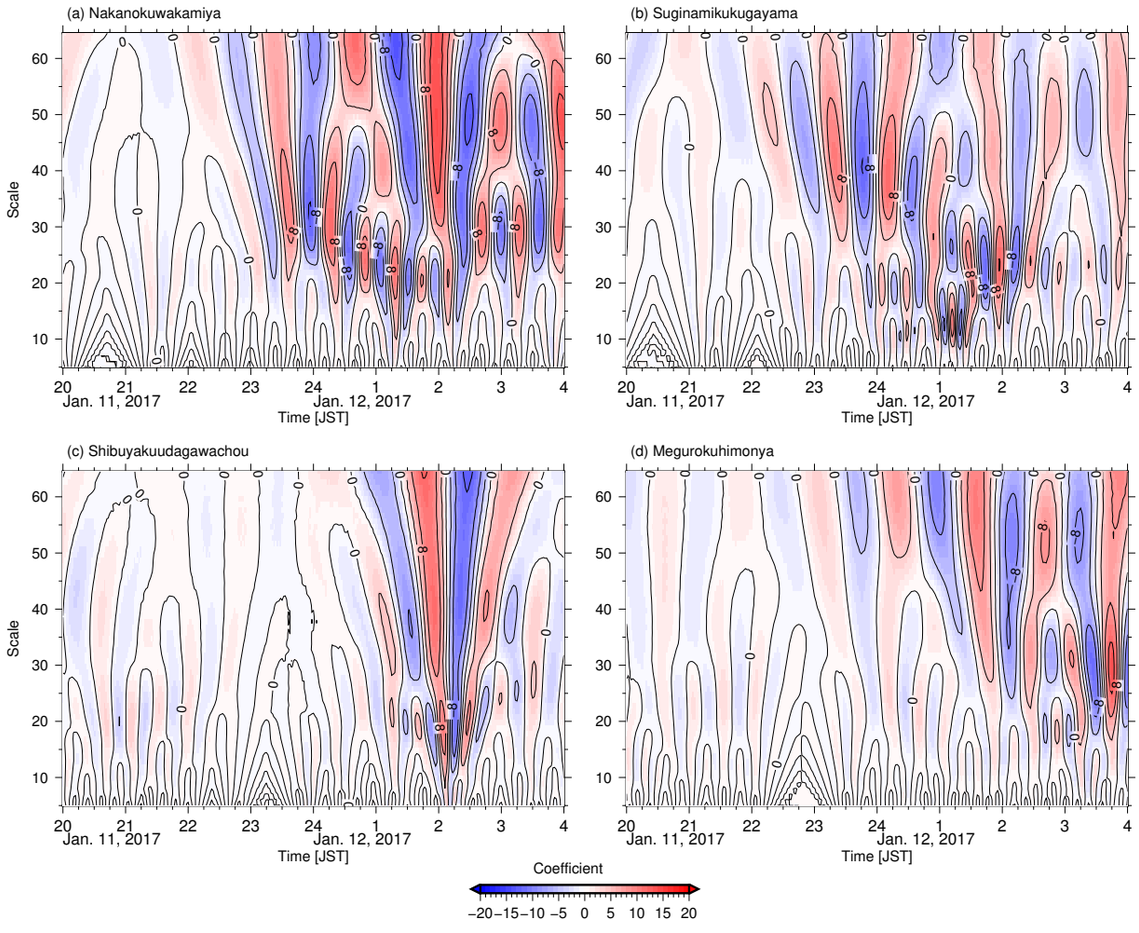

Figure 38: Time-frequency distributions of the meridional wind-speed component obtained by Morlet wavelet analysis: (a) Nakanokuwakamiya, (b) Suginamikukugayama, (c) Shibuyakuudagawachou, (d) Megurokuhimonya

Analyzed data were collected from 20:00 JST January 11, 2017 to 04:00 JST January 12, 2017. The colors indicate the amplitude of the real part of the wavelet coefficient.

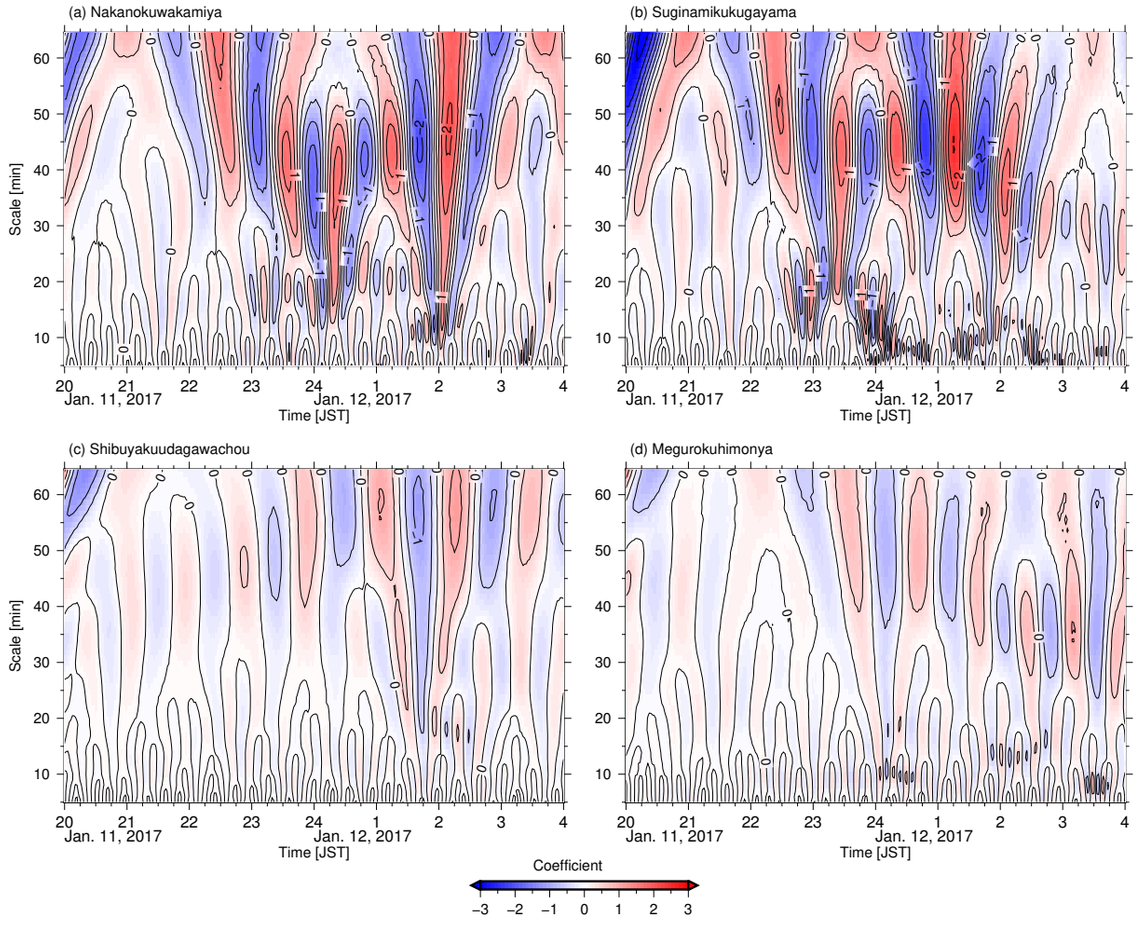

Figure 39: Time-frequency distributions of temperature obtained by Morlet wavelet analysis: (a) Nakanokuwakamiya, (b) Suginamikukugayama, (c) Shibuyakuudagawachou, (d) Megurokuhimonya

Analyzed data were collected from 20:00 JST January 11, 2017 to 04:00 JST January 12, 2017. The colors indicate the amplitude of the real part of the wavelet coefficient.

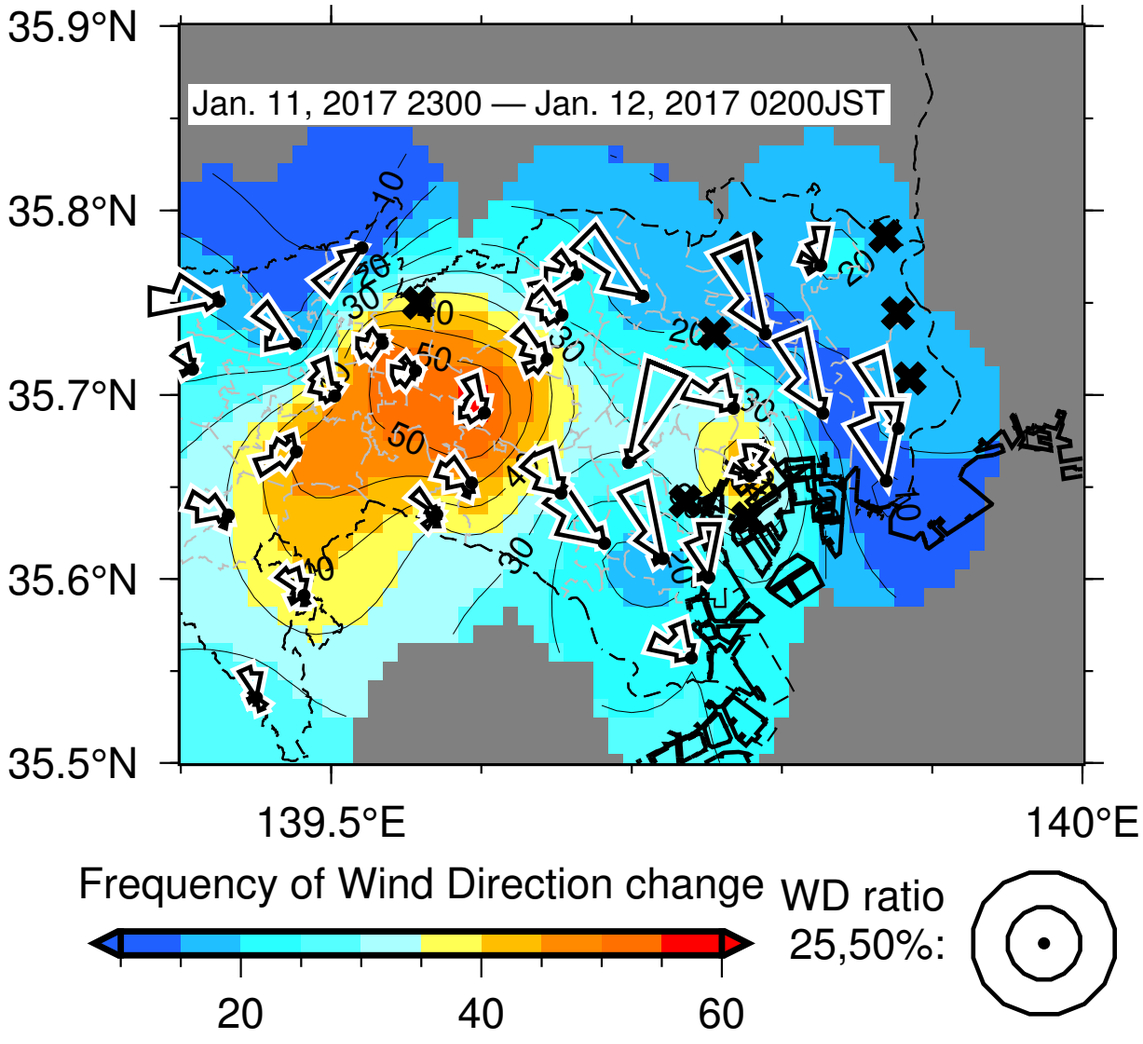

Figure 40: Distributions of wind roses and frequencies of wind-direction changes from 23:00 JST January 11, 2017 to 02:00 JST January 12, 2017

Observation points recording more than 60 min of calm conditions are marked by $\times$.

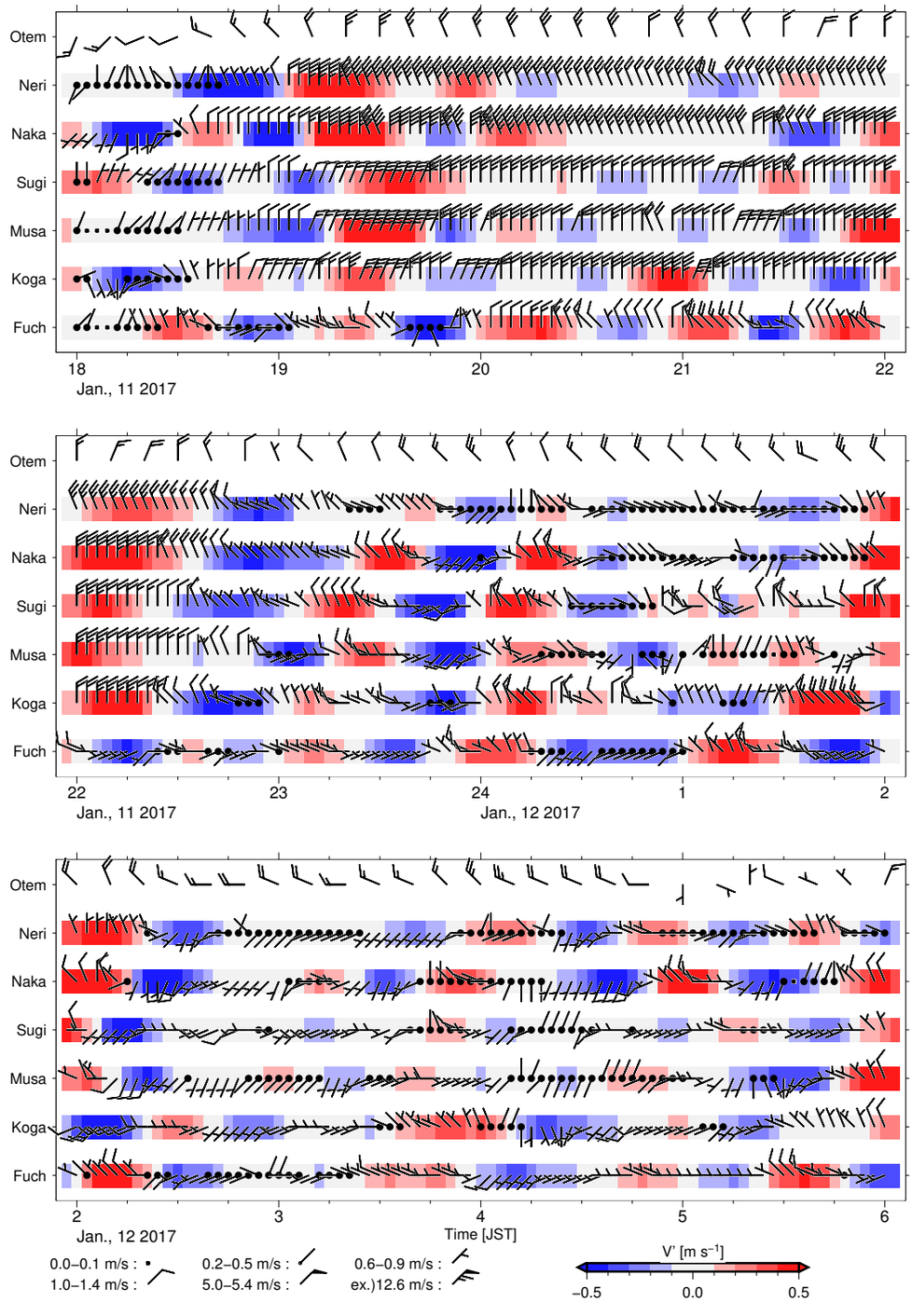

Figure 41: Temporal variation of wind barbs in the horizontal plane along the Otemachi–Fuchu cross-section from 18:00 JST January 11, 2017 to 06:00 JST January 12, 2017

Fuch, Koga, Musa, Sugi, Naka, Neri and Kita denote Fuchuushimiyanishichou, Koganeishihonchou, Musashinoshisekimae, Suginamikukugayama, Nakanokuwakamiya, Nerimakunerima and Kitanomaru, respectively. V' indicates the 20–60-mins band-pass filtered V all stations except for Otemachi.

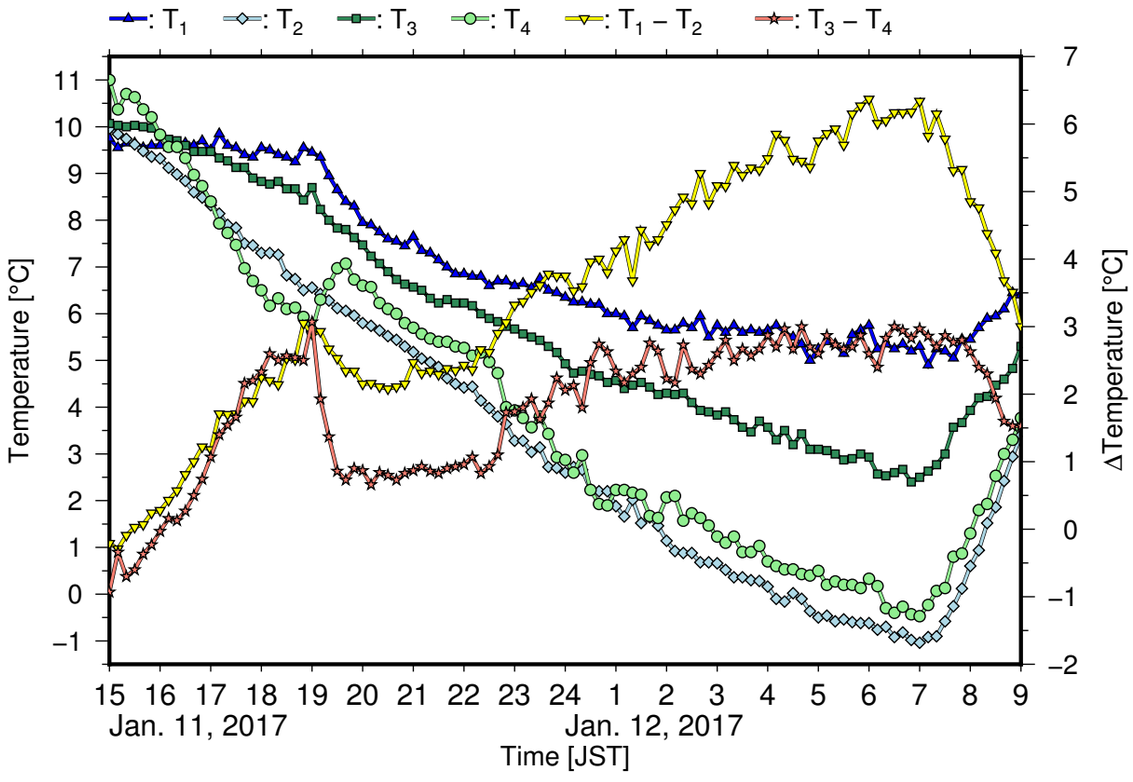

Figure 42: Temporal variations of the temperatures in different areas of the Tokyo metropolis (see text for details) and their differences in Case-1

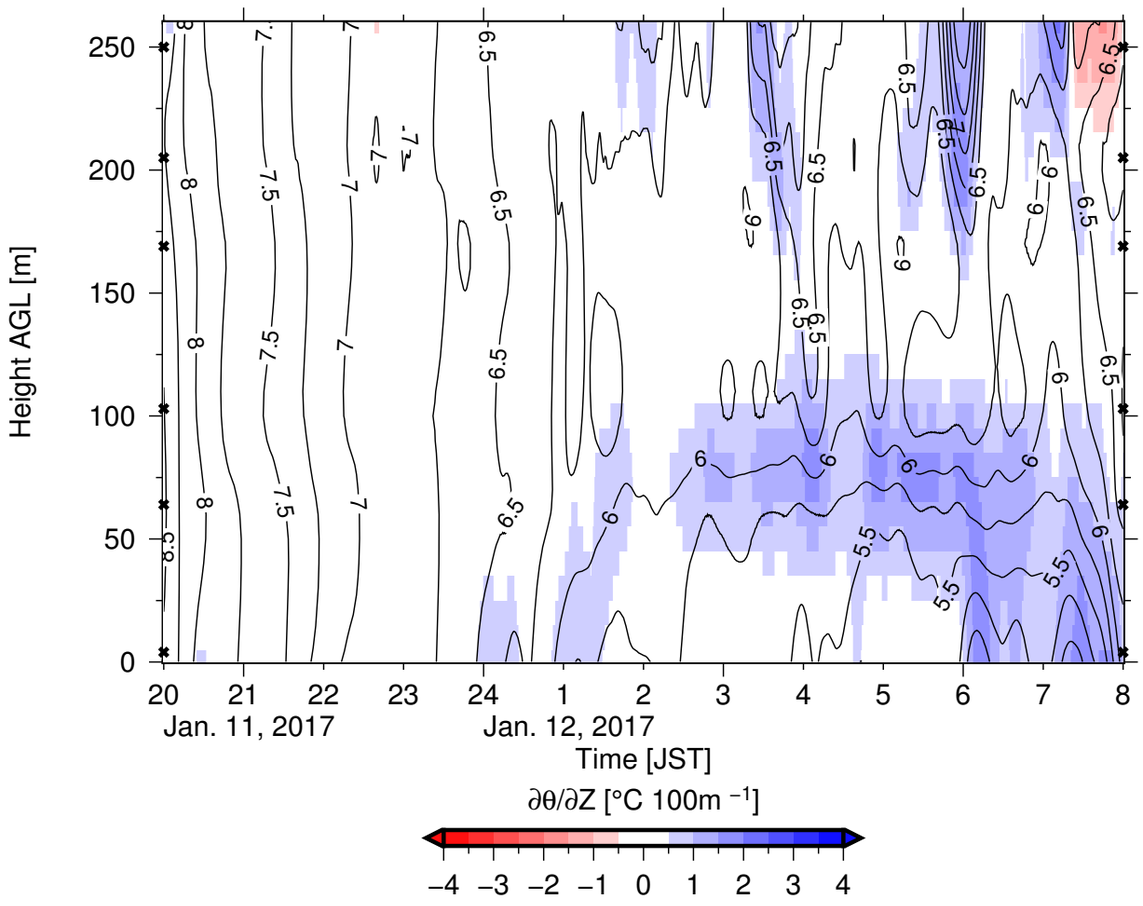

Figure 43: Temporal variations of the potential temperature (contours) and potential temperature gradient (colors) at the TT from 18:00 January 11, 2017 to 06:00 JST January 12, 2017

Analysis data were the moving-averaged values of the 10-min data. The contour interval is 0.25℃.

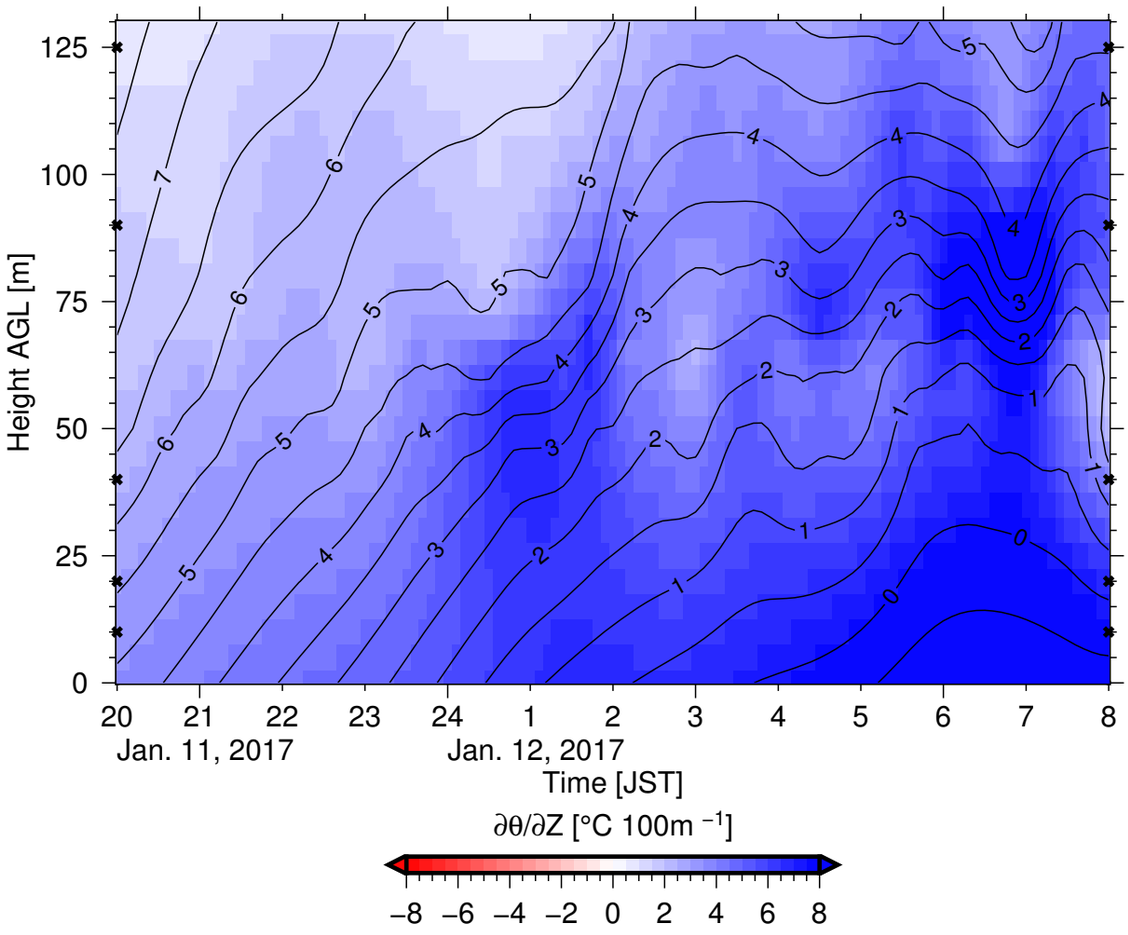

Figure 44: Temporal variation of the potential temperature (contours) and potential temperature gradient (colors) at the ST from 18:00 January 11, 2017 to 06:00 JST January 12, 2017

The contour interval is 0.5°C.

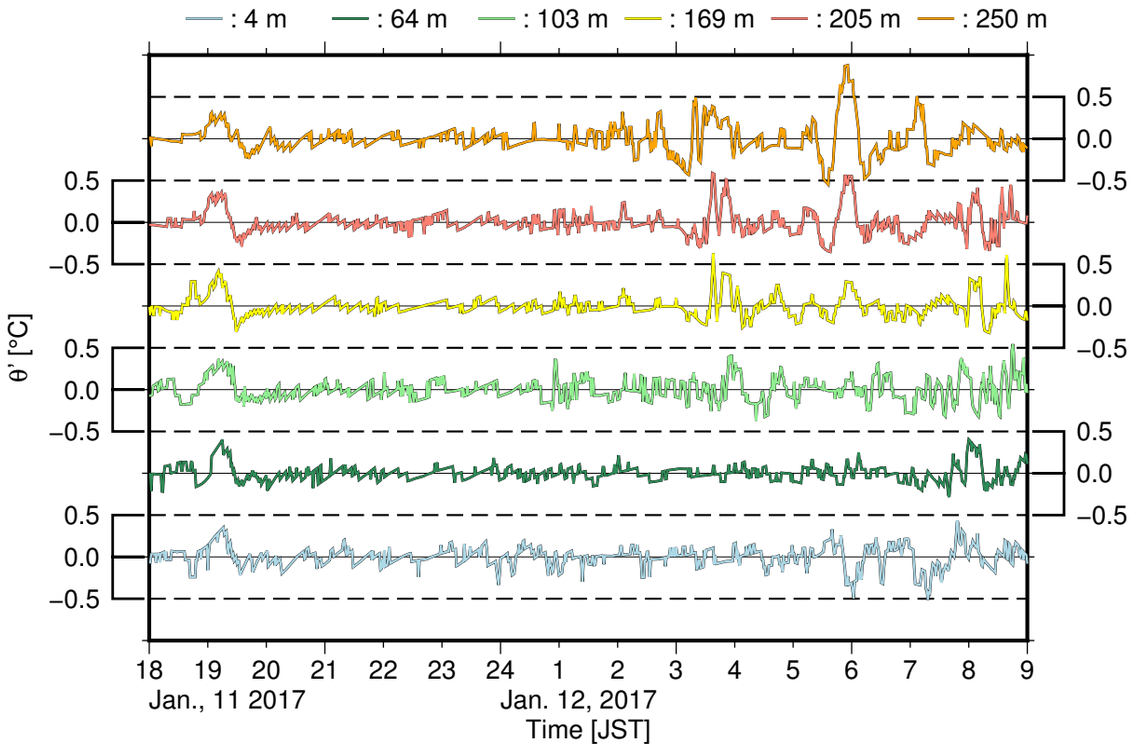

Figure 45: Vertical variations in θ' from 18:00 January 11, 2017 to 06:00 JST January 12, 2017

θ' is the potential temperature deviation from the 61-min moving average. Dashed lines represent the average $\pm$ 0.5℃. The lines are vertically shifted to avoid overlap.

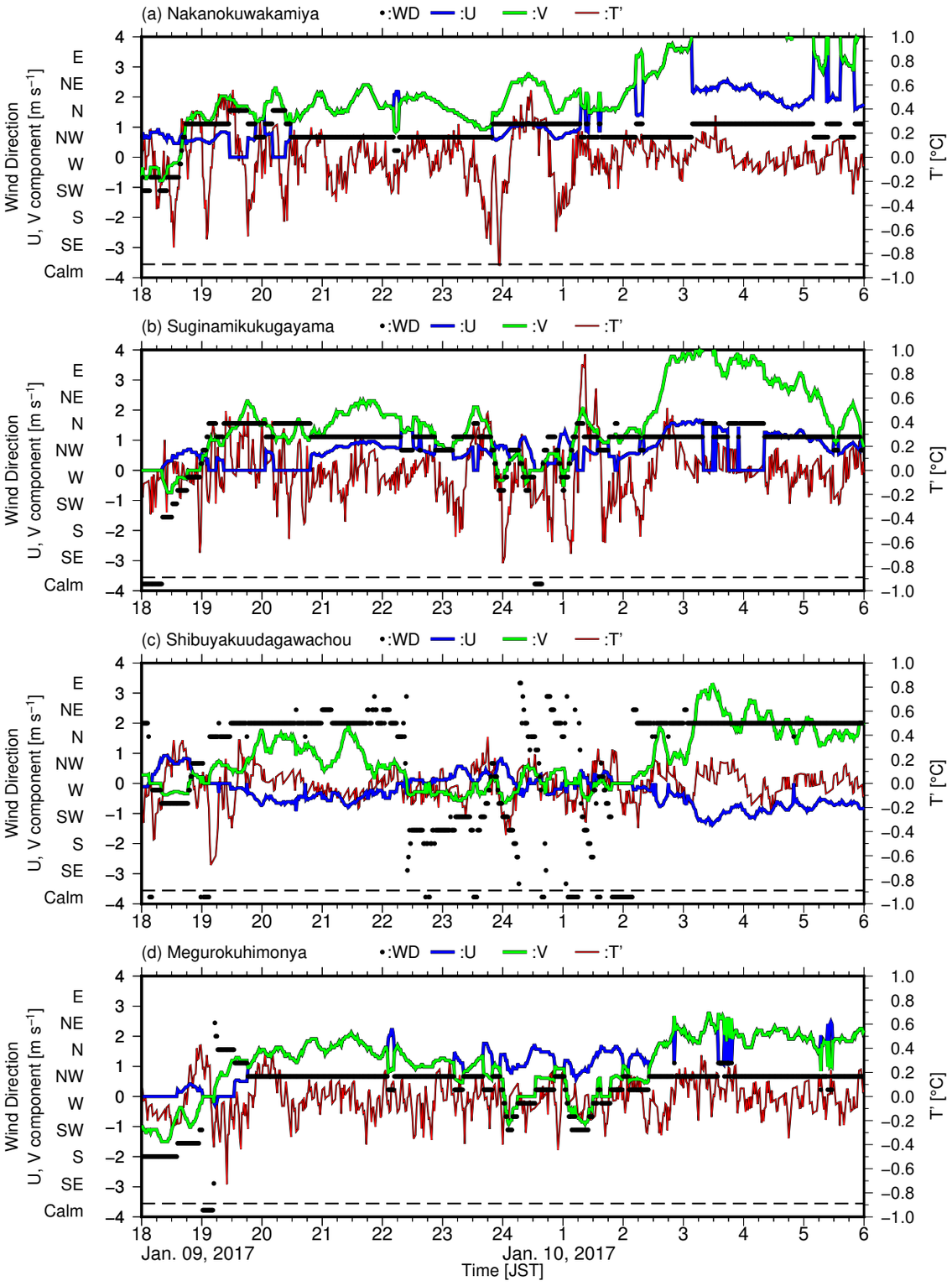

Figure 46: Temporal variations of the WD, the zonal (U) and meridional (V) components of the wind speed, and the temperature deviation from $\overline{T}$ (T') in Case-2 (January 09–10, 2017)

(a) Nakanokuwakamiya, (b) Suginamikukugayama, (c) Shibuyakuudagawachou, and (d) Megurokuhimonya. $\overline{T}$ is 61-min moving-average temperature.

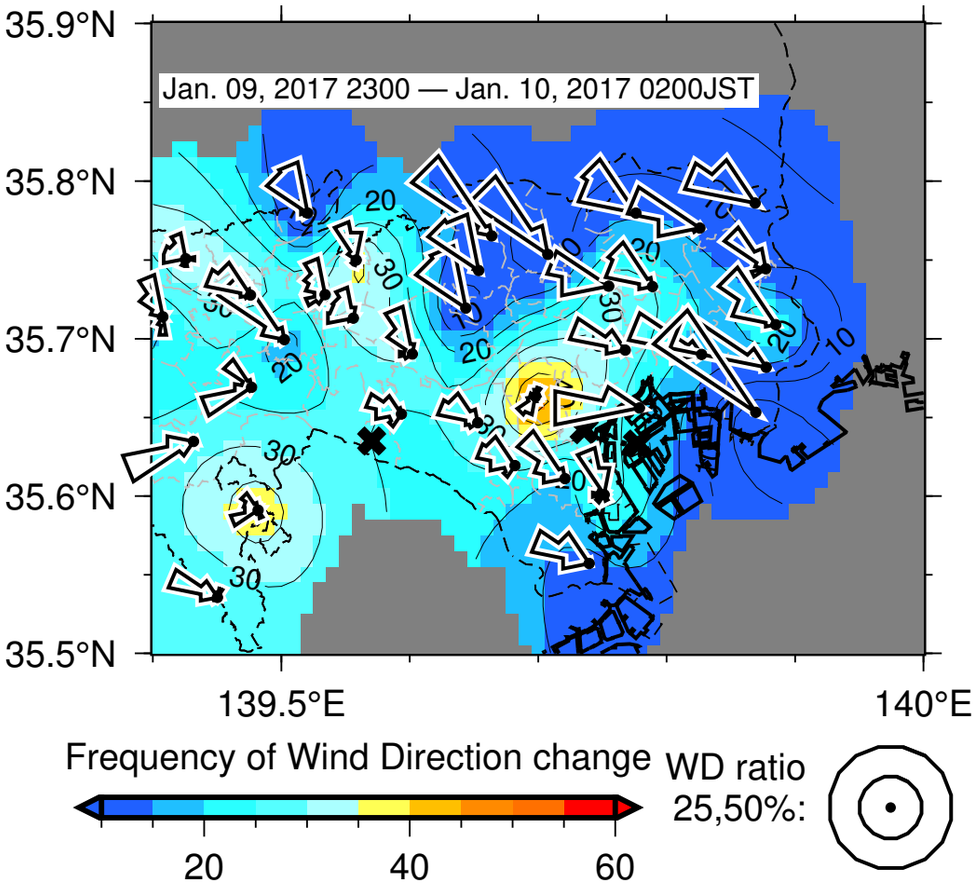

Figure 47: Distributions of wind roses and frequencies of wind-direction changes from 23:00 JST January 09, 2017 to 02:00 JST January 10, 2017

The observation stations recording more than 60 min of calm conditions are marked with ×.

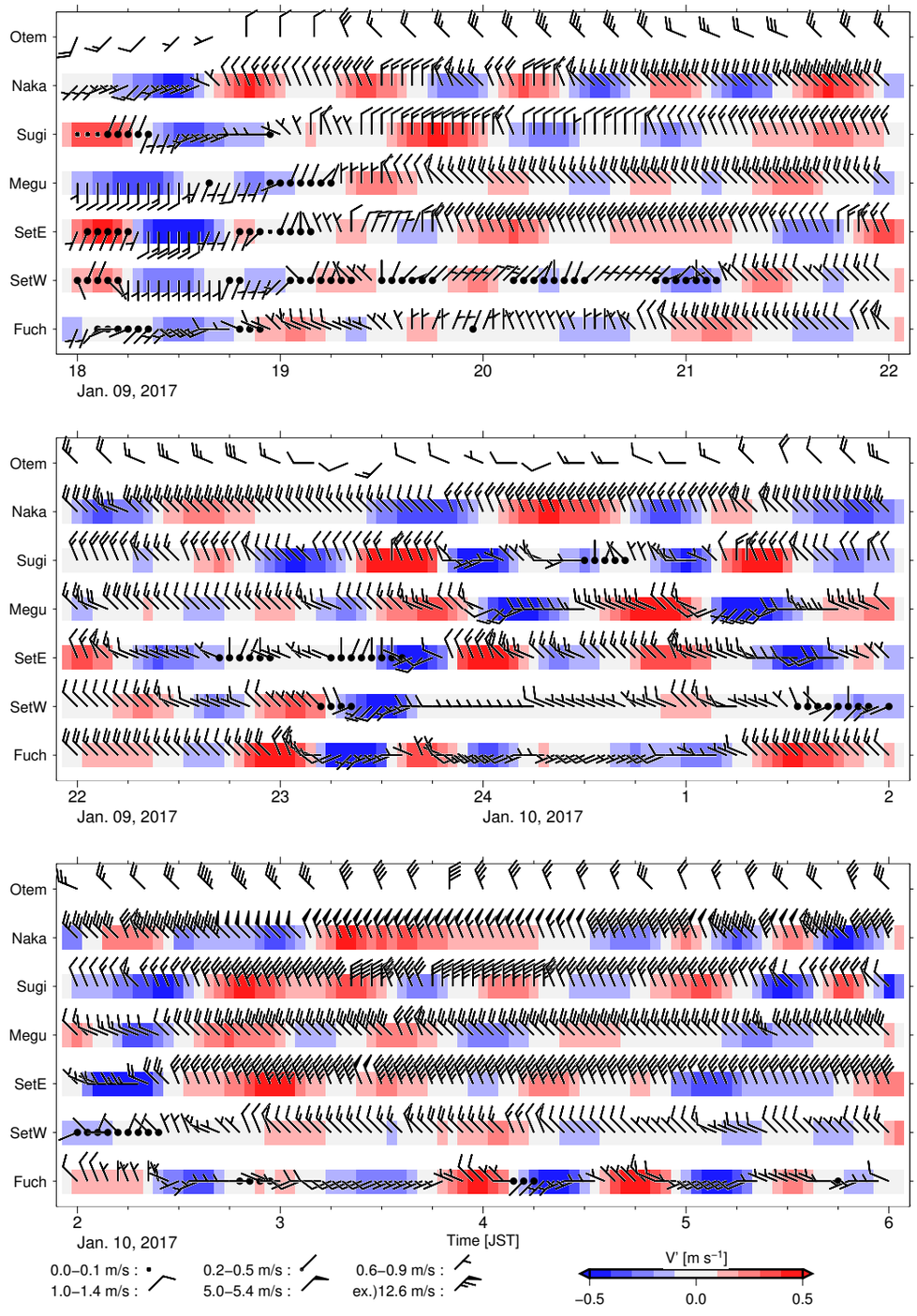

Figure 48: Temporal variation of wind barbs in the horizontal plane along the Otemachi–Fuchu cross-section from 18:00 JST January 09, 2017 to 06:00 JST January 10, 2017

Fuch, SetW, SetE, Sugi, Naka and Otem denote Fuchuushimiyanishichou, Setagayakuseijou, Setagayakusetagaya, Suginamikukugayama, Nakanokuwakamiya and Otemachi, respectively. V' indicates the 20–60-mins band-pass filtered V all stations except for Otemachi.

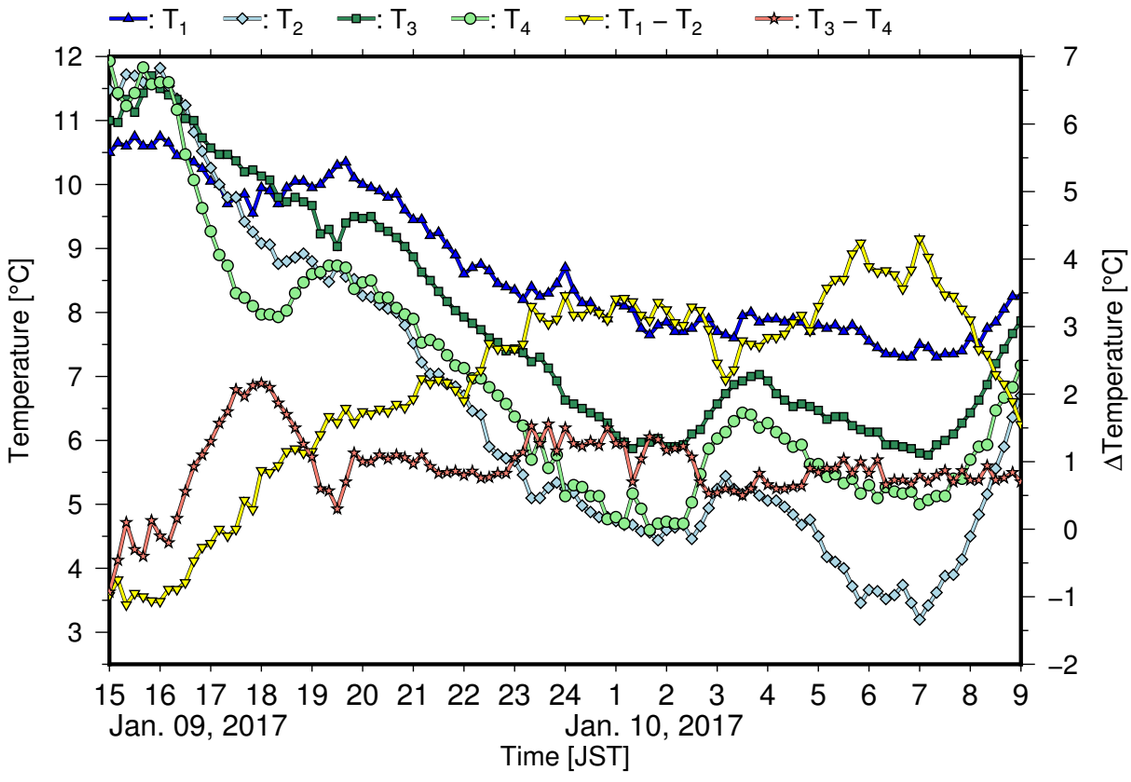

Figure 49: Temporal variations of temperatures in different areas of the Tokyo metropolis (see text for details) and their differences in Case-2

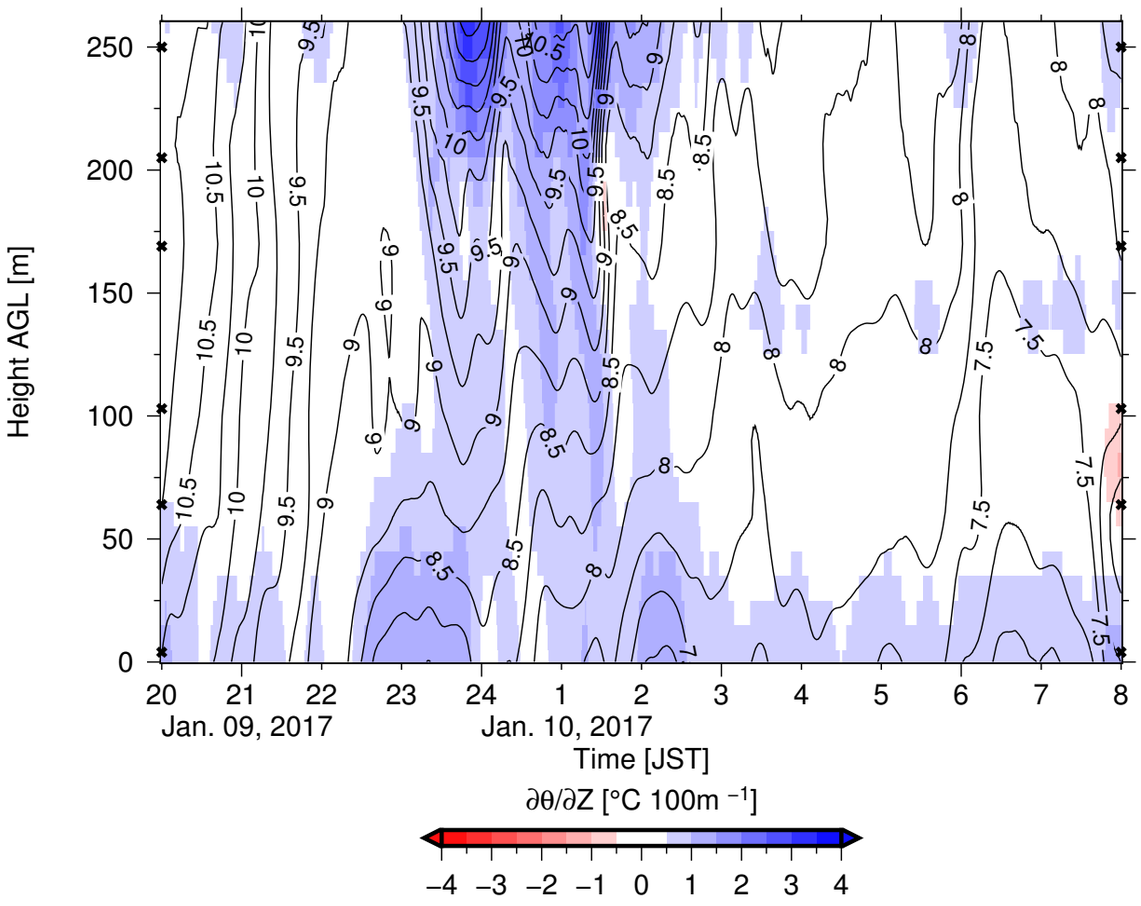

Figure 50: Temporal variations of the potential temperature (contours) and potential temperature gradient (colors) at the TT from 18:00 January 09, 2017 to 09:00 JST January 10, 2017

Analysis data were the moving-averaged 10-min data. The contour interval is 0.25℃.

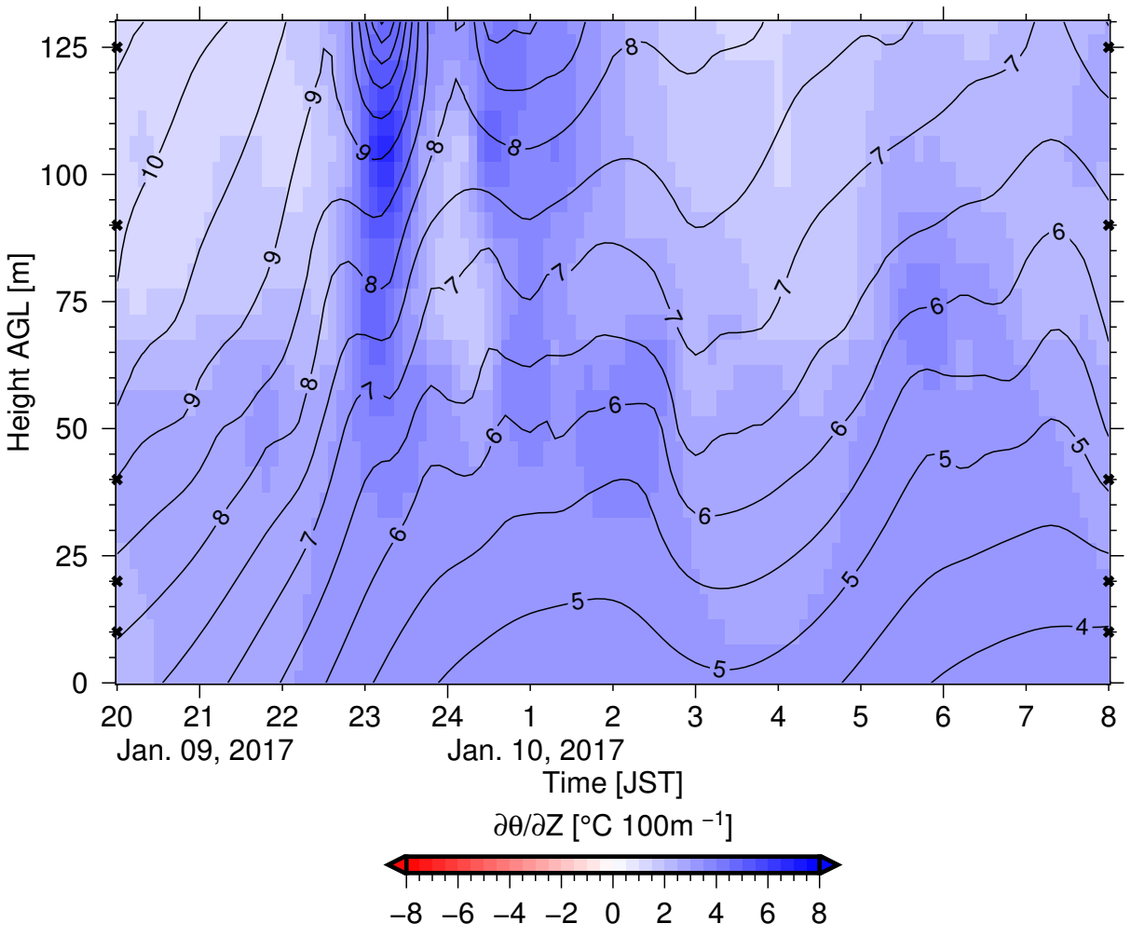

Figure 51: Temporal variations of the potential temperature (contours) and potential temperature gradient (colors) at the ST from 18:00 JST January 09, 2017 to 09:00 JST January 10, 2017

The contour interval is 0.5 ℃.

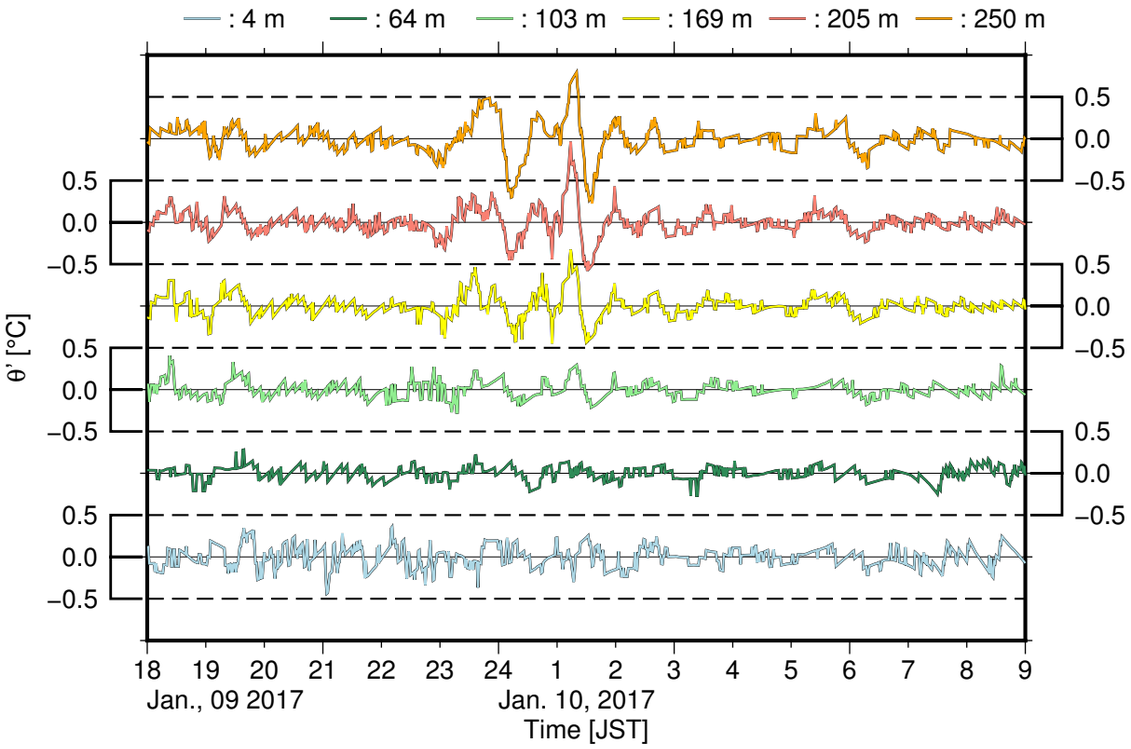

Figure 52: Vertical variations of θ' from 18:00 JST January 09, 2017 to 06:00 JST January 10, 2017

θ' is the potential temperature deviation from the 61-min moving average. Dashed lines represent the average $\pm$ 0.5℃. The lines are vertically shifted to avoid overlap.

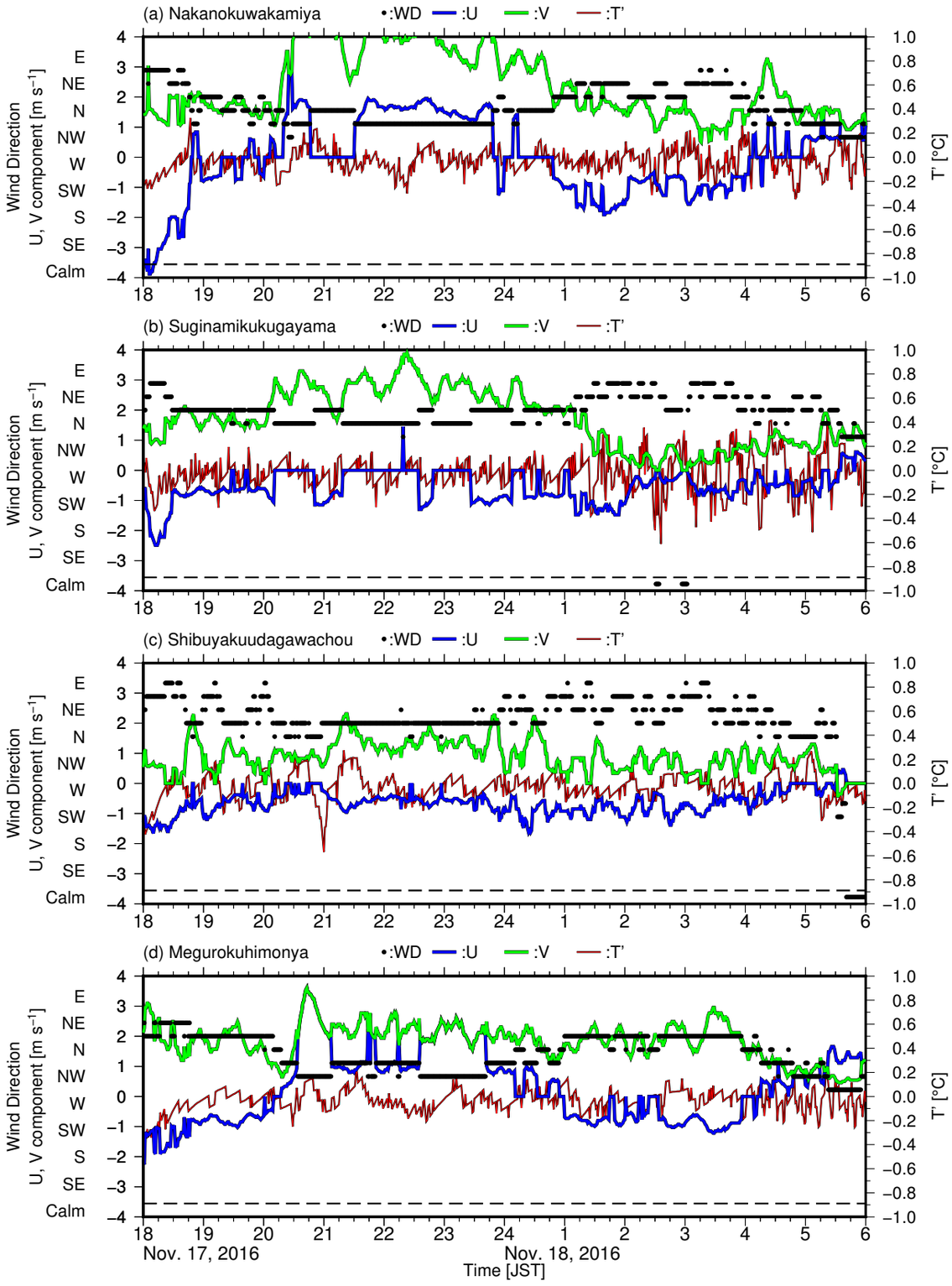

Figure 53: Temporal variations of the WD, the zonal (U) and the meridional (V) components of the wind speed, and the temperature deviation from $\overline{T}$ (T') in Case-3 (November 17–18, 2016)

(a) Nakanokuwakamiya, (b) Suginamikukugayama, (c) Shibuyakuudagawachou, and (d) Megurokuhimonya. $\overline{T}$ is 61-min moving-average temperature.

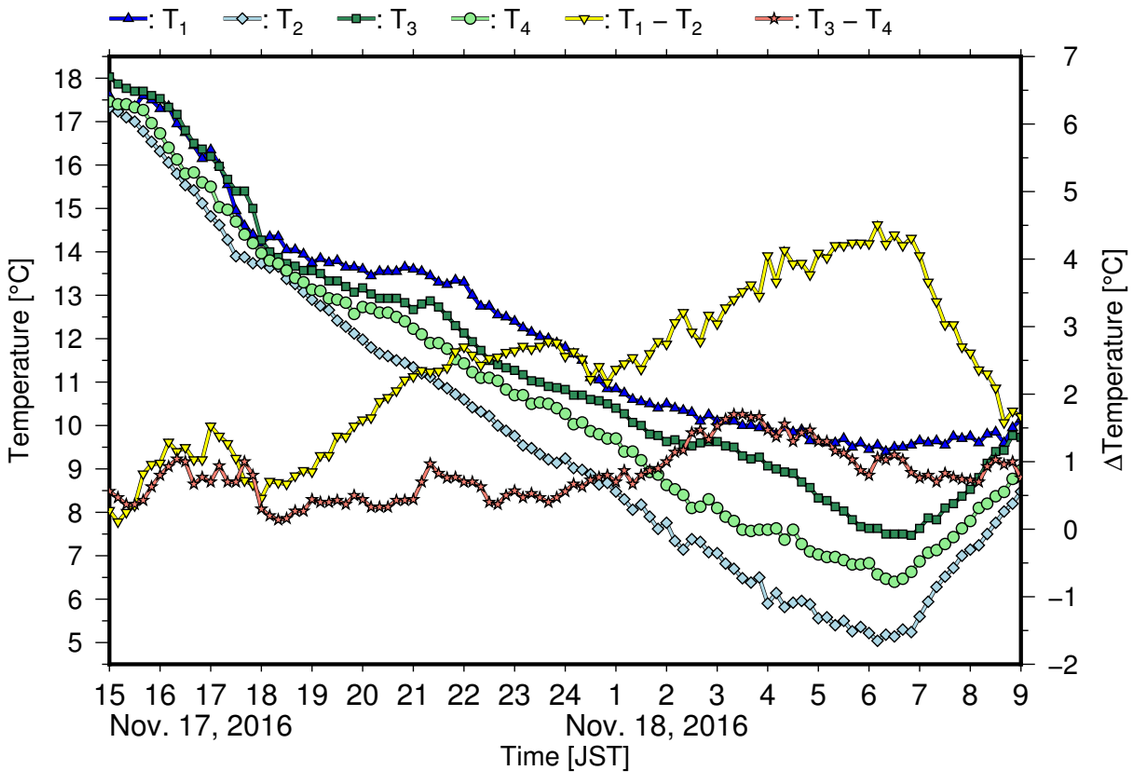

Figure 54: Temporal variations of temperatures in different areas of the Tokyo metropolis (see text for details) and their differences in Case-3

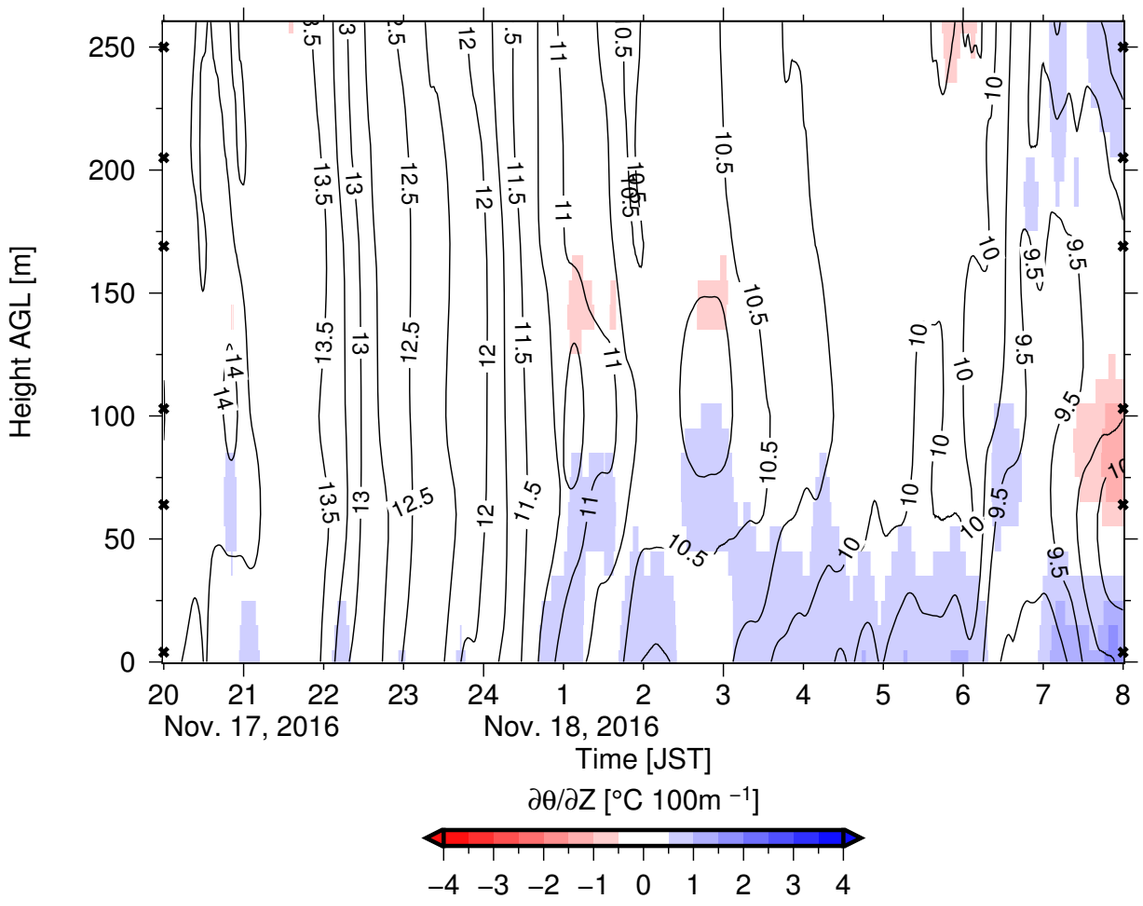

Figure 55: Temporal variations of the potential temperature (contours) and potential temperature gradient (colors) at the TT from 20:00 November 17, 2016 to 08:00 JST November 18, 2016

Analysis data were the moving averages of 10-min data. The contour interval is 0.25°C.

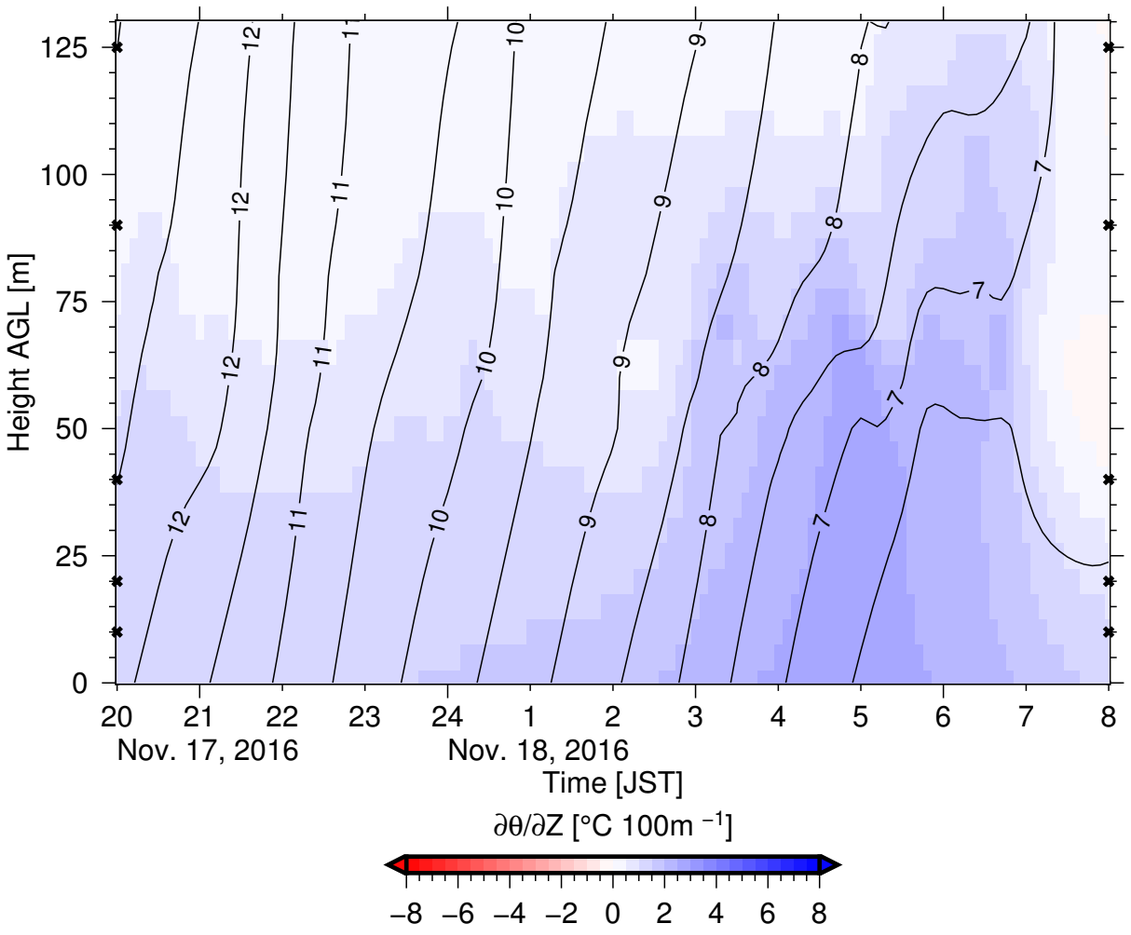

Figure 56: Temporal variations of the potential temperature (contours) and potential temperature gradient (colors) at the ST from 20:00 November 17, 2016 to 08:00 JST November 18, 2016

The contour interval is 0.5 ℃.

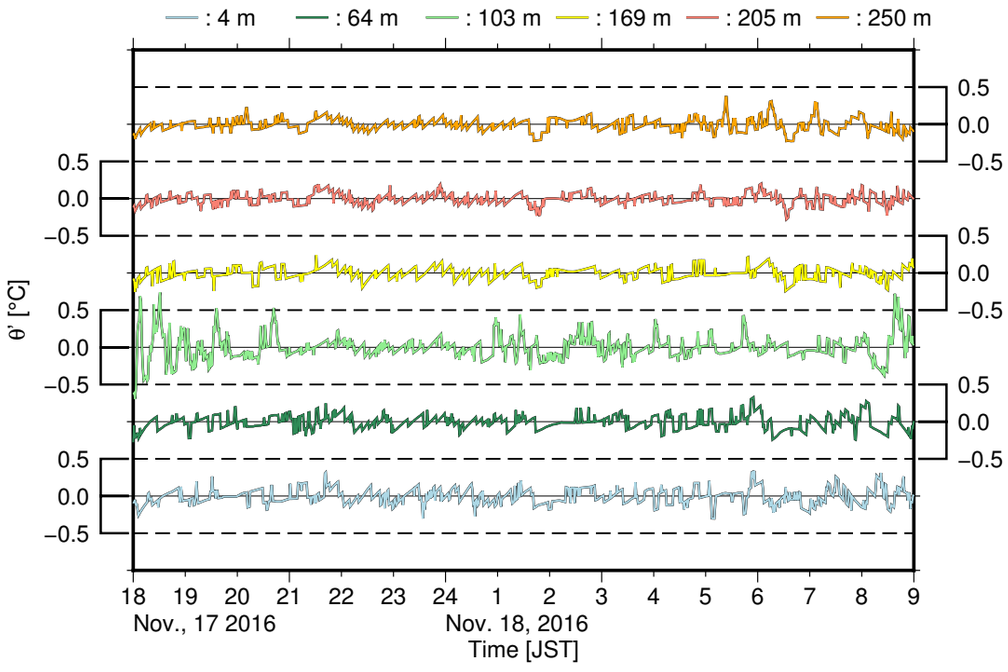

Figure 57: Vertical variations in θ' from 18:00 November 17, 2016 to 06:00 JST November 18, 2016

θ' is the potential temperature deviation from the 61-min moving average. Dashed lines represent the average $\pm$ 0.5℃. The lines are vertically shifted to avoid overlap.

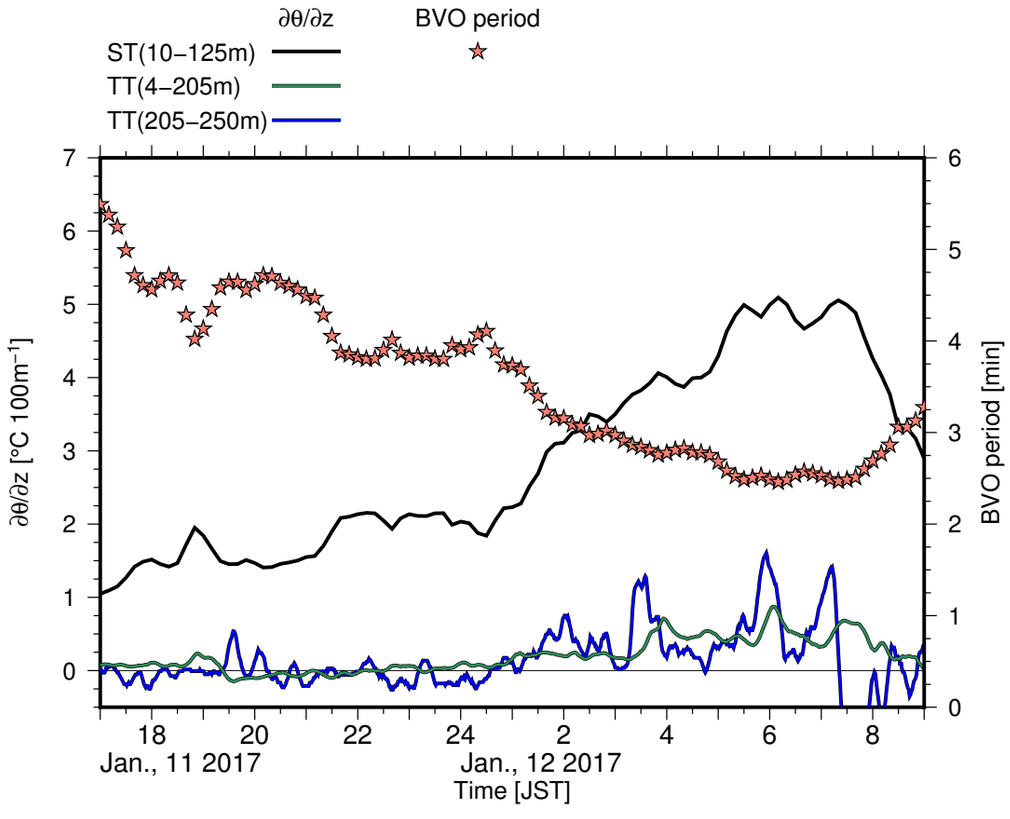

Figure 58: Temporal variations of the potential temperature gradients at the ST and TT, and the Brunt-Väisälä oscillation (BVO) period at the ST, from 17:00 JST January 11, 2017 to 09:00 JST January 12, 2017

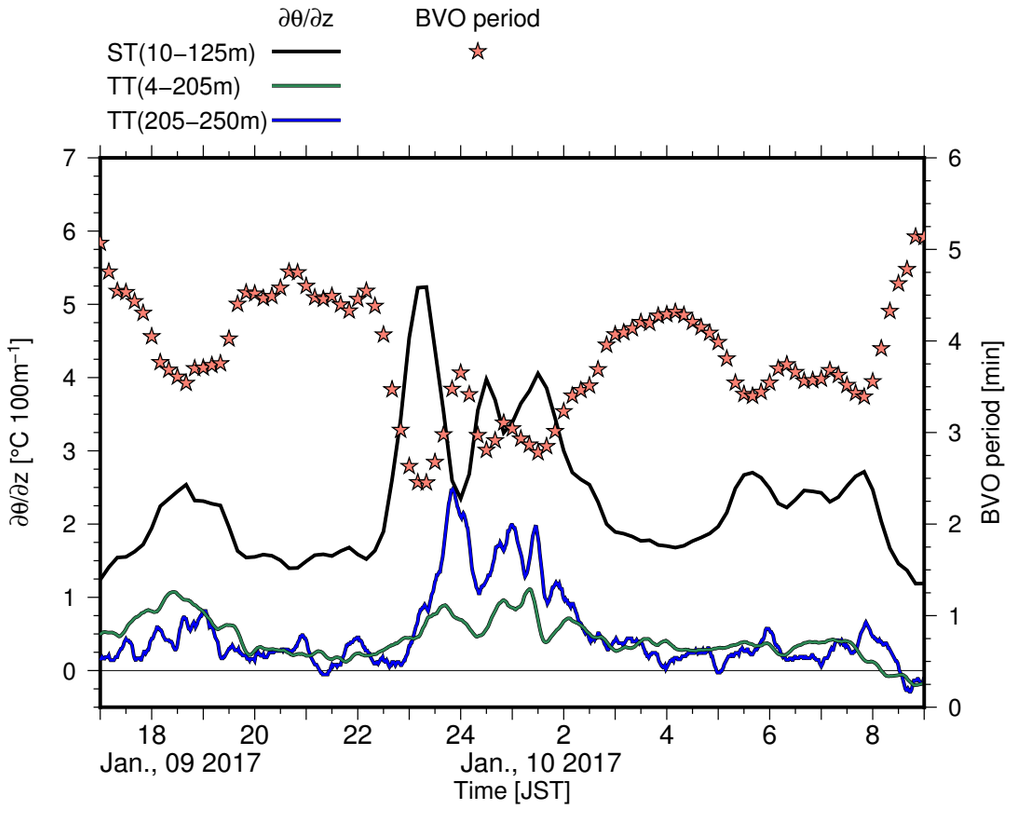

Figure 59: Temporal variations of the potential temperature gradients at the ST and TT, and the Brunt-Väisälä oscillation (BVO) period at the ST, from 17:00 January 09, 2017 to 09:00 JST January 10, 2017

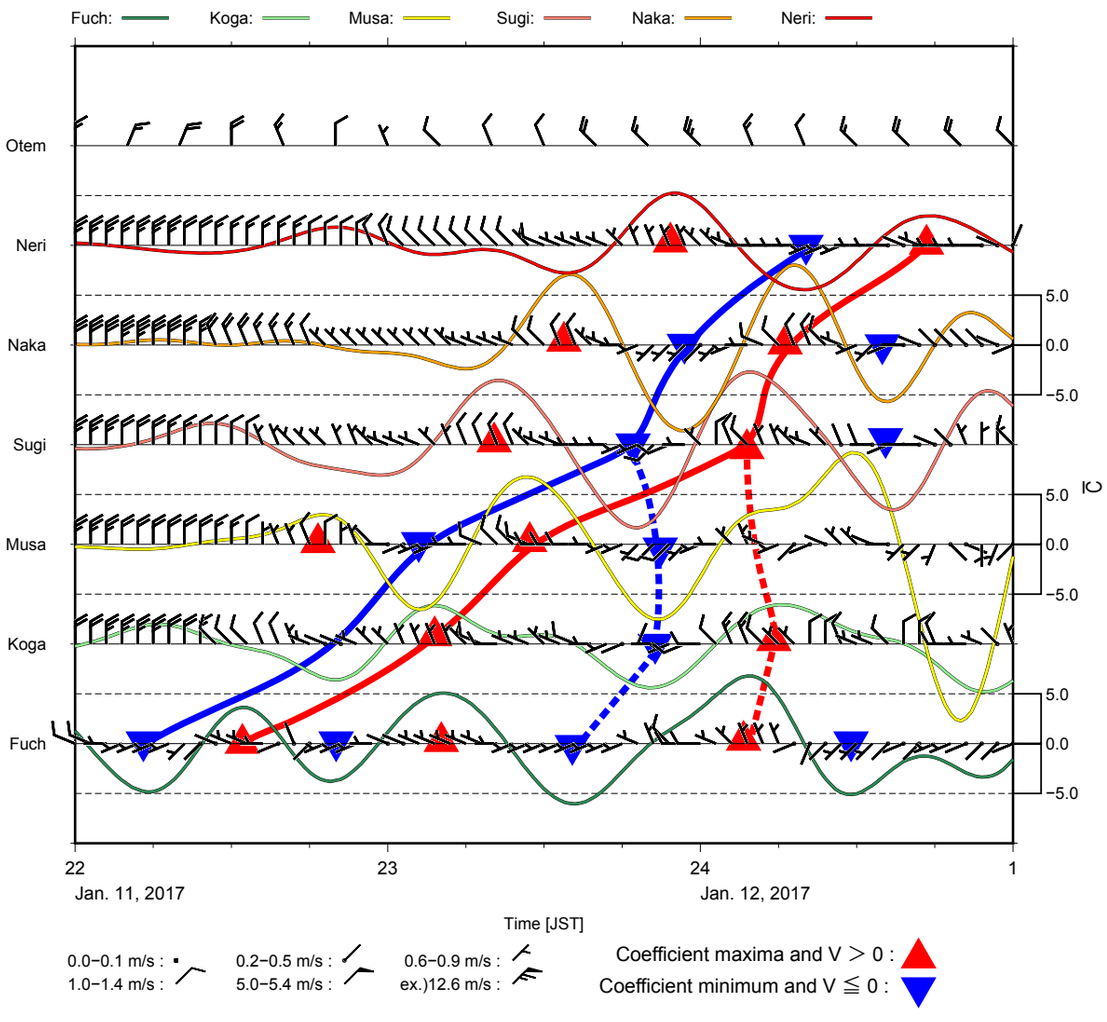

Figure 60: Temporal variation of wind barbs and $\overline{C}$ in the horizontal plane along the Otemachi–Fuchu cross-section from 18:00 JST January 11, 2017 to 06:00 JST January 12, 2017

Fuch, Koga, Musa, Sugi, Naka, Neri and Otem denote Fuchuushimiyanishichou, Koganeishihonchou, Musashinoshisekimae, Suginamikukugayama, Nakanokuwakamiya, Nerimakukitamachi and Otemachi, respectively. $\overline{C}$ indicates the scale averaged coefficient between 20 and 50 mins obtained from Wavelet analysis. The blue and red lines are connected coefficient maxima and minimum, respectively and the dashed and solid lines mean propagation pattern P_1 and P_2.

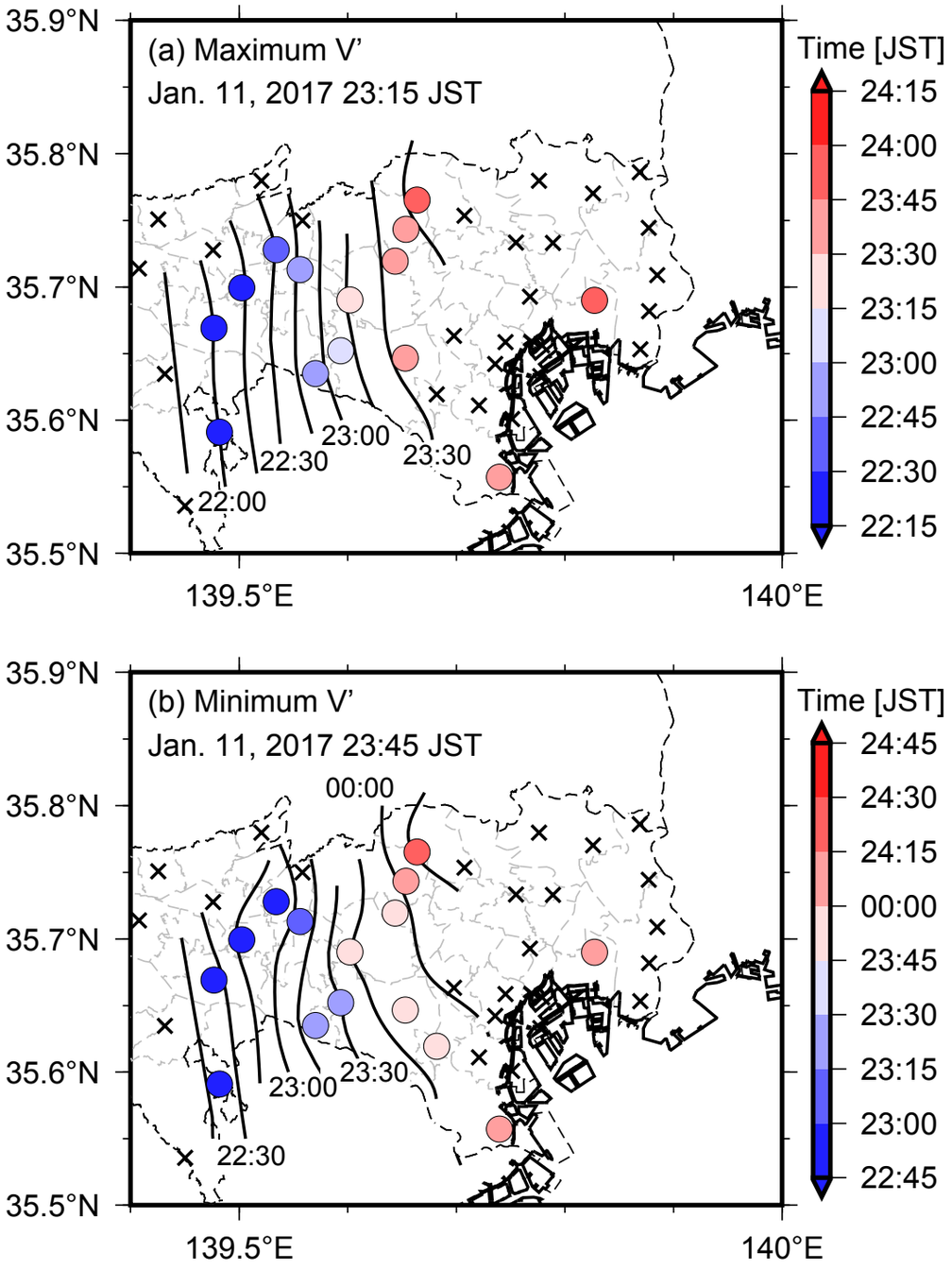

Figure 61: Positions of (a) maximum V' peak, and (b) minimum V' peak in Case-1

Stations recording non-clarified periodic motions are marked with ×.

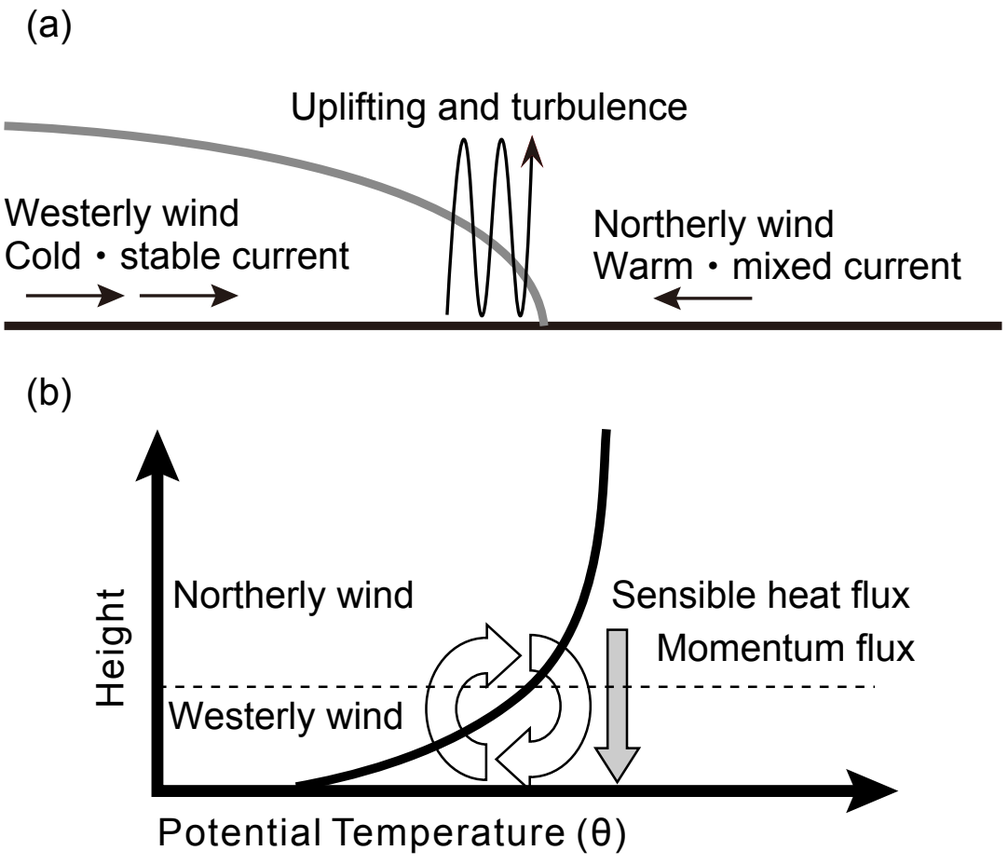

Figure 62: Conceptual diagrams of wavelike motions: (a) generation of wavelike motions, (b) vertical mixing induced by wavelike motions

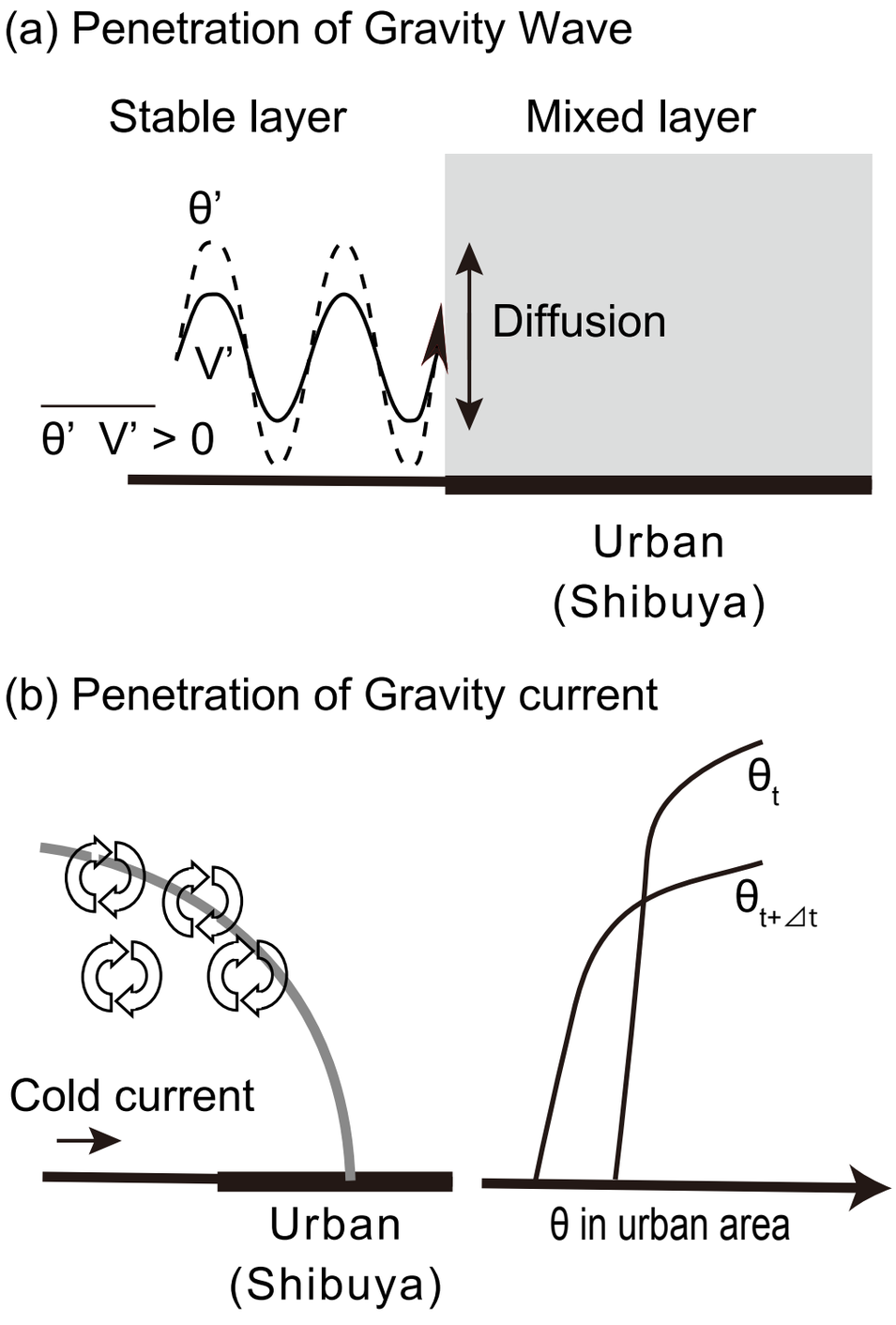

Figure 63: Conceptual diagrams of (a) gravity waves and (b) gravity currents from non-urban areas penetrating urban areas

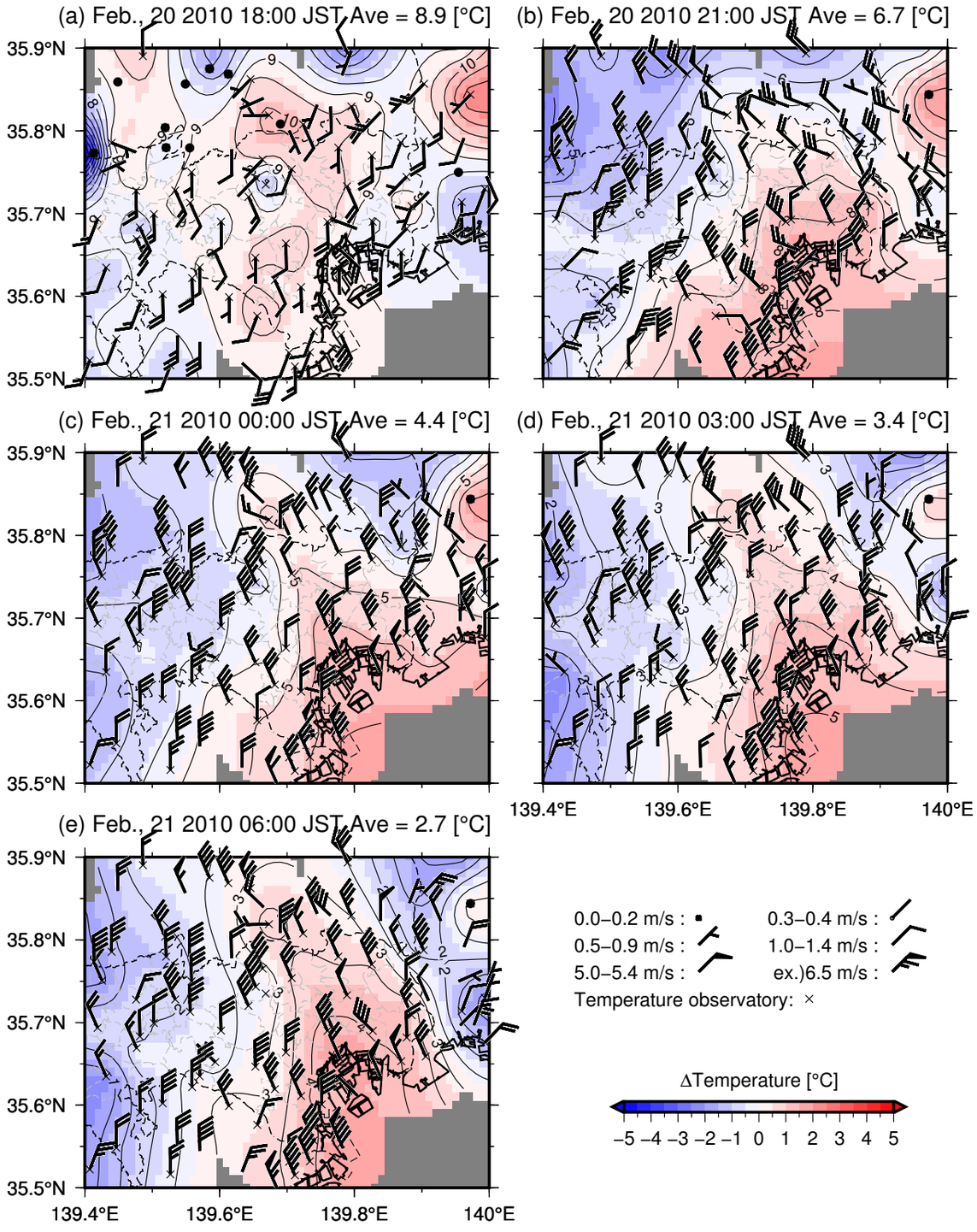

Figure 64: Distributions of temperature deviation (colors), temperature (contours) and the wind system around the Tokyo Wards area at 3-h intervals starting from 18:00 JST February 20, 2010

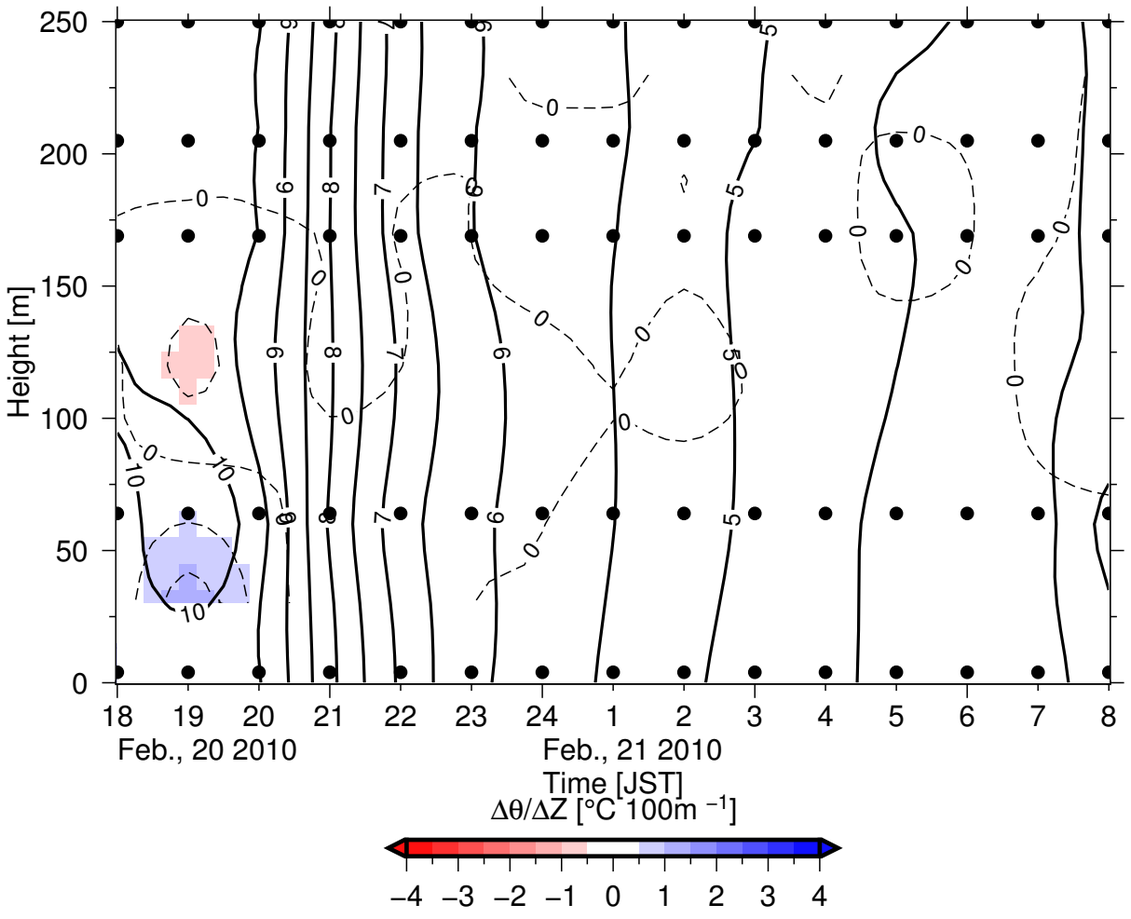

Figure 65: Temporal variations of the potential temperature (contours) and potential temperature gradient (dashed lines, colors) at the TT

Table 1: Monthly numbers of clear nights with weak winds (2001–2010)

Apr.	May	June	July	Aug.	Sept.	Oct.	Nov.	Dec.	Jan.	Feb.	Mar.	Annual
25	13	6	10	6	11	14	42	57	50	27	30	291

Table 2: Cases of clear nights with weak winds

No.	Date	H [m]	Q [kJ m^{-2}]
01	Nov. 17, 2016–Nov. 18, 2016	-	-
02	Nov. 25, 2016–Nov. 26, 2016	88	108
03	Dec. 16, 2016–Dec. 17, 2016	131	280
04	Dec. 17, 2016–Dec. 18, 2016	84	241
05	Dec. 20, 2016–Dec. 21, 2016	76	154
06	Dec. 31, 2016–Jan. 01, 2017	109	229
07	Jan. 02, 2017–Jan. 03, 2017	142	160
08	Jan. 06, 2017–Jan. 07, 2017	-	-
09	Jan. 09, 2017–Jan. 10, 2017	-	-
10	Jan. 10, 2017–Jan. 11, 2017	-	-
11	Jan. 11, 2017–Jan. 12, 2017	176	420
12	Jan. 12, 2017–Jan. 13, 2017	104	96
13	Jan. 15, 2017–Jan. 16, 2017	115	202
14	Jan. 17, 2017–Jan. 18, 2017	162	292
15	Jan. 25, 2017–Jan. 26, 2017	163	245
16	Jan. 27, 2017–Jan. 28, 2017	-	-
17	Feb. 02, 2017–Feb. 03, 2017	-	-
18	Feb. 19, 2017–Feb. 20, 2017	-	-
	Average	123	221

H and Q denote the coincident point and amount of heating, respectively.

"-" indicates cases with no coincident point below 250 m.

Table 3: Characteristics of vertical potential temperature profiles based on observations and numerical model simulations when an upper inversion layer appears in the urban atmosphere

Method	Season	Paper, figure or table	Case	City	Surface layer	Upper layer	
					γ (℃100 m^{-1})	Height of bottom (m)	γ (℃100 m^{-1})
Observation	Summer	Saito (1977), Fig.9 (a)	Aug. 1975 06 LST	Otemachi, Tokyo	0.3*3	200–300	1.4*3
		Godowitch *et al.* (1985), Fig.3	July 27, 1975 05 LST	St. Louis, America	0.5*3	160–350	2.0*3
	Winter	Ohta (1966), Fig.35	Nov. 1963 04 LST	Minato-ward, Tokyo	1.8*3	78–120	3.3*3
		Yokoyama *et al.* (1974), Table 2-2	Nov. 30, 1973 05 LST	Kita-ward, Tokyo	1.5*3	150–175	7.6*3
		Saito (1977), Fig.8	Dec. 1975 06 LST	Otemachi, Tokyo	0.1*3	200–250*3	2.2*3
		Uno *et al.* (1988), Fig.4 (a)	Nov. 20, 1984 23 LST	Sapporo, Hokkaido	1.3*3	38–90	6.9*3
		Ohara *et al.* (1989), Fig.6	Jan. 28, 1983 01 LST	Shinjuku-ward. Tokyo	0.6*3	140–220*3	4.6*3
		This study, Fig.15	2001–2010	Minato-ward. Tokyo	Ave.: 0.5 Max.: 0.9 Min.: 0.0	205–	Ave.: 3.4 Max.: 9.8 Min.: 1.9
Numerical Simulation	Summer	Martilli (2002), Fig.2 and Table 2	June 03 LST	Europe∗1	0.1*3	87–176	2.2
		Martilli *et al.* (2002), Fig.9	Sept. 00 LST	Europe∗1	0.1*3	120–170	1.2*3
		Kusaka and Kimura (2004), Fig.6	Summer 03 LST	Tokyo urban area∗2	0.0*3	120–170	0.1*3
		JMA (2013), Fig.4-4	Aug. 2012 05 LST	Otemachi, Tokyo	0.1*3	300–500	0.6*3
	Winter	Uno *et al.* (1989), Fig.3 (b)	Nov. 1984 nighttime	Sapporo, Hokkaido	0.4*3	50–90*3	2.7*3
		Saitoh *et al.* (1996), Fig.15	Mar. 14, 1992 03 LST	Tokyo urban area	-0.5*3	290–760*3	0.5*3

*1: The city was located at the center of domain and was 10 km wide. Building height were almost the same as average of the standard values for European cities.
*2: The city was located at the center of domain with 30 km wide. Building height were almost the same as average of Tokyo metropolitan area.
*1, *2: The modeling domains are flat and 2D
*3: The values were obtained from each figure
LST: Local Standard Time
γ: Potential temperature gradient

Table 4: Wind speed statistics at the ST on clear nights with weak winds, averaged over 01:00 to 06:00 JST

	Height (m)			
	45	80	115	151
Average (m s^{-1})	3.5	4.3	4.2	4.8
Standard deviation (m s^{-1})	3.5	4.3	4.2	4.8